
Investigation of the Dynamics and Synchronization Effects in Coupled Systems by Means of Symbolic Representations

Steffen Mihatsch



München 2012

Investigation of the Dynamics and Synchronization Effects in Coupled Systems by Means of Symbolic Representations

Steffen Mihatsch

Dissertation
an der Fakultät für Physik
der Ludwig-Maximilians-Universität
München

vorgelegt von
Steffen Mihatsch
aus München

München, den 15.5.2012

Erstgutachter: Prof. Dr. Gregor Morfill
Zweitgutachter: Prof. Dr. Joachim Rädler
Tag der mündlichen Prüfung: 9.5.2012

Zusammenfassung

Symboldarstellungen sind eine Methode aus dem Bereich der Zeitreihenanalyse, um Charakteristika der lokalen Dynamik von Zeitreihen zu beschreiben, indem lokale Ordnungsmuster innerhalb einer Zeitreihe auf Permutationen abgebildet werden. Ihre Struktur als endliche Gruppe blieb in der Literatur bisher weitgehend unbenutzt. Aufbauend auf dem Konzept der Transfersymbole, das Relationen zwischen Zeitreihen mit Hilfe der Gruppenstruktur beschreibt, soll die vorliegende Arbeit Erkenntnisse und Methoden aus der Algebra endlicher Gruppen für praktische Anwendungen von Symboldarstellungen in der Zeitreihenanalyse nutzen. Die betrachteten Methoden sind generisch, effizient, robust und anwendbar auf eine Vielzahl von Systemen.

Die Arbeit beginnt mit einer Zusammenfassung einiger theoretischer Grundlagen zu nicht-linearer Dynamik bzw. Chaos, sowie zur Einbettung mittels Zeitversatzkoordinaten, und gibt eine kleine Übersicht etablierter Maße zur quantitativen Beschreibung von Synchronisation, Komplexität und Ähnlichkeit von Zeitreihen.

Im Theorieteil untersuche ich symbolische Darstellungen sowohl aus der 'klassischen' als auch der algebraischen Perspektive, d. h. als Ordnungsmuster und als Transformationen. Es ergeben sich erhebliche Unterschiede zwischen den beiden komplementären Blickwinkeln. Weitere Themen sind die Eindeutigkeit der Darstellung und eine geeignete Wahl der Einbettungsparameter im Kontext symbolischer Darstellungen.

Der anwendungsorientierte Teil nutzt Symboldarstellungen um raum-zeitliche Strukturen in komplexen Systemen zu untersuchen. Das erste Beispiel ist ein Gitter aus gekoppelten Abbildungen, d. h. ein raum- und zeitdiskretes dynamisches Modellsystem. Der Untersuchung der vielfältigen dynamischen Regimes mit etablierten Methoden wird eine symbolbasierte Charakterisierung gegenübergestellt. Das Langzeitverhalten des Systems wird auf Konvergenz und Stabilität untersucht. Dabei wird gezeigt, dass mit der symbolbasierten Beschreibung schon in einem frühen Stadium die spätere Dynamik vorhergesagt werden kann.

Als weiteres Anwendungsbeispiel werden elektroenzephalographische (EEG) Mehrkanal-daten des menschlichen Gehirns untersucht, also die Anwendung der Methode auf einen sehr umfangreichen, hochdimensionalen realen Datensatz wie er im Umfeld der Narkoseüberwachung erzeugt wird. Das Interesse gilt dabei im Speziellen der Hintergrundaktivität und akustisch evozierten Potentialen. Ziel ist neben einer symbolbasierten Beschreibung der dynamischen Regimes die Unterscheidung von Bewusstseinszuständen im Hinblick auf die klinische Narkoseüberwachung.

Abstract

Symbolic representations are a method from the field of time series analysis, describing characteristics of the local dynamics by mapping local order patterns within a time series to permutations. In the literature, the structure of the set of permutations as a finite group has mostly been unused. Building on the concept of transfer symbols, which describes relations between time series with the help of the group structure, the present work uses insights and methods from the algebra of finite groups for practical applications of symbolic representations in time series analysis. The considered methods are generic, efficient, robust, and applicable to a wide range of systems.

The present work starts with a summary of some theoretic fundamentals of nonlinear dynamics and chaos, as well as time-delay embedding, and gives a brief overview of established quantitative measures for synchronization, complexity and similarity of time series.

In the theory part, I examine symbolic representations from the 'classical' as well as from the algebraic perspective, i. e. as order patterns and as transformations. Fundamental differences arise between the two complementary viewpoints. Further topics are the uniqueness of the representation, and the choice of embedding parameters in the context of symbolic representations.

The application-oriented part uses symbolic representations to study spatio-temporal structures in complex systems. The first sample application is a coupled map lattice, i. e. a spatially and temporally discrete dynamical model system. An examination of the various dynamical regimes with established methods is compared to a symbol-based characterization. The long term behavior of the system is examined for convergence and stability, finding that a symbol-based description can be used to predict the long term dynamics from an early stage.

As a further application, multi-channel electroencephalographic (EEG) data from the human brain is studied, i. e. a similar methodology is applied to a voluminous high-dimensional real-world data set, like the ones generated in the monitoring of consciousness in general anesthesia. The focus is on the background activity, and on acoustically evoked potentials. Apart from a symbol-based description of the dynamical regimes and the transitions between them, the main objective is the distinction of different states of consciousness with regard to the clinical monitoring of general anesthesia.

Contents

1	Introduction	1
2	Theoretical Background	7
2.1	Coupled Dynamics and Complex Systems	8
2.1.1	Nonlinearity and Chaos	8
2.1.2	Attractors	12
2.2	Delay-Coordinate Embedding	12
2.3	Measures of Order	14
2.3.1	Synchronization	15
2.3.2	Complexity	17
2.3.3	Interdependence	18
3	Symbolic Representations	21
3.1	Basics	22
3.1.1	Main Concept of State and Transfer Symbols	22
3.1.2	The Conceptual Difference between Rank Orders and Permutations	24
3.1.3	The Symbolic Formalism	25
3.1.4	Symbols as Partition of a State Space	29
3.1.5	Uniqueness of the Representation	31
3.1.6	Embedding Parameters	33
3.1.7	Symmetry with Respect to Transformations of the Underlying Time Series	37
3.2	Derived Measures	38
3.2.1	Class Formation	38
3.2.2	Distance Measures on S_n	39
3.2.3	The Kullback-Leibler Distance	42
3.2.4	Distance to Independence	45
3.3	Change of Sequence Length, and Entropy Rate	47
3.3.1	Expansion	48
3.3.2	Truncation	50
3.3.3	Conjugacy Classes under Change of Sequence Length	50
3.3.4	Transition between Overlapping Symbols	51
3.3.5	Entropy Rate of a Symbolic Representation	53

4	Application to a Model System: A Coupled Map Lattice	57
4.1	Introducing the Model System	58
4.1.1	Coupled Map Lattices	58
4.1.2	The Logistic Map	59
4.1.3	The CML Model System	60
4.1.4	Model Assumptions	61
4.2	Prominent Dynamical Regimes	62
4.2.1	Conventional Measures	62
4.2.2	Phase Diagram of the Parameter Space	64
4.2.3	Characterization of the Regimes	66
4.2.4	Analytical Description of the Fixed Point Regime	69
4.2.5	Dependence on Initial Conditions	71
4.3	Symbolic Description of the System Dynamics	72
4.3.1	Order Distribution of Transfer Symbols	72
4.3.2	Prototypical Symbol Distributions	75
4.3.3	Forbidden Symbols and Suppressed Classes	77
4.3.4	Transitions Between Dynamical Regimes	78
4.3.5	Symbolic Complexity Measures	80
4.4	Convergence and Stationarity	82
4.4.1	Transient Times	83
4.4.2	Transient Behavior	85
4.5	Stability	87
4.5.1	Global Perturbations	88
4.5.2	Propagation of Local Perturbations	88
4.5.3	Perturbations of the Coupling Parameters	93
4.5.4	Model System with Continuously Varying Parameters	94
4.6	Predicting the Long-Term Behavior	95
5	Application to a Life Science System: Multi-Channel EEG	99
5.1	The Electroencephalogram	100
5.1.1	The Brain as a Coupled System	100
5.1.2	Reasons to Study the Electrical Activity of the Brain	100
5.1.3	The EEG as an Observable of a Complex System	100
5.2	Experimental Setup	102
5.3	Spatial Phenomena	104
5.3.1	Formal Similarities between Multi-Channel EEG and CML	104
5.3.2	Structure on Different Scales	104
5.3.3	Paths between Hypnotic States	106
5.3.4	A Symbol-Based Measure of Anesthetic Depth	110
5.3.5	Distinguishing Different States of Consciousness	113
5.4	Auditory Evoked Potentials	117
5.4.1	Modelling of the Average Profile	118
5.4.2	Distinguishing Different States of Consciousness	119
6	Discussion and Conclusions	123
	Bibliography	129
	Acknowledgments	137

Chapter 1

Introduction

The fundamental laws of nature can generally be expressed in complete form using compact and universal formulae. In real-world situations, however, a purely analytical, reductionist approach quickly becomes too complex to be handled. An elementary example is the three-body problem of Newtonian mechanics, which does not allow a general closed-form solution. In more complex systems, like the earth's atmosphere or a tissue of living cells, it is often not possible to define an appropriate state space, determine the current state of a system with the necessary accuracy, or even to formulate the equations for each involved degree of freedom. Therefore, purely analytical approaches break down quickly and scientists have to rely on approximative and numerical methods.

Most real world situations consist of a multitude of interacting parts, each with its own preferred rhythm, coupled to the others and exposed to ceaseless perturbations from the environment. Nevertheless, we frequently observe phenomena of emerging order, where systems form self-organized structures in the absence of any central control instance. Occurring phenomena of this kind include bird swarms acting like a single super organism, pedestrians involuntarily falling in lockstep on a vibrating bridge, or brain cells synchronizing in cognitive and sensory processes.

The present work focuses on the evaluation of this sort of behavior. When studying such a coupled system and its dynamics, the main difficulty often is not to gather a sufficient amount of data, but to extract the information that is relevant for a certain research question. Many observables can be measured from an experimental system, and numerical simulations can be done with many degrees of freedom, but it is still an active field of research how to describe the occurring phenomena of emerging order and to understand the underlying dynamics.

The measured or simulated data from a coupled system usually has the form of one or multiple time series. The observables describing an experiment typically are a nonlinear superposition of multiple state variables, containing noise and redundancy. The problem is to condense one or multiple time series to those features that are essential for a specific question, in order to extract meaningful properties describing the dynamics of subsystems and their interactions. Even though the systems are usually too complex to allow for precise predictions of future states, it is often possible to predict the type of future dynamics by knowing the attractor of the system.

In the context of time series analysis, many concepts have been introduced. *Complexity*, using measures like entropies, Lyapunov exponents, and dimensionality measures, denotes system behavior that needs more information to describe than the behavior of the components.

Synchronization describes similarities between system components, which may result in a coupled dynamics that displays more order than the behavior of the isolated components.

Bandt and Pompe [11] introduced the concept of *symbolic representations* as a method for the analysis of time series. It is based on the evaluation of the rank order of short data sequences. Thus, a time series is described as a sequence of order patterns, referred to as a *symbolic representation* hereafter. Apart from the context of complexity [5], the concept proved useful to describe synchronization [56].

Symbolic representations are invariant with respect to monotonic transformations and robust with respect to noise. Furthermore, they are computationally inexpensive, compared to common measures like the Fourier or Hilbert transformation.

Even though the algebraic term *permutations* was used from the beginning, the symbols were treated purely as patterns in the above mentioned previous work, focusing on properties of their statistical distribution.

The field of symbolic representations was linked to the domain of algebra by the more recent approach of Monetti et al [65], who used the algebraic structure of the permutation group to introduce transfer symbols as a description for the interrelations between pairs of symbol sequences. Because this concept of transcription is more compatible with algebraic structures than the original use of order patterns, this new approach opens up the opportunity to study symbolic representations in algebraic terms. A main objective of the present work is to apply insights from the algebra of finite groups to the field of time series analysis in the context of symbolic representations. The description of emerging spatio-temporal synchronization effects will be one of the central issues of this work, because transfer symbols by construction are able to account for relations both in space and time.

In order to prepare the discussion of symbolic representations, chapter 2 summarizes several basic aspects. This is helpful for both the discussion of special properties of symbols and for the development of representation concepts in the context of the succeeding applications.

Section 2.1 is a brief introduction to complex systems and chaos. In the modeling of real world systems, weak coupling between system components is often neglected, or approximated in a linearized way. Typically, such systems tend to develop trajectories that either converge to a fixed point, a periodic orbit, or diverge towards infinity. The introduction of nonlinear coupling terms can lead to a new kind of dynamical behavior, called *chaos* because it exhibits properties usually associated with randomness in spite of being generated by a fully deterministic system.

In section 2.2, a summary of *delay-coordinate embedding* is presented for its importance to the methodologies derived in the following sections. A well-known theorem by Takens [102] shows how – under certain conditions – the topology of the attractor of a dynamical system can be reconstructed from the time series of a single observable. This reconstruction is carried out using two important parameters, namely the embedding dimension and the time delay, which also play an essential role in the construction of a symbolic representation.

In the context of the systems and effects studied here, section 2.3 presents a discussion of various concepts related to emerging order and self-organized structures. The concept of *synchronization* is probably the most fundamental notion. It is used in different contexts, typically without a rigorous definition. The term refers to regular events happening at the same time for different (sub)systems, or cyclic processes sharing a common rhythm. Examples in the literature include systems like pendulum clocks, the human circadian rhythm, and chaotic model systems. Section 2.3.1 discusses an established definition by Pikovsky et al. [76],

which formalizes the notion of synchronization as an adjustment of rhythms, which happens between active oscillators and is caused by weak coupling. Sections 2.3.2 and 2.3.3 provide measures related to *complexity* and *interdependence*, respectively, with a focus on methods that are applicable to discrete data.

Chapter 3 is devoted to the main research objective of this work: symbolic representations. A trajectory of a dynamical system is mapped to one or multiple sequences with values in a finite group. Dependent on the construction of the mapping, different time scales and dynamical characteristics can be filtered. Group and information theoretic methods can be applied to the discrete symbol data, in order to develop measures for synchronization, complexity, mutual interdependence, or directionality in the coupling.

Transfer symbols [65] were defined as the transcriptions between two symbol sequences that are generated by the group structure. They are used to describe mutual interdependences in pairs of time series. Based on this concept, a main objective of this work is to further exploit the algebraic structure of the symmetric group, in order to develop refined concepts for depicting and extracting characteristics of a trajectory.

In section 3.1, I first describe the central idea behind symbolic representations, before embedding it into a formalized algebraic structure. Since a major part of this work is the connection between the existing work on order patterns and the algebraic properties of the group of permutations, the fundamental differences between the two viewpoints on symbols, referred to as 'order patterns' and 'permutations', are compared. There are various notations and conventions from related fields, concerning the elements of the symmetric group, and their group structure. I summarize the different notations, and discuss how they fit into a common 'symbolic formalism'.

The set of symbols is described in terms of a partition of a time-delay state space, which illustrates the relation to time delay embedding. Starting from an n -dimensional space, scaling and translation symmetries are used to describe the essence of this partition as an $n-2$ -dimensional polytope. This polytope describes the geometry of the partition in terms of the relations of the different ambiguities, which arise at the boundaries between different components of the partition, where the entries of the delay vector are not pairwise different. Two methods to resolve these ambiguities are discussed, suitable for either an information theoretic or an algebraic point of view.

I discuss the parameters of a symbolic representation, namely the *sequence length* n and the *sampling pattern* τ . From time-delay embeddings of low-dimensional chaos, various algorithms have been proposed to estimate parameters for a reconstruction of the attractor. For high-dimensional systems and data contaminated by noise, however one can not hope to fully reconstruct the attractor. Instead, the aim is to construct measures that focus on certain features and time scales, which are relevant for a particular research question.

State symbols show a hierarchical structure in terms of the sequence length, in the sense that short symbols are determined by long ones. I show that such a hierarchy does not exist for transfer symbols. Moreover, different sampling patterns are related to sensitivity with respect to different time scales.

There are certain transformations that are natural for a time series. For example, the properties of many time series are invariant with respect to time reversal, or change of sign. The symmetries and invariance properties of symbolic representations under those transformations are studied. Especially the transfer symbols behave well in this context, in the sense that the main algebraic properties like the cycle structure (and hence the conjugacy class) are invariant.

State symbols have a more complex behavior, which might be a reason why algebraic properties are not commonly used in previous work in the field of symbolic representations.

So far, symbols have been considered as an abstract description. In order to answer specific questions, one needs to construct appropriate measures in terms of this description. In section 3.2, some of the concepts from section 2.3 are applied to symbolic representations, and the resulting measures are discussed. I summarize commonly used distance measures on the symmetric group, which can be used for a pointwise comparison of symbol sequences. Furthermore, the section discusses class formation, and an approach to turn the Kullback-Leibler distance into a metric. The aim is to provide a set of methods, which can be tailored to the system and the research question under consideration.

In section 3.3, the expansion and truncation of a rank order are first studied separately, and combined to describe the transition from one element of a symbol sequence to the next one. These are all natural transformations in the context of order patterns, but it is not straightforward how they change the algebraic properties of the corresponding permutations. Furthermore, the entropy rate of symbol sequences is discussed.

Coupled map lattices (CML) are commonly used prototype model systems to simulate the behavior that is typical for spatially extended complex systems. A CML is defined as a set of cells, where the dynamics of each cell is described by a recursion map. By the introduction of coupling terms, each cell has an influence on its neighbors, resulting in a dynamical system that is discrete in space and time. It is worth to mention that, whenever a system of partial differential equations is numerically simulated, it is discretized in space and integrated using finite time steps, naturally resulting in the structure of a CML.

In chapter 4, symbolic representations are applied to a CML model system. After summarizing the concept of coupled map lattices, the logistic map is discussed, which is widely used as a model system for chaos and as a base for the construction of coupled map lattices. The coupling mechanism used here was proposed by Atmanspacher et al. [8], with a square lattice geometry, nearest-neighbor coupling, and periodic boundary conditions. The model includes instant and delayed coupling forces, resulting in two control parameters, namely the coupling strength and the delay.

First, the system is examined using well-known established measures in order to obtain a reference description (section 4.2). This is used to relate the observed dynamical behavior with the results from symbolic descriptions. Measures like the Lyapunov exponent, quantities derived from recurrence plots, and linear correlation coefficients are used to describe various dynamical regimes, relating them to subsets of the two-dimensional parameter space of the system. For the fixed point regime, an analytical study of stability [7] is discussed, which is applicable to the CML system used here. It confirms the form of the spatial structure that arises at the boundary to the neighboring regimes, where the fixed point becomes unstable.

Section 4.3 studies symbolic descriptions of the system dynamics. Focusing on synchronization effects on a local level, the main descriptive method is based on transfer symbols between neighboring cells. The distribution of the algebraic order, a measure that considerably reduces the dimension of the description space, still contains enough information to allow a good separation of the different dynamical regimes. I also examine forbidden symbols, and how the transitions between different dynamical regimes are reflected in the symbolic description. The section ends with an examination of different aspects of symbolic complexity.

In section 4.4, the transient behavior of the system is studied in terms of a symbolic description. Instead of considering the distance of the trajectory to the attractor in the metric

of the state space, the symbolic description of the evolving system is compared with that of the long-term behavior. In other words, instead of asking for full convergence, I investigate, at which timescale the main dynamical features of the stationary state can be identified. In the space of order distributions, the transient path is often relatively straightforward, indicating that this description could be useful for a prediction of the system's dynamics (which is studied in section 4.6).

Section 4.5 is about the stability of the stationary state. The growth of global perturbations is studied in a classical (i. e. non-symbolic) way, comparing the time evolution of the perturbed and the unperturbed state. This approach is closely related to the Lyapunov exponent, and gives similar results, with the benefit of being sensitive to negative exponents (compared to the commonly used method [112] that reconstructs the attractor from a time series). The spatial propagation of local perturbations is examined, including transitions between individual and collective behavior as a function of the coupling parameters (within regimes corresponding to a common stationary state). The effect of (global) perturbations of the coupling parameters are observed in a symbolic description of the system. In section 4.5.4, I present an approach using a large lattice that is built as a representation of the whole parameter space. Using coupling parameters that vary monotonically in space, the neighborhood of any cell behaves as a small lattice with approximately constant coupling parameters, which is influenced by the dynamics of neighboring parameters.

In section 4.6, a symbolic description is used to predict the long term dynamics given an early state of the system. I find that a good prediction of the long term dynamics is possible, from a time before all transient processes are finished. Especially the dynamical regimes can be predicted surprisingly well, using only the first iterations of the system.

In chapter 5, I make an attempt to transfer some of the methods developed in the framework of the investigation of CML to data from one of the probably largest real-world complex coupled systems: the human brain. Its network activity, which is generated by billions of neuronal cells, is beyond any direct observation, but it is possible to capture the electrical activity on large scales, i. e. of huge neuronal collectives containing millions of individual cells.

The electric potential on the scalp is a superposition of countless signals from different sources, which originate in different positions and are distorted by volume conduction and filtering effects from the inhomogeneous, anisotropic brain tissue and the skull. Hence, the study of electroencephalographic (EEG) data actually deals with an 'inverse problem' of accessing the internal functions of the system from observables that are projections to highly reduced spaces. Generally, brain activity is detected in the form of collective activity that significantly stands out of the ceaseless 'soundscape' generated by the vast number of neurons. The EEG has a high temporal resolution at the price of a low spatial resolution. Cognitive and sensory processes are related to collective behavior of large groups of neurons, which means (not necessarily locally) synchronized 'firing'.

Aside from pure physiological interest, there are various reasons to study the human brain, for example gaining insight in occurring pathologies like epilepsy, developing treatments and monitoring their success. Another important aspect is monitoring the state of consciousness of a healthy brain: during anesthesia, there is still a small but significant number of cases of intra-operative awareness [88], where patients experience episodes of consciousness during a surgery, which can lead to severe psychological traumata.

Section 5.1 gives introductory remarks to technical aspects of the EEG recording, as far as they are necessary for the understanding of the following sections, considering multiple

aspects, such as electrode placement, reference montage, voltage and frequency range, and artifacts. The EEG data used in this work comes from a study dealing with *auditory evoked potentials* (AEP) during Propofol general anesthesia, which was designed and carried out at the *Department of Anesthesiology, Klinikum rechts der Isar, Technische Universität München* (Munich, Germany). Section 5.2 briefly summarizes the important clinical and technical data like the measuring protocol, electrode scheme and other relevant parameters.

Section 5.3 studies local synchronization behavior in the EEG by adapting the methodology used with the coupled map lattice of chapter 4. First, the presence of spatial structure is demonstrated by examining the level of similarity between the time series of pairs of electrodes as a function of their distance on the scalp. Following this, methods already used in chapter 4 are adjusted to the EEG. Using the algebraic order of transfer symbols between neighboring electrodes, the local EEG activity is mapped as a trajectory in the low-dimensional space of order distributions. The different regimes are observed as clusters, and described in terms of stationarity and dependence on the individual. This description is used to construct a scalar measure for 'anesthetic depth', which I evaluate for its discrimination power. Furthermore, I discuss some of the limitations posed by practical use during surgery.

Evoked or *event-related potentials* refer to the electrical activity on the scalp that corresponds to a specific brain function, like the execution of a cognitive task or the processing of a stimulus. This sort of activity is of special interest, because by repetition of similar stimuli, certain cognitive functions can be associated with the activity that is correlated to the time of stimulus. Since cognitive functions differ depending on the state of consciousness, the evoked potentials contain information about this state.

Section 5.4 is about *auditory evoked potentials* (AEP) caused by binaural clicking stimuli. AEP are considered a promising means of monitoring anesthetic states because the processing of acoustic stimuli is switched off last of all senses in the transition to unconsciousness [103]. In order to avoid the commonly used averaging over multiple epochs, statistics of a symbolic description are studied. The symbolic description is used for the identification of the different states of consciousness.

Chapter 6 summarizes the work, with a focus on the results and the gained insights, and gives an outlook on further possible applications of symbolic representations.

Chapter 2

Theoretical Background

This chapter briefly summarizes several topics that are important for understanding the concepts and methods used in the present work. Section 2.1 introduces the field of complex systems. As soon as nonlinearities are involved, relatively simple systems can exhibit highly complex behavior. The section briefly introduces some essential features of the resulting chaotic dynamics.

Section 2.2 discusses some basic terms and definitions of embedding theory. The essentials of Takens' theorem are recalled, which under certain conditions proves the existence of a delay-coordinate embedding for an attractor using a single observable. The parameters for the embedding, namely the embedding dimension and the time delay, play an essential role in the construction of a symbolic representation as well.

Section 2.3 gives an overview of various concepts to define and quantify order properties of dynamical systems, with particular attention to those that are applicable to discrete data. The concept of *synchronization* is probably the most fundamental notion in the context of emerging order properties in dynamical systems. It is used in a variety of contexts, typically without a rigorous definition. Some examples in the literature are given, followed by a discussion of a widely noted definition by Pikovsky et al. [76]. Other order-related concepts are summarized, subsumed under the general terms *complexity* and *interdependence*. These methods can be applied to symbolic descriptions in order to cover certain perspectives on a given problem.

2.1 Coupled Dynamics and Complex Systems

The objective of the present work is to study methods for describing and quantifying various synchronization phenomena governing the dynamics of coupled systems. Before addressing the actual research topics and presenting the methodological approaches, a careful consideration of the underlying systems is necessary.

I want to start by emphasizing the fundamental difference between linear and nonlinear dynamics. Following the arguments of section 1.2 in Strogatz [97], I focus on ordinary differential equations (ODE), but the main points are just as relevant for other settings like discrete-time mappings. Written as a system of first order, an ODE describes a finite dimensional system whose time development is given by

$$\dot{x}(t) = F(x, t). \quad (2.1)$$

If F is *linear* in x , the solutions of eq. 2.1 form a vector space. In this case the principle of *superposition* holds, essentially saying that a linear system is equal to the sum of its parts. Supposing that the coefficient matrix can be diagonalized, the parts can be solved individually, typically yielding exponential or periodic solutions. Note for instance, that the commonly used Fourier and Laplace transforms are linear maps of vector spaces. This approach sometimes includes an assumption that the signal can be understood by studying its linear components separately, for example when considering the *power spectrum* of a signal (i. e. considering only the amplitude of each frequency component and neglecting the phases).

In real-world situations, common sense often suggests linear dependence. If we observe that a certain action generally causes a certain effect, we tend to suppose that adding the action to an unknown real-world situation will add its usual effect. In many cases however, nature behaves differently: 'If you listen to your two favorite songs at the same time, you won't get double the pleasure!' [97].

2.1.1 Nonlinearity and Chaos

For nonlinear problems, the principle of superposition is not valid, thus there are no general methods to combine known solutions into new ones. Many nonlinear problems are actually not solvable in an analytical way at all. This is not only a practical calculation problem: by adding nonlinear coupling terms to a set of otherwise linear ODEs, fundamentally different dynamics can arise.

The *Lorenz system* [58], theoretically and computationally studying Rayleigh-Bénard convection to explain atmospheric turbulence, was the model that first drew attention to the kind of dynamics that later was called *chaos*.

The main characteristic of this new behavior is that a fully deterministic system can exhibit irregular, seemingly random behavior, which is not transient but an inherent part of the long term dynamics. As a physical term, *chaos* was introduced by Li and Yorke [54] (cf. [37]). Usually, the focus of chaos theory is on low-dimensional systems, because the dynamics in the state space can be accessed with reasonable amounts of data. This is an important limitation both for experimental and numerical approaches, cf. the 'curse of dimensionality' in section 3.1.6). Moreover, there is more hope for analytical results.

Chaos is common in real world systems, like a dripping faucet (Shaw [91], cf. [71]), showing regimes from constant drop intervals to periodic sequences and fully chaotic dynamics. The

incidence and importance of chaotic phenomena is often underestimated, because most commonly used physical models (for instance in education) are chosen such that they can be fully solved using calculus.

The *Rössler system* [83] was constructed as a model for time-continuous chaos. The system and its dynamics are as simple as possible,

$$\begin{aligned}\frac{dx}{dt} &= -y - z \\ \frac{dy}{dt} &= x + ay \\ \frac{dz}{dt} &= b + z(x - c),\end{aligned}\tag{2.2}$$

while still preserving the essential properties of the Lorenz system. There is only one nonlinear term in the equations and only one center of oscillation in the state space. The system still has 3 dimensions, which is the minimum to allow the 'stretching and folding'-mechanism of chaotic dynamics in a continuous-time system. This comes from the fact that folding is not possible in two dimensions because trajectories are not allowed to cross. Fig. 2.1 shows typical trajectories of the Lorenz and Rössler systems. Even in the projection to one dimension, the irregular dynamics that are characteristic for chaos are obvious.

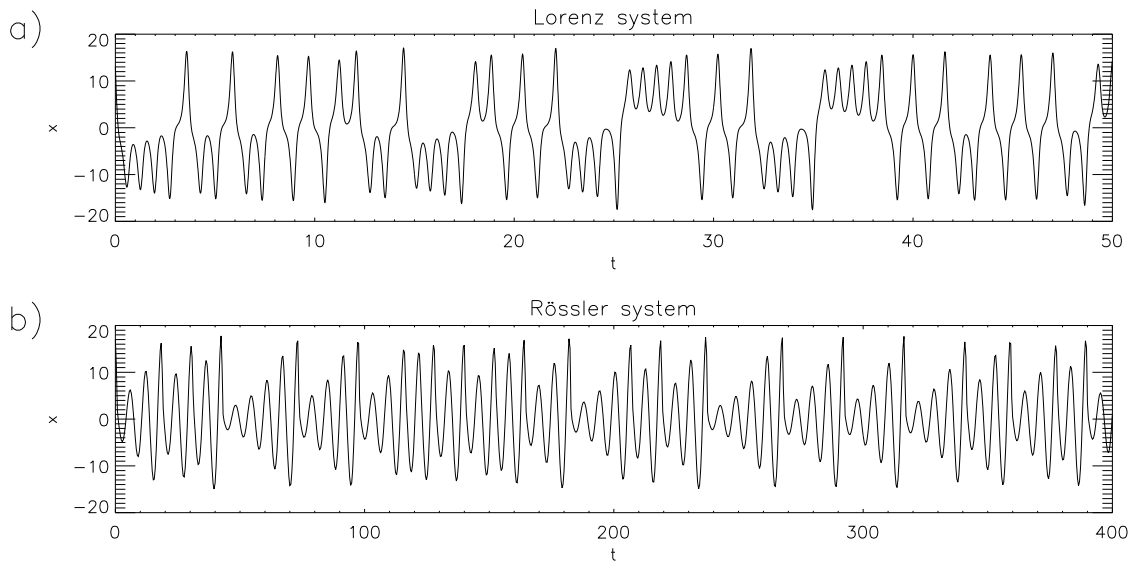


Fig. 2.1: Chaotic dynamics: a typical trajectory a) x -coordinate of Lorenz system b) x -coordinate of Rössler system.

The differential equation of a dynamical system defines a vector field on the state space. In an infinitesimal approximation (and supposing a 'well-behaved' vector field), this vector field is linear. In an infinitesimal neighborhood of a trajectory, the vector $V(x)$ at a point x always points along the trajectory. The vector $V(x')$ of a neighboring point x' points either towards, parallel to, or away from $V(x)$. This locally leads to a neighbor trajectory that either exponentially approaches, is parallel to, or diverges from the trajectory $x(t)$.

In order to describe the development of the distance, consider two neighboring trajectories. Due to the linear approximation, we only need to consider the dimension that is spanned by

the initial conditions x_0 and $x'_0 = x_0 + \delta_x(0)$. In a coordinate system centered at the reference trajectory, the vector field has the form

$$v(x) = \lambda x. \quad (2.3)$$

The reference trajectory corresponds to the solution $x(t) = 0$. Any neighboring trajectory with initial condition $x'(0) = x'_0$ leads to a solution $x'(t) = x'_0 e^{\lambda t}$. Hence, in an infinitesimal approximation, the distance between neighboring trajectories behaves exponentially as a function of time (see fig. 2.2).

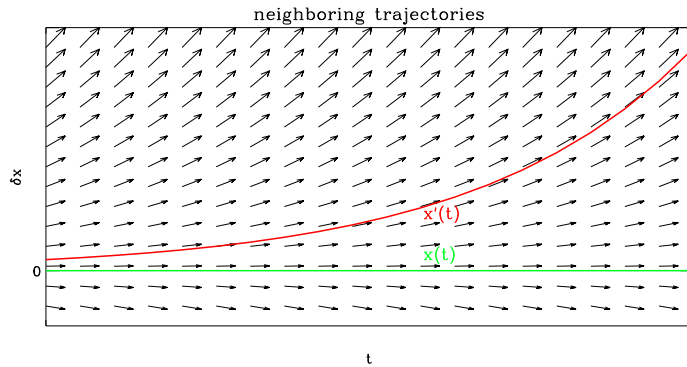


Fig. 2.2: In an infinitesimal approximation, the system is linear and the distance between trajectories behaves exponentially.

The *Lyapunov exponents* [59] formalize this idea. In the infinitesimal (i. e. linear) approximation, a small ball of initial conditions is deformed to an ellipsoid. The (local) growth is characterized by the growth exponents in the directions of the principal axes of this ellipsoid. These are averaged over time to get the *Lyapunov exponents* of the system. For details on the theory of Lyapunov exponents, see Benettin et al. [12]. The *maximum Lyapunov exponent* (MLE) is an important measure for predictability: if all Lyapunov exponents are negative, small uncertainties in the initial condition vanish as the system converges. In the positive case, there is at least one direction in which they grow. For a prediction using a finite-precision initial condition, this means that the slightest error in the direction of a positive Lyapunov exponent grows exponentially, making long term predictions of the system impossible. The MLE is a standard indicator for chaotic behavior, and will be useful in the study of the coupled map lattice in chapter 4.

Lyapunov exponents only measure the stretching mechanism of the system. For instance, the system

$$\frac{dx}{dt} = x \quad (2.4)$$

has a positive Lyapunov exponent, but a simple exponential behavior. For chaotic behavior, a folding mechanism is necessary to ensure that distant trajectories will eventually approach each other. This problem is addressed by the Poincaré recurrence theorem. To formulate it in its modern form, we need the notion of an invariant measure.

An *invariant measure* is a probabilistic approach in dynamical systems. The long term behavior of the system is described as a probability measure, assigning each subset of the state space the probability to be visited by a typical trajectory at a random time. If such a probability measure exists, it is invariant with respect to the time development. For chaotic oscillators, it is often supposed that a *natural invariant measure* exists, i. e. that the long term distribution of generic trajectories converges to a limit that is sufficiently well-behaved. For the Lorenz system, this was proven by Tucker [106] (cf. Fiedler [33]).

The original version by Poincaré [77] was written with respect to the volume of a vector space. A more general formulation in terms of measure theory can be found in Katok and Hasselblatt [46].

Theorem 2.1 (Poincaré recurrence theorem (cf. [46])). *Let $T : X \rightarrow X$ be a measure-preserving transformation on a probability space (X, Σ, μ) , and let $A \subset X$ be a measurable set. Then for any $N \in \mathbb{N}$,*

$$\mu(\{x \in A \mid \{T^n(x)\}_{n \geq N} \subset X \setminus A\}) = 0. \quad (2.5)$$

Idea of proof (cf. [77]). Let $B := \{x \in A \mid \{T^n(x)\}_{n \geq N} \subset X \setminus A\}$ as in eq. 2.5. Consider the 'tube-like' subset of X that is covered by the time development of B :

$$B^n := B \cup \dots \cup T^n(B). \quad (2.6)$$

Since T is measure-preserving, the measure of B^n is growing at a constant rate until $T^k(B) \cap B^k \neq \emptyset$. The total measure is finite, hence this must happen for finite k . This implies that $f^k(B) \cap B \neq \emptyset$ (else there would already be an intersection for lower k). Consequently, every set of positive measure contains a point with a recurring trajectory (or conversely, any set without recurrence points has measure zero). \square

Theorem 2.1 implies that *almost every* point is *recurrent*, i. e. its trajectory eventually comes back to an infinitesimal neighborhood of the point.

The idea of an invariant measure is related to the concept of *ergodicity*:

Definition 2.2. *Let X be a measure space with measure μ , and T a measure-preserving transformation. T is called **ergodic** if for every $E, H \subset X$ with positive measure there exists $n \in \mathbb{N}$, such that*

$$\mu(T^{-n}E \cap H) > 0. \quad (2.7)$$

Another formulation of ergodicity is that a system covers all available phase volume, i. e. a small ball E of initial conditions will eventually meet any open set H . In the long run, such a system tends to 'forget' its initial state and always converge to the same dynamical characteristics. This is a typical property for chaotic dynamics, as well as for many thermodynamic systems. A central property of ergodicity is that the time average of a function over a trajectory is equal to the 'ensemble average' over the state space, in some 'almost-everywhere'-sense that depends on the specific formulation.

The Lorenz and Rössler systems are *dissipative* in terms of the topology of the state space, i. e. there are open sets that are never revisited. This does not contradict the existence of an invariant measure, however the measure must vanish on any open set that is not revisited, i. e. it must be supported on the attractor. It is not necessarily a 'classic' volume measure because subsets of full dimension may have measure zero. The measure also might not have a density, i. e. sets of zero volume can have positive measure.

For such a measure, the Poincaré recurrence theorem applies, stating that *almost every* point is recurrent. Note that the genericity condition refers to the invariant measure. Since any 'leaving sets' in a dissipative system have measure zero, the theorem does not predict any recurring points outside of the attractor.

One of the most well known real-world examples for such a system is the earth's atmosphere, where the sensitivity of the weather is expressed in the famous metaphor of the *butterfly effect*¹.

¹This metaphor is attributed to Lorenz, relating to a talk held by him in 1972 with title 'Does the flap of a butterfly's wings in Brazil set off a tornado in Texas?'

2.1.2 Attractors

Even though the system state can typically not be predicted far into the future, there is much regularity in the dynamics of the chaotic systems discussed above. Therefore, it makes sense to ask for general dynamical information, considering the set of states that appear in the long term limit of typical trajectories.

The idea of an *attractor* of a dynamical system is a minimal set that attracts nearby trajectories. This is usually defined in the following way: it is closed with respect to the time development and there is an open neighborhood of initial conditions whose trajectories converge to the attractor. The specific formulations vary, for example in the kind of stability that is demanded. See Milnor [64] for a discussion of some commonly used definitions. The set of initial conditions whose trajectories converge to a given attractor is called its *basin of attraction*.

The classic forms of attractors are stable fixed points and stable limit cycles. The study of chaotic dynamics has led to another form: *strange attractors* (Ruelle and Takens [84]). These sets are typically non-manifold (and therefore do not have a topological dimension), and exhibit *fractal* [60] structures.

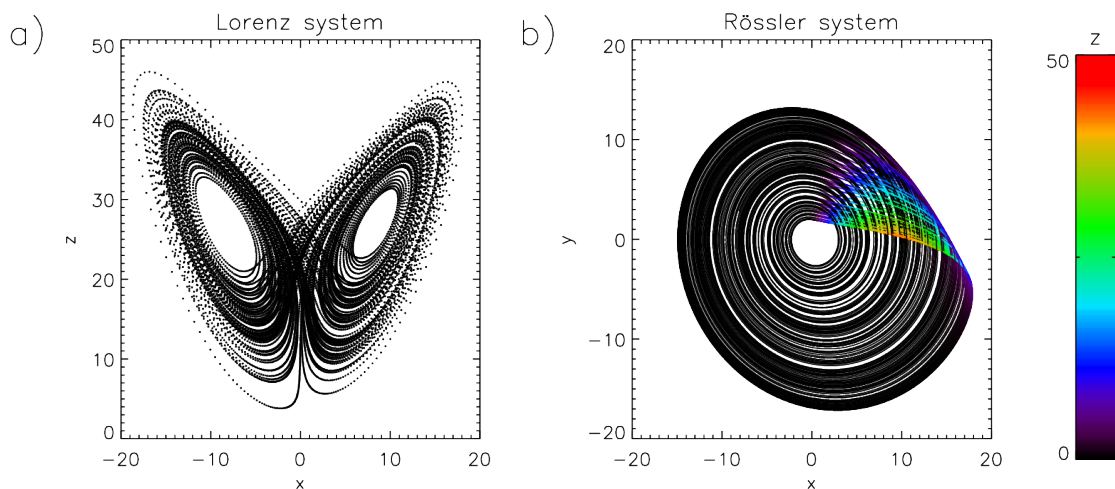


Fig. 2.3: Chaotic attractors: long term distribution in state space. a) Lorenz system (z versus x) b) Rössler system (y versus x). For the Rössler system, the color coding of the z -coordinate illustrates the folding mechanism.

The study of changes in the topology of an attractor as a function of the control parameters is the objective of *bifurcation theory* [97]. The studied features include the appearance and annihilation of stable or unstable equilibrium points and periodic orbits. The transitions between ordered and chaotic regimes are important objects of research, where bifurcation phenomena like periodic windows, period doubling cascades or intermittence behavior are explored.

2.2 Delay-Coordinate Embedding

When modeling a physical system, *state variables* are chosen to represent relevant degrees of freedom, and their time development is described by differential equations. Real world systems often have a state space of high and unknown dimension, and the difficulty of modeling is to

find an appropriate reduction to some relevant state variables, while preserving the essential mechanisms. As an example, one can think of the sino-atrial node – the natural pacemaker of a human heart – which is not only coupled to physiological variables like blood pressure, oxygen saturation, and breath rate, but is also influenced by a multitude of other sources, e. g. perceptual stimuli.

In experimental situations, the exact mechanisms of a system are usually unknown. Scientists study a set of observables, and hope to reconstruct the important dynamics of the system from this observation. The assumption is that in a coupled system any hidden parameters and variables will be represented in the observational data. Packard et al. [72] argue that in order to reconstruct 'phase-space pictures' of an n -dimensional dissipative system, it is generally enough to measure n arbitrary independent observables. Anticipating the mathematical theory by Takens, they propose to use time delayed copies $(y(t + \tau_1), \dots, y(t + \tau_n))$ of a single observable $y(t)$ as independent quantities. The τ_i are called delays, the vector (τ_1, \dots, τ_n) is referred to as the *sampling pattern*, and the values $(y(t + \tau_1), \dots, y(t + \tau_n))$ are called the *delay vector*. Packard et al. apply this *delay-coordinate embedding* to the Rössler system, estimating the attractor dimension and the MLE.

Note that the term 'embedding' is used in different senses. In mathematics, it refers to a property of a map to fully preserve certain topological properties. In physics, it usually describes the purpose of a map to transport dynamical information into some description space, using observables of the system. The aim is to conserve the topology of the attractor, but often such maps do not fulfill the criteria for an embedding in the strict mathematical sense.

In order to discuss the well known theorem by Takens, this section starts with a brief recall of mathematical terms needed to formulate a dynamical system in terms of differential geometry (see for instance do Carmo [26] for a detailed introduction to differential geometry):

1. A *diffeomorphism* is a bijective mapping, which is smooth in both directions (i. e. both the mapping and its inverse).
2. A (smooth) *manifold* is a set that locally resembles euclidean space².
3. A (smooth) *embedding* is a map $\varphi : A \rightarrow B$ that is a diffeomorphism on its image (i. e. on the image $\varphi(A)$, the differential structure coming from A and the one as a subset of B coincide).
4. A time-continuous dynamical system is defined by a *state space* M , which is a smooth manifold, together with a *vector field* v . The time evolution is given by the differential equation $\dot{x} = v(x)$. Hence, a trajectory is attained by following the *flow* of v from a given initial condition.

Note that some of the terms introduced above can refer to different levels of smoothness, like continuity, C^k (i. e. there exist k continuous derivatives), or C^∞ . The theorem formulated below demands at least C^2 -smoothness.

Takens proved that it is generally possible to reconstruct the full topology of the state space from the time series of a single observable³:

²There is an *atlas* of *charts* (U_i, ϕ_i) , mapping parts of the set to euclidean space $(\phi_i : U_i \rightarrow \mathbb{R}^n)$, such that the U_i form an *open cover* of M , their images $\phi_i(U_i)$ are open in \mathbb{R}^n , and the *transition maps* $\phi_i^{-1} \circ \phi_j$ are diffeomorphisms.

³The theorem is based on Whitney's embedding theorem [109], giving the existence of an embedding into euclidean space of dimension $2n$ for any compact manifold of dimension n .

Theorem 2.3 (Takens' Theorem [102]). *Let M be a compact manifold of dimension n . For pairs (φ, y) , where $\varphi : M \rightarrow M$ is a smooth diffeomorphism and $y : M \rightarrow \mathbb{R}$ is a C^2 -smooth function, it is a generic property that the map $\Phi_{(\varphi, y)} : M \rightarrow \mathbb{R}^{2n+1}$, defined by*

$$\Phi_{(\varphi, y)}(x) := (y(x), y(\varphi(x)), \dots, y(\varphi^{2n}(x))) \quad (2.8)$$

is an embedding.

In the case of a dynamical system as defined above, the manifold M is the state space of the system, or part of it. The theorem demands M to be compact, which a priori is not satisfied for many physical systems whose state spaces are part of \mathbb{R}^n . This can probably be resolved if the attractor is bounded.

The diffeomorphism φ refers to the time evolution of the system for a fixed *delay* τ . The function y is an observable of the system. In this case, the map Φ is a *delay embedding* into \mathbb{R}^{2n+1} , as defined above.

The term *generic property* means that it holds for *almost all* choices for the pair (φ, y) . It should be mentioned that terms like 'almost all', 'almost surely' or 'almost everywhere' are rigorous mathematical terms, even though they may sound colloquial. They are used in many parts of mathematics to state that the set of exceptions to a general statement is negligible in a well-defined sense. In the topological case used here, the generic property is true on an open dense subset of the corresponding function space. In probability theory for instance, *almost surely* means that the set of exceptions has zero probability.

In summary, Takens' theorem allows to map the state space as a whole to a euclidean space. Still this is not the best result one could imagine, in several aspects. First, it demands a compact manifold, which is a priori not given for most state spaces. Furthermore, the aim of a delay embedding usually is not to describe the state space, but the attractor. Since the attractor can have a considerably lower dimension than the state space, there is hope for a lower dimensional constraint if only the attractor is to be reconstructed.

Sauer et al. [86] proved several theorems that release constraints from Takens' theorem, focusing on the attractor instead of the whole state space. Instead of a compact manifold, they show a similar theorem demanding only a compact subset $A \subset \mathbb{R}^n$, and an embedding dimension larger than two times the *box-counting dimension* of A . Then, A can be chosen as the closure of the attractor. See also Bohn [15] for further discussions of mathematical aspects of delay-coordinate embedding.

Symbolic representations are closely related to the concept of time delay embedding. To define a symbolic representation, a value in a time series is considered together with future values at certain time delays (see section 3.1). The second step, namely the generation of symbols from delay coordinates, will be explained in detail in section 3.1.4. The parameters – embedding dimension and delays – are the same for delay-coordinate embedding and symbolic representations. Therefore, I will postpone the discussion about the choice of parameters to section 3.1.6.

2.3 Measures of Order

Interactions between oscillators can lead to collective behavior that is fundamentally different from the dynamics of the isolated system components. This section gives a collection of commonly used concepts to identify and describe different sorts of collective dynamics. The

aim is to find appropriate quantitative measures for characteristic properties of the respective dynamic regimes.

2.3.1 Synchronization

The word synchronization is used in a variety of contexts, some of more mathematical or physical meaning than others. The word's origin is Greek, meaning 'sharing a common time'. Usually it is used to describe systems with rhythmic dynamics exhibiting similar events at the same time, like synchronized clocks ticking in unison or an orchestra playing in a common beat. First, some examples are discussed of phenomena commonly referred to as 'synchronization'. While the term synchronization is mostly used in an informal and unspecific way, Pikovsky et al. [76] gives an explicit definition, which is discussed in the following.

Probably one of the first observations of synchronization in a modern scientific sense is attributed to Huygens, who was working at the problem of measuring the geographic longitude, which demands for highly accurate clocks. He observed that two pendulum clocks that were suspended from the same wooden beam would synchronize, with their pendulums swinging in opposite phase. He called the effect 'sympathy of two clocks' (cf. [76]).

The *circadian rhythm* of the human body is driven by an oscillator with a period of about 24 hours. It controls many important body functions that depend on the time of day, like temperature, alertness, level of certain hormones, blood pressure, desire for sleep, or sleep phases (see Strogatz [98]). The circadian pacemaker is located at the front of the hypothalamus, with a direct connection to the eyes. The main synchronization mechanism between the circadian clock and the outside world is the influence of daylight. The effect of interior lighting is small because even on a cloudy day, daylight is much more intense.

If the natural period of the internal clock deviates too far from the sleep-wake cycle, desynchronization can occur between the sleep times and the internal clock. This has been observed for blind people, in isolation studies, and in cases of shift work and jetlag. The circadian rhythm is also related to some kinds of insomnia, for example when people are regularly forced to go to bed at a time when their circadian pacemaker forbids sleeping (Lavie [53] and Strogatz et al. [100]).

In the study of model systems consisting of coupled chaotic dynamical systems, various synchronization regimes have been observed (see Rosenblum et al. [82], Bocalletti et al. [14]). For other examples from real-world and experimental systems, see also Rosenblum et al. [81], Glass [36], and Glass and Mackey [37].

Definition 2.4 (Pikovsky et al. [76]). **Synchronization** is an adjustment of the rhythms of oscillating objects due to their weak interaction.

To make definition 2.4 rigorous, the involved terms need to be specified. The term *oscillating object* refers to an active system that has its own source of energy, and some sort of steady rhythm, which is stable with respect to small perturbations. It is supposed to be autonomous, i. e. without explicit time dependence. The basic model for such an oscillator is a pendulum clock, and many commonly used examples for synchronization refer to systems with a stable limit cycle, which can be described by a *phase*.

Weak coupling, in the sense of Pikovsky's definition [76], means that the coupling forces are small enough, so they mainly act on the phase, instead of dragging the oscillating system off its attractor. Rigid coupling, where two systems follow the same trajectory by design, is

explicitly excluded, e. g. two clock pendulums connected by a rigid bar, so that there is only one degree of freedom left.

A *rhythm* in the sense of definition 2.4 is an oscillation cycle that is not necessarily periodic but usually supposed to be regular enough to allow the definition of an instantaneous phase. It can also have the form of regular events, where properties like frequency or oscillation period are defined. An adjustment is usually defined in terms of the frequencies (e. g. clocks with slightly different natural frequencies adjust their running frequency to a common value) or phases (e. g. clock pendulums swing *in phase* or *anti-phase*).

For examples of synchronization in the sense of Pikovsky, see for instance Rosenblum et al. [82], who used a system of two coupled non-identical Rössler oscillators to study transitions between different synchronization regimes defined by phase relations of the two oscillators. Synchronization in the above sense also includes the mentioned convergence of frequencies of detuned oscillators, intermittent synchronization or statistical correlation between phases.

As already mentioned, Pikovsky's formulation is relatively strict. Firstly, most practical implementations of synchronization measures rely on a well-defined phase, which is used to define an adjustment in terms of measures like the average frequencies or the phase difference distribution. While this works in systems like the Rössler or Lorenz system, in large ensembles or other high-dimensional systems it is not possible to define a meaningful phase. These cases demand for more general concepts, like measures for similarities and coincidences in the behavior of subsystems, or emerging order in spatially extended systems.

Definition 2.4 applies to a pair of systems, and the adjustment of rhythms usually is a scalar concept. Multiple time series can be related in more complex ways than such a scalar measure can represent. For instance, three time series can be pairwise independent but redundant as a triple: consider independent uniformly distributed binary random variables a , b . Then $c := (a \text{ xor } b)$ is statistically independent both from a and from b , but as a triple a , b and c are redundant (any one is determined by the other two). Constructions like this are used in *channel coding* for detecting or correcting errors (see for instance Cover and Thomas [24]).

Chapters 4 and 5 will deal with emerging order in spatially extended systems, which may or may not be connected with synchronization in the above sense. Therefore, an important part of the research objective of this work is to describe different synchronization-related phenomena of emerging order. The following sections will summarize some relevant concepts.

I should also mention a useful general description by Brown and Kocarev [17], which summarizes what most uses of the term *synchronization* have in common. In contrast to Pikovsky's synthetic approach (i. e. connecting different systems by coupling), they propose an analytic one decomposing a single dynamical system. Their description has four parts:

1. Subsystems are defined by decomposing the state space of a dynamical system into a product of subspaces.
2. Properties of the subsystems are defined.
3. A mode of comparison is defined for the above properties.
4. Synchronization means that the properties 'agree in time'.

The symbol based approach of the present work exceeds this formalism insofar as the properties do not have values in \mathbb{R}^n (like defined in [17]) but in a finite group. Furthermore, I use synchronization as a continuous concept allowing various degrees of synchronization, instead of the binary one proposed by Brown and Kocarev.

2.3.2 Complexity

The concept of *information entropy* introduced by Shannon [90] quantifies the amount of uncertainty in a discrete random variable with a given distribution. The basic idea is the expected amount of information that a message will yield, supposing that it consists of *iid* (independent identically distributed) symbols with a known distribution. Shannon's famous *source coding theorem* says that the information entropy of a signal is a lower bound to the expected size of a lossless compression for a sequence of discrete iid random variables. A signal with high entropy needs more effort to transmit, and typically is considered as more complex than a low-entropy signal. Bandt and Pompe [11] applied this concept as a complexity measure for symbolic representations.

Algorithmic complexity (or *Turing complexity* or *Kolmogorov complexity*) is a concept for the complexity of a data string. It is defined as the size of the shortest program that produces the data string as its output. Formalized via a *universal Turing machine*, this length is defined up to a constant, which makes the Kolmogorov complexity well-defined for large enough sequences. Note however, that it is not computable, because it includes the *halting problem*. Moreover, proving that a given program is the shortest is a difficult problem. The concept was developed independently by Solomonoff [95], Kolmogorov ([50], cf [22]) and Chaitin [22] with slightly different motivations.

While algorithmic complexity is the length of the shortest program to generate a data set, *computational complexity* (see [105]) or *logical depth* [13] is the computational cost to execute this program. For instance, most a random sequences have a high algorithmic complexity because the the program typically can not be made shorter than the string itself. In this case, the computational complexity is low (only one print operation per character of the string). Bennett [13] calls the idea behind algorithmic and computational complexity a

'... computerized version of the Occam's razor paradigm, which exhorts us to explain each phenomenon by the most economical hypothesis able to explain it at all.'

Lopez-Ruiz et al. [57] proposed an approach combining entropy and distance to randomness, resulting in a 'convex' measure that defines both completely ordered and completely disordered behavior as simple, with a maximum of complexity in between. In section 4.3.5, a similar complexity measure is applied to a symbolic representation.

Shiner et al. [92] distinguish three categories of complexity notions, using terms of *order* and *disorder*. The first category includes monotonic functions of disorder, for instance information entropy or algorithmic complexity. Functions of the second category are convex, with minima both for complete order and for complete disorder, with a maximum in between, like the preceding one by Lopez-Ruiz et al. [57]. The third category is made of increasing functions of order, for instance describing the amount of self-organization in a system, compared to completely random behavior. Following [92], concepts like this are sometimes used in evolution biology.

Generalizing the complexity measure of Lopez-Ruiz et al., they propose a measure $\Gamma_{\alpha\beta} := \Delta^\alpha \Omega^\beta$ based on a *disorder measure* Δ and an *order measure* Ω , which are supposed to be normalized to the interval $[0, 1]$. The proposed complexity measure can have the characteristics of all three categories, dependent on the parameters α and β . As a straightforward choice of measure, they suggest the normalized entropy $\Delta := S/S_{max}$ as a disorder measure, and $\Omega = 1 - \Delta$ as the order measure.

Whenever the attractor of a system is known, its size or complexity reveals much about a system's dynamics. In the case of chaotic dynamics, the corresponding strange attractors typically are non-manifold, and the usual measures (e.g. the topological dimension, or k -dimensional volume) vanish or are not defined. There exist various non-integer concepts of *attractor dimension* (see Farmer et al.[31]) for dynamical systems. For example, the *box counting* or *Hausdorff dimension*[40] only uses metric information. The *Rényi dimension* (Balatoni and Rényi[10], cf. [31]) gives different weight to parts of the attractor according to the probability that they are visited by a trajectory. The *correlation dimension* (Grassberger and Procaccia[38]) is formulated in terms of a single time series and does not require a reconstruction of the attractor.

2.3.3 Interdependence

In statistics, the most straightforward notion of interdependence is *correlation*, in the sense of a linear component in the relation between two or more random variables. The central idea behind this concept is to measure deviations from the mean in units of the standard deviation, leading to a universal measure that is independent of the nature and the dimension of the involved quantities. The idea was introduced by Galton[35] in the context of biological heredity (though he never mentions negative correlations). The commonly used *Pearson product-moment correlation coefficient* (or *Pearson's r*)[73] uses standard deviations from the mean, which corresponds to a model of normal distributions. As a measure of interdependence, Pearson's r is applicable to real-valued random variables.

If interactions can be neglected, a system is equivalent to the sum of its parts. Using this idea, one can look for systematic differences between the dynamics of a coupled system and those of its uncoupled parts. This description can be useful in cases where the parts on their own have complex dynamics and the coupled system shows emerging spatial or temporal order (which is what happens in the coupled system studied in chapter 4).

If the parts can not be observed on their own, an independent version of the time series can be artificially created. In section 3.2.4, this is done by comparing the joint distribution of two symbol sequences with the product of their marginal distributions.

The *Kullback-Leibler distance*[51] (or *relative entropy*),

$$d(p, q) := -\mathbb{E}_p \log_2 \left(\frac{dp}{dq} \right), \quad (2.9)$$

is a distance measure between two probability distributions p, q on the same event space. It is only defined if the support of p is part of the support of q (i.e. all events with positive probability in p have positive probability in q). Fig. 2.4 shows its behavior in the basic case of two events.

The Kullback-Leibler distance can be interpreted as the capacity loss when coding a sequence with a symbol distribution p with a code that is optimized for a different symbol distribution q . The Kullback-Leibler distance is highly sensitive to deviations at 'almost-forbidden' events with small probabilities, diverging to infinity if p gives positive probability to an event which is forbidden in q . This illustrates the restricted domain of definition: an optimal code would not define a symbol for a ' q -forbidden' event, hence it is not possible to code the corresponding message.

Note that the Kullback-Leibler distance is not a metric, because symmetry and triangle inequality are violated. The distribution p usually acts as a reference distribution, while

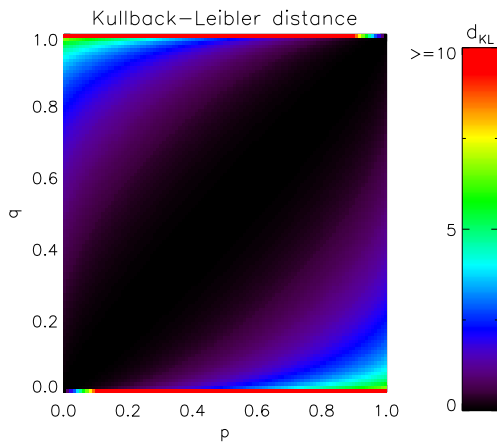


Fig. 2.4: Kullback-Leibler distance between two distributions on two events, which have the probabilities p and $1 - p$, or q and $1 - q$, respectively.

q describes a test distribution, e.g. the theoretical model and a measured sample, respectively. Whenever considering distances between multiple distributions, the asymmetry of the Kullback-Leibler distance demands a consistent way to label the involved distributions as reference and sample.

Section 3.2.3 will present an approach to turn the Kullback-Leibler distance into a metric. In the applications in chapters 4 and 5, the classification of reference and sample distribution will mostly be clear, so that the original measure can be used.

An essential part of synchronization as well as interdependence is the idea of different systems communicating with each other, therefore information flow is a useful concept. This approach seems most promising in cases where the information flow is conjectured to happen mainly in one direction, like in cases of asymmetric coupling. See Bahraminasab et al.[9] for an approach to quantify the information transfer from one time series to another using a directionality measure based on conditional mutual information.

Chapter 3

Symbolic Representations

This chapter is devoted to the methodology that is the main research objective of the present work: symbolic representations. Section 3.1 describes the central concepts, and connects them with formalisms used in related fields. The two complementary perspectives on symbols, referred to as *order patterns* and *permutations*, are compared. The set of symbols is described in terms of a partition of a time delay state space, illustrating parallels to delay-coordinate embedding. The structure of the partition is condensed to an $n-2$ -dimensional polytope, illustrating the structure of the ambiguities that arise if the entries of the delay vector are not pairwise different. Methods to resolve such ambiguities are proposed, suitable for either an information theoretic or an algebraic point of view.

A hierarchical structure – in the sense that short symbols are determined by long ones – is found for state- but not for transfer symbols. I explain that different sampling patterns are sensitive to different time scales. The invariance properties of symbolic representations under transformations of the underlying time series are studied, showing that especially the algebraic properties of transfer symbols are well-behaved.

In section 3.2, different concepts for the quantification of order properties are applied to symbolic representations. The aim is to provide a collection of measures that are applicable to a symbolic description and suitable for the context of different research questions. Commonly used distance measures on the symmetric group are summarized, which can be used for a pointwise comparison of symbol sequences. An approach to turn the Kullback-Leibler distance into a metric is discussed.

Section 3.3 is about the relations between symbols with different sequence lengths or overlapping delay vectors. The results are used to discuss the entropy rate of a symbol sequence.

3.1 Basics

As mentioned before, this work is about extracting information about dynamical properties of time series. Filtering for specific information often comes along with a discretization, leading to a coarse grained description of a time series. In information theory, the concept of information entropy [90] led to a variety of tools for the description of the properties and relations of such discrete information sources (see for example Cover and Thomas [24]).

In the field of *symbolic dynamics* (see Smale [94], Ott [71]), (time-discrete) dynamical systems are discretized in space by partitioning the state space into a finite number of subsets, each assigned to a symbol. An element of the state space is described by the symbol sequence of its trajectory, thus shifting the problem from the state space to a space of sequences, where different techniques are available. For example, the time development has the simple form of a shift-operation

$$(\dots, s_{-1}, s_0, s_1, s_2, \dots) \mapsto (\dots, s_0, s_1, s_2, s_3, \dots). \quad (3.1)$$

Generally, this discretization leads to a loss of information. However, there are cases where a *generating partition* exists, providing a one-to-one relation between the state space and the space of symbol sequences.

Band and Pompe [11] introduced a different approach of discretization, using local *rank orderings*¹ (also called *order patterns*) to describe a time series by a sequence of permutations. Section 2.2 explained how this can be written as a partition of a suitably defined state space. Rank orderings were used to distinguish random and chaotic behavior [2] [4] and to measure complexity [5] [11]. Note that, even though the term *permutation* is sometimes used, the methods described in the above references treat order patterns purely as a set of elements, without any additional structure.

In this work, the set of permutations is studied from the perspective of its algebraic structure. Monetti et al. [65] use the algebraic structure of the symmetric group to introduce *transfer symbols*, a description of the relations between the symbolic representations of two time series. Also note recent work by Amigo et al. [3], which defines complexity measures in terms of transfer symbols. The aim of this chapter is to explore the new concepts and structures that arise when regarding this symbolic description from an algebraic perspective.

3.1.1 Main Concept of State and Transfer Symbols

Suppose that a human observer is asked to describe in a few words the essential features of a piece of time series, for example from a financial index. The result would be a statement like

'It has an upwards trend, with a small dip in the second half.'

A description like this neglects exact numbers and captures local patterns in the time series by considering the relations of nearby points.

When describing a time series in the neighborhood of a time t , the simplest version of the above filtering is to ask if the series increases or decreases, comparing points at t and $t + \tau$. The generalization of this is to examine longer sequences of values for their rank order. In order to introduce the general concept, I briefly summarize the required mathematical terms here. A precise discussion of the formalism will be given in section 3.1.3.

¹The use of rank orders was already proposed by Spearman [96] in the context of statistical correlation, where it gives robustness against outliers.

Given a finite set $A := \{x_1, \dots, x_n\}$, a bijective mapping of A into itself is called a *permutation* of A . Note that the composition of maps is associative, the identity map is a neutral element, and each bijective map has an inverse. Thus, the composition of maps defines a group structure on the set of permutations. For $A := \{1, \dots, n\}$, this group is called the *symmetric group*, and noted by S_n ².

In calculations, it is common to write permutations in *cycle notation*: a k -*cycle* (x_1, \dots, x_k) denotes a permutation that maps each element x_i to x_{i+1} , and x_k to x_1 . It is straightforward to see that every permutation can be written as a composition of disjunct cycles, which commute and are unique (up to sequential rearrangement). The permutation that generates the rank order of a vector is called its *symbol* (see fig. 3.1).

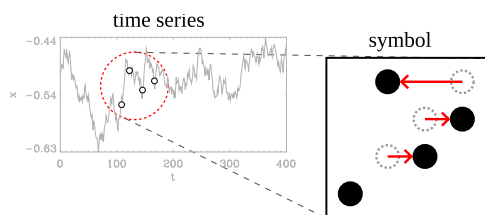


Fig. 3.1: State symbols of a time series: short subsequences are described by the permutations that generate their rank order. In this example, the generating permutation is a three-cycle.

Definition 3.1 (Symbols [11]). Let $v := (v_1, \dots, v_n)$ be a vector of pairwise different real numbers. The **symbol** of v is the unique permutation $a \in S_n$ with

$$a(i) > a(j) \quad \forall i, j = 1 \dots n \quad \text{with} \quad v_i > v_j. \quad (3.2)$$

Definition 3.2 (State Symbols). Let $x(t)$ be a time series and $\tau := (\tau_1, \dots, \tau_n)$. The symbols of $v := (x(t+\tau_1), \dots, x(t+\tau_n))$ form a sequence of symbols, which are called the **state symbols** of x . The vector τ is referred to as the **sampling pattern**, and τ_1, \dots, τ_n are called **delays**.

The sequence of state symbols is also called a *symbolic representation* of the time series x . Due to the connection to time delay coordinates (see sections 2.2 and 3.1.4), v is often called a *delay vector* in the literature. In definition 3.1, the assumption that v has pairwise different entries has a technical reason, section 3.1.5 will explain how to avoid this constraint. Note that, in order to be precise, I avoid the term 'symbol' for specific constructions and speak of 'state symbols' when describing local features of a time series with a sequence of symbols. Later, I will also use τ as a scalar, referring to the equidistant sampling pattern $(0, \tau, 2\tau, \dots, (n-1)\tau)$.

The state symbols were defined in terms of a single delay vector. When dealing with two rank orders, the natural construction is the permutation that transforms one into the other. Monetti et al. [65] introduced this concept, called *transfer symbols*, to describe the relations between two time series.

Definition 3.3 (Transfer symbols [65]). Let $a, b \in S_n$ be symbols. The **transfer symbol** from **source** a to **target** b is the permutation that generates b when applied to a .

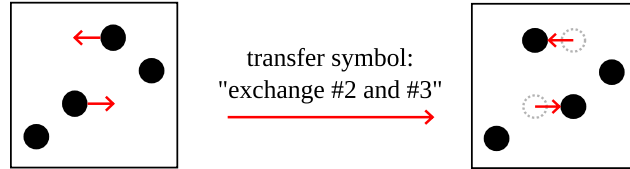
This definition also makes sense when considered from a group theoretic perspective, because the term $a^{-1}b$ coincides with the difference between two group elements (see fig. 3.2). The fact that permutation groups are not commutative leads to transfer symbols not being symmetric with respect to an exchange of source and target. Since

$$a^{-1}b = (b^{-1}a)^{-1}, \quad (3.3)$$

²Note that the permutation group of any set with n elements is isomorphic to S_n .

the exchange of source and target leads to an inverse transfer symbol, similar to a difference or quotient.

Fig. 3.2: A transfer symbol between two rank orders is defined as the permutation that transforms one into the other. The red arrows indicate the action of the transfer symbol from a to b .



3.1.2 The Conceptual Difference between Rank Orders and Permutations

The concept of symbols combines two different viewpoints, which I refer to as *rank orders*³, and *permutations*. This section explains the difference between these viewpoints.

A rank order defines a *total order* on a finite set, i. e. for two elements it always defines one that is ranked higher. Considering a set of n tasks, a rank order is a list, defining an order in which the tasks are to be done. The set of possible lists has $n!$ elements. From this viewpoint, the set of symbols is a homogeneous set of lists, with no additional structure and no prominent elements. For example, there is no canonical list that is simpler or more canonic than any other. However, it is natural to think of distance measures, for instance considering two lists as close to each other if they agree on the position of many tasks. When considering a sequence of rank orders, it is natural to treat them like a sequence of unrelated objects, using their distribution, i. e. 'how variable are the relative frequencies?', or 'are there any elements that do not occur at all?', or defining distance measures. There is no straightforward concept of composing two lists.

In contrast, a permutation is a transformation that rearranges the elements of a list. For example:

'Move item #5 to the top, lowering items #1 – 4 by one rank.'

The set of permutations also has $n!$ elements, but a different structure. Two such rearrangements can be composed by applying them one after another, and the result is again a permutation. This composition equips the set with the structure of the *symmetric group*. The elements have intrinsic algebraic properties, for example there exists a simplest transformation (*'keep everything as it is'*). Moreover, some transformations are their own inverse, while others are not. One can form equations, for example considering the 'difference' between a pair of permutations (i. e. the element that transforms one into the other).

In conclusion, the set of order patterns and the group of permutations have a fundamentally different structure, even though they can formally be identified with the same set of elements. The state symbols introduced above are closer to the 'rank orders' perspective, while the transfer symbols are on the 'permutations'-side.

The relations between these perspectives can be investigated by considering important properties or *morphisms* (transformations that are compatible with a structure) that are natural from one perspective, and describing them in terms of the other viewpoint. Section 3.3 will do this for the transformation between different sequence lengths, which is straightforward in the 'rank orders' perspective but complex from an algebraic point of view.

³Also called *order patterns* in the literature, see for example Amigó [2] [4], or Groth [39].

3.1.3 The Symbolic Formalism

There exist several notations and conventions that apply to rank orders and their associated permutations. Since the conventions of different fields may deviate from each other, it is of importance that the appearance of the equations does not depend on the viewpoint (e. g. if a variable is interpreted as a rank order or as a permutation). In this section, the formalism used in this work is presented and compared to other notations from related fields. Since not all common conventions are compatible, non-intuitive notations can not always be avoided.

Symbols

Definition 3.4. *The group of permutations of n elements is defined as the set of functions*

$$S_n := \{a : A \rightarrow A \mid a \text{ bijective}\}, \quad \text{where } A := \{1, \dots, n\}. \quad (3.4)$$

The relation between these functions and the exchange of objects can easily lead to misunderstandings, hence it is important to first make clear the terms used in this context:

Definition 3.5 (Items and positions). *Let $a \in S_n$ be a permutation. Then, $a(i) = j$ is understood as*

'The new item on the position i is the one from position j .'

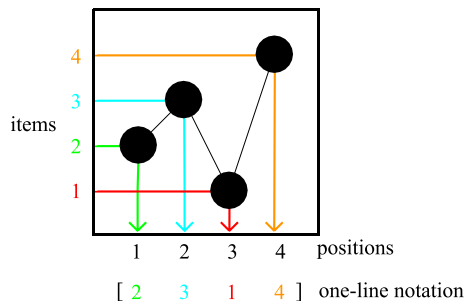


Fig. 3.3: Items and positions. $a(i) = j$ means that *item* number j is put on *position* number i . Note that the arrows point from $a(i)$ to i , which is a possible source of confusion (and a consequence of the mathematical standard notation for permutations).

Elements of S_n can be referenced in several ways (specific expressions are given for $n = 4$, wherever considered helpful). Let $a \in S_n$ be a permutation.

- a) The most straightforward way to write down a function is to state its value for every possible argument, in the so-called *two-line notation*:

$$\begin{pmatrix} 1 & 2 & \dots & n \\ a(1) & a(2) & \dots & a(n) \end{pmatrix}. \quad (3.5)$$

Since the first line is canonical, it is enough to write down the second one,

$$[a(1), \dots, a(n)], \quad (3.6)$$

which is called *one-line notation* and in this work is always denoted in square brackets, in order to avoid ambiguities.

- b) A further important convention is *cycle notation*: as mentioned, any permutation can be written as a product of disjunct *cycles* of the form

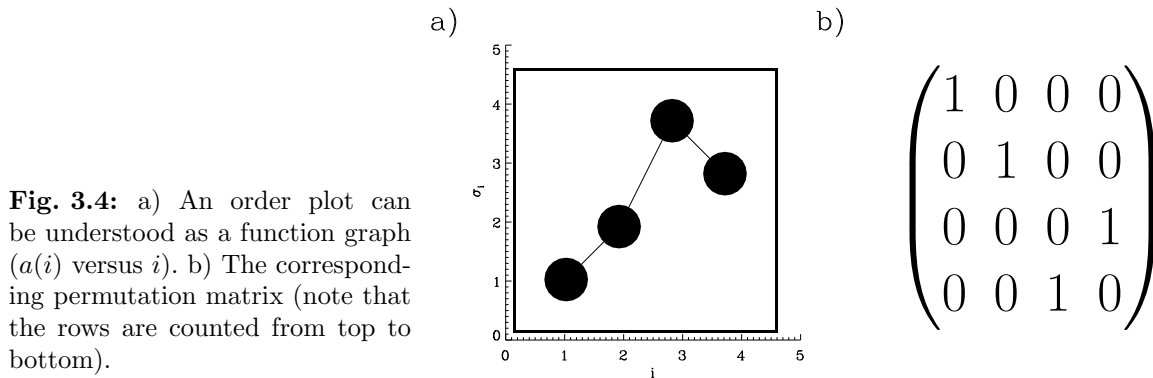
$$(x, a(x), a^2(x), \dots, a^{k-1}(x)), \quad (3.7)$$

where k is the minimal positive integer for which $a^k(x) = x$, and those cycles are unique (up to sequential rearrangement). Note that, for the given notation, a cycle $(1, 2, 3, 4)$ shifts the entries of a 4-vector to the left, i. e. the new entry on position 1 is the one from position 2, etc. For both one-line and cycle notation, I will omit commas, as long as the expressions are still unambiguous, e. g., for $n < 10$ it is clear that each digit stands for a number.

- c) For visualizing a symbol, I use diagrams of $a(x)$ versus x (fig. 3.4a), which I refer to as an *order plot*. Definition 3.5 implies that the rank order of a delay vector is associated to the permutation that generates this rank order when applied to the columns of an ascending rank order. This implies that an exemplary delay vector with entries 1, 2, 4, 3 corresponds to a state symbol with one-line notation [1243]. As a result, the one-line notation (and the order plot) of a state symbol is a discretization of the corresponding delay vector.
- d) Permutations can be written as *permutation matrices*. The matrix $A \in \mathbb{R}^{n \times n}$ that corresponds to a permutation $a \in S_n$ is defined by

$$A_{ij} := \begin{cases} 1 & \text{if } j = a(i) \\ 0 & \text{else.} \end{cases} \quad (3.8)$$

Note that, by convention, the rows of a matrix are counted from top to bottom, while the ordinate of an order plot is oriented from bottom to top, which is a potential source of confusion (compare fig. 3.4a and b).



Composition of Symbols

The group of permutations is not commutative. Therefore, it is important to bring together the different conventions about left and right actions. The standard way to define the composition of permutations is the convention for the composition of functions:

$$(ab)(i) := a(b(i)). \quad (3.9)$$

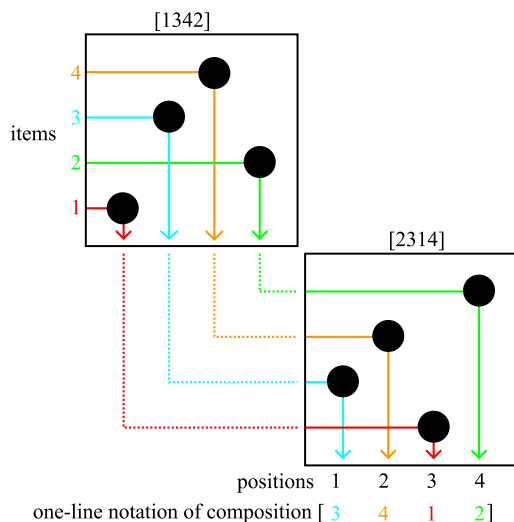


Fig. 3.5: Composition ab of two order plots $a = [1342]$ and $b = [2314]$.

This formulation comes from the original definition 3.4. In principle, this is enough to make all symbol equations of this work well-defined. However, for reasons of clarity, I will briefly explain how the composition looks like in terms of the other notations. As a numeric example, I consider the symbols $a := (234) = [1342]$ and $b := (123) = [2314]$, and their composition $ab = (13)(24) = [3412]$.

- a) In the cycle notation, consider the composition example $(234)(123)$, evaluated on the argument 2. The right cycle acts first, mapping 2 to 3, which is then mapped to the final result 4 by the left cycle (similarly for all other arguments). This corresponds to the formulation

$$(234)(123) = (13)(24).$$

- b) Fig. 3.5 illustrates the composition of two order plots, placing item $a(b(i))$ at position i . Note that the arrows point from $ab(i)$ to i (same as in fig. 3.3). This perspective translates as

$$[1342][2314] = [3412].$$

- c) Now consider the action of a permutation on an order plot. From the perspective of an order plot a , the action of b permutes the output of a (see also fig. 3.5): item $a(i)$ now goes to position $b^{-1}(i)$ (instead of position i). This corresponds to b permuting the *columns* of a , or more exact:

'the new column $b^{-1}(i)$ shall be the one that was column i before',

which is equivalent to

'the new column i shall be the former column $b(i)$ '.

This perspective corresponds to the formula

$$[1342](123) = [3412].$$

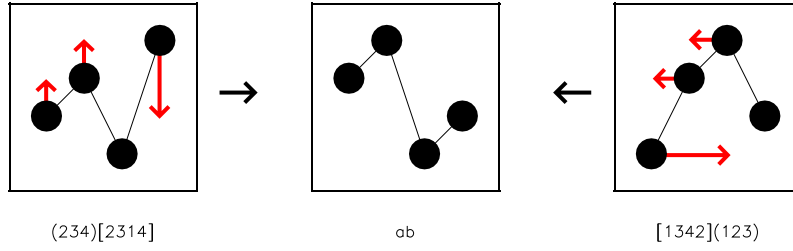


Fig. 3.6: Example ($n = 4$). The composition ab of symbols $a := (234) = [1342]$ and $b := (123) = [2314]$ can be interpreted as a left-action of a on b (left side), or as a right action of b on a (right side). Both lead to the same symbol $ab = [3412]$ (middle).

Conversely, from the perspective of an order plot b , a exchanges the items before they enter b (sending item $a(i)$ instead of item i), corresponding to a^{-1} permuting of the *rows* of b . This formulation translates as

$$(234)[2314] = [3412].$$

In summary (see also fig. 3.6),

$$ab = \begin{cases} b \text{ permuting the columns of } a \text{ (right action of } b \text{ on } a) \\ a^{-1} \text{ permuting on the rows of } b \text{ (left action of } a \text{ on } b). \end{cases} \quad (3.10)$$

In this work, the term 'apply a permutation to a rank order' refers to the right action, if not explicitly specified otherwise.

- d) It is straightforward to check, that the multiplication of matrices works analogous to the reasoning for order plots, but we should take a look at how row and column vectors are included in the formalism of matrix multiplication. One-line notations can be interpreted as row vectors:

$$[a(1), \dots, a(n)] = [1, \dots, n]A = 1A, \quad (3.11)$$

with a and A as above. Note that row vectors are written in square brackets, in order to prevent ambiguities with the cycle notation. For the column vector, this implies

$$A = A 1 = A[1, \dots, n]^T = ([1, \dots, n]A^T)^T. \quad (3.12)$$

Hence, the column vector that corresponds to the matrix representation A (and the symbol $a = [a(1), \dots, a(n)]$) is

$$[a^{-1}(1), \dots, a^{-1}(n)]^T. \quad (3.13)$$

- e) In programming, symbols are usually composed via *index notation*, where (examples for a, b as above)

$$a[b] := ab = [1342][2314] \quad (3.14)$$

is translated as '*in the array [1, 3, 4, 2], take the entries at the position 2, 3, 1 and 4*'. In this formulation, the index notation is compatible with the rest of the formalism discussed here.

Transfer Symbols

A transfer symbol was introduced as the permutation that connects two rank orders. Formally, this can be understood as a left or right action. For two symbols a and b , the transfer symbol t , as introduced by Monetti et al. [65], refers to the right action: $at = b$, which is equivalent to

$$t = a^{-1}b. \quad (3.15)$$

This is the permutation that generates b , when applied to the columns of a (see fig. 3.2). Alternatively, a left-action transfer symbol t' can be defined by $t'a = b$, which leads to $t' = ba^{-1}$. When not explicitly stated otherwise, the term *transfer symbol* refers to the right action.

Concerning the relation between right- and left-transfer symbols, consider two pairs of symbols with the same (right-) transfer symbol,

$$a^{-1}b = A^{-1}B. \quad (3.16)$$

Then, the symbols differ by a common factor

$$Aa^{-1} = Bb^{-1} =: c. \quad (3.17)$$

The left-transfer symbols are ba^{-1} and

$$BA^{-1} = cba^{-1}c^{-1}. \quad (3.18)$$

Thus, one version of the transfer symbol determines the conjugacy class (see definition 3.7 in section 3.2.1) of the other. Setting $c := a$ leads to

$$t = a^{-1}b = a^{-1}(ba^{-1})a = a^{-1}t'a. \quad (3.19)$$

Therefore, both versions of a transfer symbol share the same conjugacy class. Furthermore, for fixed t , any a may appear, hence t' can be any element from this class.

3.1.4 Symbols as Partition of a State Space

Using the concept of *time delay coordinates* described in section 2.2, a symbolic representation can be formulated as a partition of a time delay state space. Let $x(t)$ be a real valued time series, and $\tau = \{\tau_1, \dots, \tau_n\}$ a sampling pattern. Then,

$$y(t) := (x(t + \tau_1), \dots, x(t + \tau_n)) \quad (3.20)$$

is an n -dimensional delay-coordinate embedding of x . Since the state symbol of x with sampling pattern τ at time t is a function of $y(t)$, the set of symbols for sequence length n corresponds to a partition of \mathbb{R}^n into $n!$ subsets.

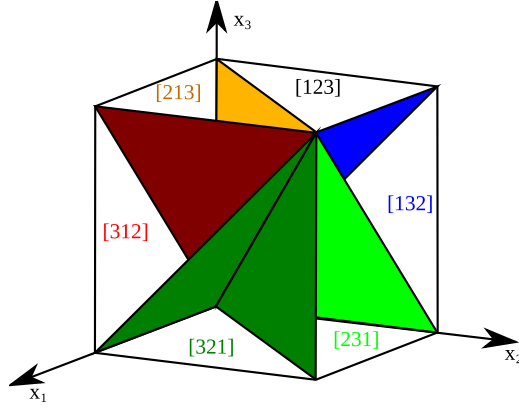
The borders of these subsets are given by the hyperplanes

$$\{(x_1, \dots, x_n) \mid x_i = x_j\} \quad \text{for } i, j \in 1, \dots, n, \text{ with } i \neq j. \quad (3.21)$$

Fig. 3.7 illustrates the partition for $n = 3$ (cf. Groth [39]). There are three planes, which intersect in the diagonal $x_1 = x_2 = x_3$. A view along the diagonal gives a clear picture about the situation in dimension $n = 3$. The partition of \mathbb{R}^n is symmetric with respect to diagonal shift,

$$(x_1, x_2, x_3) \mapsto (x_1 + a, x_2 + a, x_3 + a), \quad (3.22)$$

Fig. 3.7: Symbols of sequence length $n = 3$ as a partition of \mathbb{R}^3 in $n! = 6$ subsets. The figure shows the separating planes, restricted to the unit cube.



and scalar multiplication,

$$(x_1, x_2, x_3) \mapsto (\lambda x_1, \lambda x_2, \lambda x_3). \quad (3.23)$$

Eq. 3.22 implicates that the partition is the same on all planes perpendicular to the diagonal, hence it is enough to consider it on one such plane (for instance the one containing the origin). Furthermore, eq. 3.23 implies that the elements of every ray $\{\lambda x | \lambda > 0\}$ are mapped to the same symbol. Consequently, the partition of \mathbb{R}^n can be expressed as a tessellation of a $n-2$ -dimensional sphere S^{n-2} . In the above example with $n = 3$, this sphere is a circle. Therefore, the symbol of a point in 3-dimensional delay coordinates is determined by its angle around the diagonal (compare with fig. 3.7).

Note that any rank order can be transformed into any other by permuting the timestamps of the data points. In the n -dimensional time delay state space, each transposition of timestamps corresponds to a reflection. Thus, any two subsets of the partition are congruent up to reflections.

In the following, I will give some detail for dimension $n = 4$. There, the above mentioned sphere is 2-dimensional, therefore the partition can still be visualized. Note that the term 'visualization' refers to the object embedded in 3-dimensional space, and not the 2-dimensional projection in fig. 3.8. The graph of its connections reflects the structure of the set of rank orders of sequence length 4. On the sphere, the partition forms a *polytope*. Its *faces* correspond to the symbols, and their connections describe the ambiguities at the transitions between different symbols. The structure of the polytope is given by the following reasoning:

1. Each symbol corresponds to a face. Hence, the polytope consists of $n! = 24$ faces, which are congruent up to reflections (as noted above).
2. An *edge* corresponds to one pair of equal values in the delay vector. Each rank order has $n-1$ pairs of values that can be made equal by a continuous deformation without meeting other ambiguities in between (namely points with ranks $(k, k+1)$, for $k = 0 \dots n-1$). Consequently, each face has $n-1$ edges.
3. At a *vertex*, two such ambiguities come together. This can happen in the form of either two pairs or one triple of equal values, therefore there are two different kinds of vertices. Note that for general n this reasoning starts with subspaces of dimension $n-3$, and ends with vertices of dimension 0.

4. In the 'two pairs' ambiguity, each pair can be resolved independently. Since there are two ways to resolve each pair, these vertices are connected to four edges (and four faces).
5. The 'triple'-ambiguity can be reduced in six ways ('choose one of the three points and either raise or lower it'), therefore these vertices are connected to six edges and six faces.
6. Each face has one 'two pairs'-vertex (partition of the delay vector in upper and lower half) and two 'triple'-vertices (either the upper or the lower three points are equal). Thus, the polytope is made of six 'two pairs'-vertices and eight 'triple'-vertices.

These conditions fully determine the polytope shown in fig. 3.8. Starting from a cube, it can be formed by putting a four-sided pyramid on each of the square faces.

Note that the natural distance between faces of the polytope (i. e. the number of boundaries one has to cross to get from one face to the other) corresponds to the *Kendall tau* distance between rank orders, as defined in section 3.2.2. Note also, that the structure of the polytope is still based on the 'rank orders'-domain, i. e. it does not make use of the algebraic structure. However, it already contains more structure than has been used so far in the context of symbolic representations.

3.1.5 Uniqueness of the Representation

If a delay vector contains multiple entries of the same value, its symbol is not well-defined. This is why I excluded this case in definition 3.2. There are basically two ways to resolve such an ambiguity: one of the candidates can be chosen either with a canonical rule, or at random. Both methods have their own advantages and drawbacks, which will be discussed here.

From a purely information theoretic point of view, a main interest is the variation of a symbol distribution. From this perspective, a given delay vector is expected to always correspond to the same symbol, hence a canonical choice seems natural. For instance, one can define the canonical rule to rank any pair of equal values in a time series in increasing order, i. e. treating the first point as the lower one. The drawback here is that the symbol candidates for one vector can have quite different algebraic properties. The extreme example is the constant delay vector, which equally fits to any symbol. This way of resolving the ambiguity can break symmetries of the system, and introduce a considerable bias in the distribution of algebraic properties. For instance, the ambiguous symbol [2231] can be assigned to the self-inverse symbol [3241], as well as to the 4-cycle [2341]. In the view of a partition of the state space (section 3.1.4, especially fig. 3.8), a canonical choice corresponds to mapping each boundary point to one of the faces it touches. In this formulation, it is obvious, that any such mapping breaks the symmetry of the partition geometry. In conclusion, this canonical choice performs well if one is interested in entropies, but potentially introduces a bias when doing algebra like modding out symmetries of S_n and working with equivalence classes (see section 3.2.1).

The second way to resolve ambiguities is a random choice. In real world measurements, the observed signals contain some amount of noise. Consequently, even if a system comes back to a previous state, the exact repetition of a measured value is a zero-probability event (supposing a sufficient output accuracy). This way of resolving ambiguities can be modeled by choosing one of the eligible symbols randomly. See fig. 4.13 for a practical example. This method is robust when considering algebraic properties, because it does not introduce a bias, even though the occurrence of ambiguities has a blurring effect on the symbol distribution. Therefore, the random choice is natural from an algebraic point of view. The drawback is that

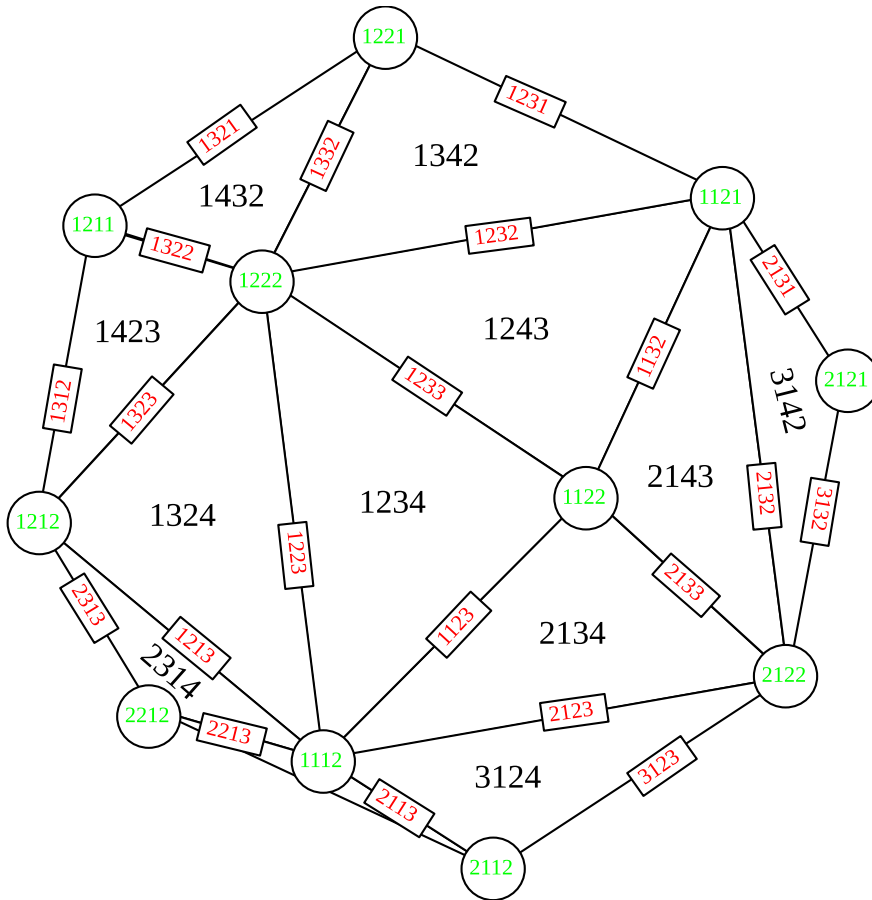


Fig. 3.8: The polytope representing the connections between the symbols of sequence length $n = 4$ (square brackets omitted for brevity). The faces (black) correspond to the symbols without ambiguities, the edges (red) have one ambiguous pair of values, and the vertices (green) are generated by two ambiguous pairs.

this way introduces variation whenever the vector is 'simple'. The extreme example is again the constant delay vector, which is blurred to a uniform symbol distribution. In conclusion, random choice is a useful method when working with algebraic properties, and an unfavorable one when using entropy measures.

In numerical simulations, it can even be useful to create artificial ambiguities. When working with canonical choice, this method give some robustness against measuring noise. Furthermore, since computers are deterministic but not exact, floating point numbers not only have finite accuracy (which in many cases can be considered as internal noise), but they also discretize the phase space of a complex system, which can change the quality of the dynamics. As an example, consider a stable fixed point that attracts the whole phase space. A numerical simulation discretizes the system in space and time. This is negligible in most regions, but around the fixed point, there can exist new periodic orbits in the discrete system. Therefore, when using amplitude-independent measures like symbols on this systems, those small errors can lead to considerable artifacts. In this work, small differences are considered as ambiguities, either by adding noise (corresponding to random choice), or by treating nearby values as

ambiguous (for canonical choice).

3.1.6 Embedding Parameters

By showing that an optimal result can be assured in the limit of infinite accuracy, the mathematical part of section 2.2 provides an important justification for the method of delay-coordinate embedding. The theorems of Takens [102] and Sauer et al. [86] state that from a mathematical point of view the embedding parameters n and τ do not matter, as long as the embedding dimension is large enough. In a physical application however, many of the mathematical issues become secondary and new difficulties arise. This is due to different objectives, as well as different assumptions about the problem:

In differential geometry, a focus is on compact manifolds, for which the strongest results can be proved. Mappings are considered as exact (i.e. noise-free), and the aim is a perfect one-to-one mapping, preserving topological structure exactly. Since noise is not considered, the mapping is reversible, and it is irrelevant if features are contorted or scaled down.

In contrast, in physics, delay embeddings are typically used for experimental data. The state space of the system (or even its dimension) is often unknown. The measured time series have finite precision and are contaminated with noise. It is not enough to preserve the topology of the attractor, because important features may be contorted or scaled down, such that they vanish under observational noise. The aim is not a perfect but a reasonable reconstruction of the attractor, containing its main features in a way that is robust against observational noise. Moreover, it is often acceptable to sacrifice some details in order to reduce the embedding dimension. Therefore, in an experimental situation, there is a need for an appropriate compromise between the quality and the cost (in terms of the required sample size) of the mapping.

When sampling a space, the number of samples corresponding to a given resolution grows exponentially with the dimension, this fact is called the *curse of dimensionality*. As a consequence, the amount of available data prevents the use of high embedding dimensions. This is why attempts to reconstruct the full attractor usually focus on low-dimensional chaos. In practical approaches, good results are attained already for lower embedding dimensions. For instance, Packard et al. [72] uses a 3-dimensional embedding for the attractor of the Rössler system, while the theorems demand 5 (Sauer et al. [86]) or 7 (Takens [102]).

Algorithms for Low-Dimensional Chaos

In the context of low-dimensional chaos, one is often interested in reconstructing the attractor of a dynamical system. Various algorithms have been proposed for the choice of optimal embedding parameters n and τ .

One approach for finding optimal delay times τ is to demand that a delayed copy is complementary to the original time series. In an information theoretic sense, this corresponds to a minimum of the mutual information (see Fraser and Swinney [34]) between the original and a time-delayed copy of the time series. Liebert et al. [55] and Kennel et al. [48] propose a topological approach that aims to detect false nearest neighbors in the reconstruction space. Buzug and Pfister [21] introduce geometric measures to quantify how much an attractor is spread out over the available space in the time-delay state space. Pecora et al. [74] propose a *continuity statistic* to find the maximum number of independent delay coordinates, and an *undersampling statistic* as a self-consistency test against overly large time delays or embedding dimension.

Note that the mentioned approaches, as well as the considerations in the following sections, include non-equidistant sampling patterns, which are not covered by the discussed theorems. However, it seems reasonable to expect that in practice the statement of the theorems is robust against this kind of modification.

In many real-world systems, where the dimensionality of the state space is large or unknown, one can not hope for a full reconstruction. In these cases, the aim is to capture certain aspects of the dynamics using a limited amount of measured data. Finding an appropriate sampling pattern is not necessarily about maximizing the captured information (i. e. finding complementary observables). Instead, the parameters must be chosen according to the research question.

Moreover, the algorithms mentioned above optimize the parameters for a dynamical system with fixed parameters. However, in the examples of the following chapters as well as in other real-world systems, one often wants to use the same description method for multiple configurations, in order to recognize for instance dynamical regimes, or to estimate control parameters of the system.

Sequence Length

Same as the embedding dimension in the case of delay-coordinate embedding, the sequence length n determines the size of the description space. A symbolic representation has values in the group of permutations S_n , which has $n!$ elements, hence the sequence length n determines how much information a symbol sequence can contain.

For practical purposes, the most important limitation to the sequence length is due to the number of possible symbols, which is $n!$. Most methods involve a symbol distribution. The required sample size poses a strong restriction on n . This work mainly uses sequence length 4 and 5. For long symbols, it still makes sense to ask for algebraic properties of single symbols.

Concerning the relationship between symbolic representations of different sequence length, I find a hierarchical relation for state symbols: long state symbols contain all the information of shorter ones, in the following sense:

Remark 3.6. *Let s_1 and s_2 be symbolic representations of the same time series, with respect to the sampling patterns τ^1 and τ^2 . If τ^2 is a subset of τ^1 , then s_2 is a function of s_1 . This follows from the fact that the rank order of a set determines the rank order of any subset. Note that this may cease to be true when passing to transfer symbols, or derived measures like symbol classes.*

In the case of transfer symbols, a reduction of information takes place, and a priori it is not clear if the information contained in a short transfer symbol is part of the information of a longer one. In section 3.3.1, it will be shown that indeed a short transfer symbol generally holds additional information compared to a longer one, even though it is based on a subset of the same data.

Now let us consider the situation for long sequence length $n \rightarrow \infty$. For constant τ , one symbol finally covers the whole time series. The rank ordering corresponds to a rescaling of the values, such that they fit a uniform distribution. In this context, Amigó [4] provides growth estimates of sets of forbidden state symbols in recurrence maps in the limit $n \rightarrow \infty$, based on results of Elizalde [30] on permutations avoiding generalized patterns.

In the continuous case, the limit $n \rightarrow \infty$ can alternatively be considered as an increasing sampling density within a fixed time horizon $T := (n-1)\tau$. If a continuous function is evaluated

with an increasing sampling rate, the symbol converges to the continuous case, i. e. the function is restricted to an interval of length T , and rescaled nonlinearly, such that the values are uniformly distributed.

Sampling Patterns

Since the amount of available data often gives strong constraints on the sequence length, the delays τ_i are usually the most important parameters of a symbolic representation. They act as a filter for certain features or timescales, allowing an adjustment of the embedding to the research question under consideration.

Motivated by Takens' theorem (see section 2.2), *equidistant* sampling patterns

$$\tau = (0, \tau_0, \dots, (n-1)\tau_0) \quad (3.24)$$

are used in many cases. For a given sequence length, there is only one parameter τ_0 , which determines a time scale that the sampling pattern is most sensitive to. The applications in chapters 4 and 5 will use equidistant sampling patterns.

Choosing a non-equidistant sampling pattern can possibly influence the width or the form of this 'focus' in terms of time scales. In the following, I present a small excursion to non-equidistant sampling patterns.

A sampling pattern (τ_1, \dots, τ_n) is called sensitive to a *time scale* t , if there exist i and j with $t = \tau_j - \tau_i$. This means that the resulting symbols contain information on pairs of data points that are a time t apart from each other. Then, a natural question is how many different time scales are visible to a sampling pattern, i. e. how broad or narrow the 'focus' on different time scales can be.

Fig. 3.9 gives an example of a sampling pattern $\tau = (0, \tau_1, \tau_2)$, with $\tau_1 \ll \tau_2$, applied to a signal that consists of a slow wave with high frequency modulations. The symbol can access both signals separately by comparing one pair of values in the respective timescale. In other words, the two signals are reflected in the fluctuations of symbol subsets: Low-frequency content causes slow fluctuation between the red and the green symbol class shown in fig. 3.9b. In contrast, high frequency content is represented by quick fluctuations within each of those groups. The symbols drawn in black are rare in a low-frequency signal, hence their relative frequency reflects the power distribution between high and low frequencies.

A Family of Sampling Patterns

A sampling pattern (τ_1, \dots, τ_n) can be described by the differences $\tau_{i+1} - \tau_i$. This defines a *difference vector* $d := (\tau_2 - \tau_1, \dots, \tau_n - \tau_{n-1})$. The time delays that are visible for this sampling pattern are the sums over a subset of subsequent components of d . For example, the sampling pattern $\tau = (0, 1, 3, 6)$ corresponds to the difference vector $(1, 2, 3)$, and can 'see' the delays 3 and 5, but not 4).

Of course, large delays can easily lead to a variety of visible time scales. Therefore, I will ask for sampling patterns, which for fixed sequence length can see all time scales from 1 to some value t , which is to be maximized.

For sequence length n , a delay vector contains $n(n-1)/2$ pairs of values. This is an upper bound for the number of visible time scales. Since all components of d are positive, there are at least $n-1$ different time scales. Reversing a difference vector has no effect on the visible time scales.

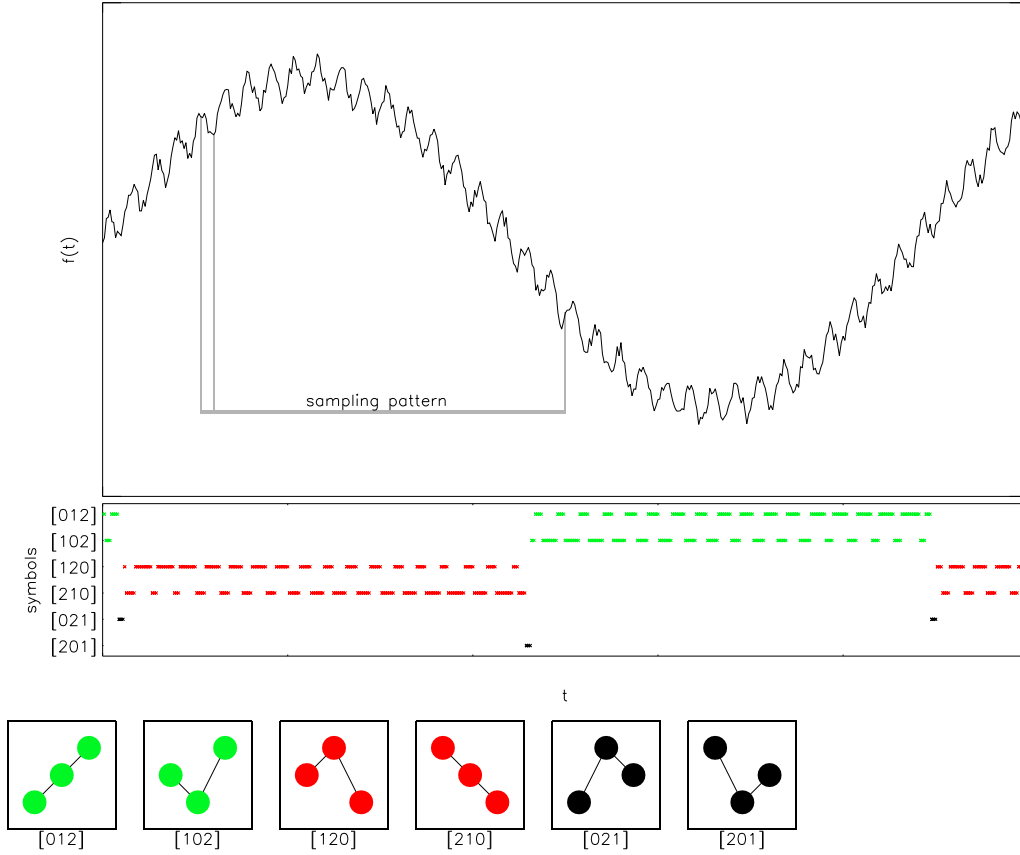


Fig. 3.9: Example for a sampling pattern that is sensitive to two different time scales. Low-frequency content causes slow fluctuations between the red and green symbol classes, while high frequencies are seen as quick fluctuations within each class. The relative frequency of the black class reflects the ratio of high- and low-frequency content.

The lower bound is reached by the uniform difference vector $d = (1, \dots, 1)$, corresponding to the equidistant sampling pattern $\tau = (0, \dots, n - 1)$. For sequence length 4, the upper bound is reached uniquely by the difference vector $(1, 3, 2)$. For sequence length 5 to 8, an examination of all possible combinations shows that the upper bound is not reached by any difference vector. There is no obvious pattern in the optimal difference vectors.

In order to approach the upper bound, I propose a two-parameter family d_{kl} of solutions, with parameters $k, l \in \mathbb{N}$. Start with a prefix of $l - 1$ entries with value 1, covering the numbers below l . Then, add k entries with value l . As an example, the member for $k = 4, l = 5$ is

$$d_{4,5} = (1, 1, 1, 1, 5, 5, 5, 5). \tag{3.25}$$

The sampling pattern that corresponds to d_{kl} has a sequence length $n = k + l - 1$, and its visible time scales extend from 1 to $kl + l - 1$. Fig. 3.10 shows the performance of the family between its upper and lower bound. The lower bound is attained for $k = 0$.

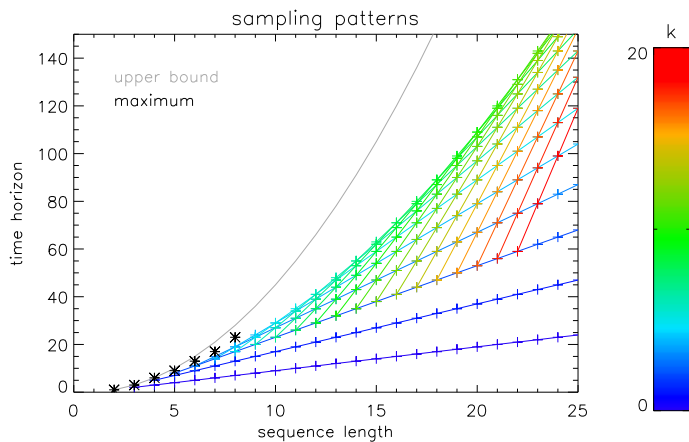


Fig. 3.10: A family of sampling patterns: the colored lines indicate subsets of constant k . The lower bound is realized by $k = 1$, the upper bound is shown in gray. For short sequence length, optimal sampling patterns found via a brute force search are added in black.

3.1.7 Symmetry with Respect to Transformations of the Underlying Time Series

A good description of a time series should not change much under the transformations that are natural for the underlying time series. Therefore, it is useful to study the behavior of symbolic representations under simple transformations of the underlying time series: sign flip and time reversal. Both of these symmetries are characteristic for certain stochastic processes, and are seen in many real world time series, e.g. Brownian motion.

The application of a permutation to a state symbol was defined as left-multiplication (see section 3.1.3). As an abbreviation, define $(-1) \in S_n$ as the 'time-reversing' permutation that turns an ascending delay vector into a descending one. Let x be a delay vector, respectively its state symbol. Let $a \in S_n$ be a rank order, and consider the above transformations of the underlying time series:

- 1) Time Reversal: A rank order a is reversed in time by applying the permutation (-1) to the columns (see fig. 3.6). By eq. 3.10, this corresponds to a right-action of (-1) on a , hence a time reversal multiplies all state symbols with (-1) from the right.
- 2) Sign Flip: A sign flip corresponds to action of (-1) on the rows of a , which is equivalent to a left-action of the inverse $(-1)^{-1} = (-1)$. Consequently, a sign flip of the data multiplies all state symbols with (-1) from the left.

These transformations look simple, but can lead to symbols that differ fundamentally from an algebraic point of view. For example, time reversal turns the transposition $(12) \in S_4$ into the 4-cycle $(14)(23)(12) = (1324)$. The use of algebraic properties calls for symbolic descriptions with invariance properties with respect to those transformations. This might be a reason why most of the previous work with rank orders uses measures like entropy instead of algebraic properties (see [5] [11]).

Now let us consider transfer symbols. As mentioned, state symbols obtain an extra factor (-1) on the left when reversing time, and on the right when flipping the sign. Transfer symbols have the form ab^{-1} . Hence, for the sign flip, both factors appear in the middle, where they cancel each other:

$$a(-1)(b(-1))^{-1} = a(-1)(-1)b^{-1} = ab^{-1}. \quad (3.26)$$

For the time reversal, the factors appear outside of the expression, which results in a conjugation of the transfer symbol with (-1) . This conjugation leaves invariant the cycle structure

but changes the permuted elements (e.g. a transposition (12) becomes $(n, n - 1)$), which leaves invariant most algebraic properties. These invariance properties make transfer symbols a promising construction when considering algebraic properties.

If left-transfer symbols are considered (see section 3.1.3), all factors (-1) act from the other side, hence the effect of time reversal and sign flip is exchanged.

3.2 Derived Measures

Symbolic representations are a filter, extracting certain general characteristics of a data set. To answer a specific question, a corresponding measure must be designed and applied to the symbolic description. The most obvious characteristic of symbol data is its discrete nature. What is also important about the set of symbols is its structure as a finite algebraic group, and the absence of a total order. This section studies measures that are applicable to this sort of data. A focus will be on using the group structure of S_n , which distinguishes a symbolic representation from other discrete sequences.

3.2.1 Class Formation

The most straightforward way is to work directly with the symbol distribution, counting the relative frequency of each symbol. Suppose that one is looking for a certain property in a time series. If this property is correlated with the incidence of certain symbols, the relative frequency of those can be used as an indicator. For instance, in the case of two time series, the relative frequency of the identity transfer symbol is a simple indicator of similarity or synchronization.

However, there are several disadvantages of performing statistics over the full set of symbols. Dependent on the chosen sequence length, the set of symbols is large. In the presence of noise, a reliable estimation of relative frequencies needs large sample sizes. Furthermore, there are permutations that are often strongly correlated, like the various transpositions.

In many situations, similar symbols can be grouped together to *symbol classes*, without losing essential information. This means considering a partition of S_n into disjunct subsets, usually constructed as classes of an equivalence relation. Instead of working with the full set of symbols, each element is mapped to its equivalence class.

Symmetries of the system can be a further reason to use symbol classes. One usually does not want that a description changes under a transformation that leaves the system invariant. Transfer symbols for example are not symmetric with respect to an exchange of source and target, which often breaks a symmetry of the system under consideration. This can be resolved by grouping each element with its inverse or, more generally, by choosing a partition of S_n that is invariant with respect to inversion.

Conjugacy Classes

When working with permutations, it is often assumed that a permutation acts on elements that are treated as a set without any structure. In this setting, the action of exchanging two elements A and B has the same properties as the action of exchanging any other two elements C and D . This symmetry corresponds to an invariance with respect to exchanging all references to one object with references to another, for instance: '*replace every A with a B when describing a permutation*'. The following definition states this in a formal way:

Definition 3.7. Let $a, b \in S_n$. The permutation $b^{-1}ab$ is called 'a **conjugated** by b '. This makes conjugation an operation of S_n on itself. The equivalence class

$$[a] := \{b^{-1}ab | b \in S_n\} \quad (3.27)$$

of a permutation modulo conjugation is called its **conjugacy class**.

Obviously, being conjugated is an equivalence relation between permutations. Thus, the permutation group splits as a disjoint union of equivalence classes. Conjugation is transitive on the set of k -cycles for fixed k , which means that it can transform any k -cycle into any other. Since each permutation has a unique (up to sequential rearrangement) description as a composition of disjoint cycles, this implies that the conjugacy class of a permutation is determined by its partition into cycles. Hence, for permutations of n elements, the set of conjugacy classes is the set of partitions of n .

This assumption of an unordered set is not always appropriate. One can think of permuting objects of different weight (heavier ones being harder to move), or of objects arranged in a row (neighbors being easier to exchange). In situations like these, the symbolic description can not be expected to be conjugation-invariant.

Algebraic Order

The *algebraic order* of a group element is defined as

$$\text{ord}(x) := \inf\{n \in \mathbb{N} | x^n = e\}, \quad (3.28)$$

where e is the neutral element of the group. It is straightforward to see, that all elements of a finite group have finite order. Monetti et al. [65] found that the distribution of the algebraic order of transfer symbols can distinguish different synchronization regimes of a coupled system.

In practice, the algebraic order has some nice properties. For the commonly used sequence lengths 4, 5, 6, there is a convenient number of classes (4, 6, and 6, respectively). Therefore, the possible order distributions span a space of 3 – 5 dimensions, which is low enough to be accessed with reasonable sample sizes, and can still be visualized to some extent.

3.2.2 Distance Measures on S_n

Apart from measuring the relative frequencies of the symbols that are characteristic for certain features, comparing symbols or symbol sequences one-to-one is a straightforward approach for measuring similarities. Therefore – without claiming completeness – this section will summarize a collection of distance measures on the symmetric group S_n that are found in the literature. Note that some of the measures come from the context of the comparison of lists, and different measures might be similar when considered for small n . Before presenting the measures themselves, important properties of a distance measure are given.

Definition 3.8 (Bi-invariance). A metric d on S_n is called **bi-invariant**, if it is invariant under elements of the group acting from both sides:

$$d(ca, cb) = d(a, b) = d(ac, bc) \quad \forall a, b, c \in S_n. \quad (3.29)$$

The first equation (*left invariance*) turns out to be equivalent to the statement that d is a function of the transfer symbol. To see this, consider two pairs of state symbols that lead to the same transfer symbol:

$$\begin{aligned} a^{-1}b &= A^{-1}B \\ \Leftrightarrow Aa^{-1} &= Bb^{-1} \\ \Leftrightarrow \exists c \in S_n : A &= ca, B = cb. \end{aligned} \tag{3.30}$$

This shows, that two pairs of symbols lead to the same transfer symbol if and only if they differ by the action of a group element c from the left. A similar calculation shows that the second equation of definition 3.8 (*right-invariance*) implies that the distance is a function of the left-transfer symbol (as defined in section 3.1.3).

For a bi-invariant distance measure, both equations are fulfilled. As shown, left-invariance implies that the distance is determined by the transfer symbol. The right-action conjugates the transfer symbol,

$$(ac)^{-1}bc = c^{-1}a^{-1}bc. \tag{3.31}$$

Therefore, a bi-invariant distance measure of S_n is a conjugation-invariant function of the transfer symbol. Since the number of conjugacy classes is small, there is not much freedom left, i. e. bi-invariance is a strong restriction for a distance measure.

When considering arrangements of n items on n positions, the right-action corresponds to a re-labeling of the positions, while the left-action can be described as a re-labeling of the permuted items (compare fig. 3.3 for the use of the terms *positions* and *items*). If a right-invariant measure is applied to the inverse of its argument, one gets a dual measure that is left-invariant and vice versa:

$$\begin{aligned} d : xy &\mapsto d(x, y) && \text{is left-invariant} \\ \Leftrightarrow d' : xy &\mapsto d(x^{-1}, y^{-1}) && \text{is right-invariant} \end{aligned} \tag{3.32}$$

Since inverse elements share the same conjugacy class, bi-invariant measures are their own dual.

I should also mention the notion of an *edit distance*, which comes from the context of string operations in computer science. Suppose that there is a set of admissible edit actions, like inserting or deleting single characters. An edit distance between two strings counts the minimum number of edit steps needed to transform one string into the other. I will only use term '*edit distance*', if the edit steps do not only exist, but also have a reasonable meaning as edit actions.

A Compilation of Some Distance Measures

1. The above-mentioned *algebraic order* of a transfer symbol is a bi-invariant distance measure between two symbols. For $n \geq 5$, it is not sub-additive⁴, i. e. the triangle inequality fails. Still, the algebraic order of the transfer symbol can be interpreted as a distance measure between symbols.

⁴for example, with $a := [01234]$, $b := [01243]$, $c := [12043]$, we have $d(a, b) = 2$, $d(b, c) = 3$ and $d(a, c) = 6$, violating the triangle inequality.

2. The *minimum number of transpositions* needed to generate a transfer symbol is another conjugation-invariant function, hence bi-invariant. This measure is the path metric of a graph, where two permutations are connected if they differ by a transposition acting from the right. This makes it an edit distance, thus a metric. Note that right- and left-transfer symbols share their conjugacy class, hence they lead to the same metric.
3. The *exact match distance* counts the number of positions, on which two permutations do not agree. It is another example of a bi-invariant metric. This measure equals n minus the *hamming distance*, if the rank orders are treated as strings (or n minus the number of fixed points of the transfer symbol).
4. The *Kendall tau* [47] or *bubble-sort distance* counts the pairs of positions, about whose order two symbols disagree, i. e. for positions i, j , one symbol gives the higher rank to i and the other to j . Conversely, the dual measure counts the pairs of items, about whose order two symbols disagree. These are edit distances, for the exchange of neighboring positions or items, respectively, and therefore is equal to the running time of a bubble-sort algorithm. Note that the graph of the Kendall tau distance is the dual graph⁵ to the polytope presented in section 3.1.4. As an example, consider the rank orders [1342] and [1243]. They disagree on one pair of positions (2/4), therefore the Kendall tau distance is 1. They disagree on the order of three pairs of items (2/3, 3/4, and 2/4), hence the dual distance is 3.
5. *Spearman's footrule* [96] sums up the distance between the positions of each item in two rank orders⁶. In terms of the transfer symbol, this is the distance that each item is moved. Since this definition uses the distance between positions, it is not right-invariant. The dual measure considers the change of rank in each position, thus it is the *Manhattan distance* between the rank orders in one-line notation. Counterparts to the *Euclidean* or l^∞ metric can be generated by summing up some function of the above distances. The triangle inequality holds as long as this function is monotonically increasing.
6. The *adjacency distance* counts the number of times that $a(k+1)$ does not immediately follow $a(k)$ in b . This uses neighboring positions, hence is not right-invariant.
7. The length of the *longest common subsequence* is a similarity measure, it is subtracted from its maximum n to obtain a metric, ranging from 0 to $n-1$. Note that, in contrast to a substring, a subsequence of a rank order does not have to be consecutive. Since the metric uses relative positions, it is not right invariant. This is an edit distance, with insertion and deletion as edit steps. When keeping the length of a rank order constant, the basic edit step is one deletion and one insertion, which is described by the action of a contiguous cycle $(k, \dots, k+l)$ on the positions of a given rank order. Accordingly, the edit steps of the dual metric act on the element labels.

I compared the different distance measures by their mutual information over all pairs of symbols. Surprisingly, the dual pairs tend to have low mutual information, meaning that they

⁵The vertices of the dual graph are the faces of the polytope. Two vertices are connected if the corresponding faces share an edge.

⁶The term is in use both for the distance measure between rank orders and for the derived correlation coefficient.

Information content of metrics [bits]			
n	4	5	6
upper bound ($2 \log_2(n!)$)	9.17	13.81	18.98
bound for symm. ($\log_2(\frac{n!(n!-1)}{2})$)	8.11	12.80	17.98
all considered metrics	4.54	6.85	9.18
bi-invariant bound ($\log_2(\#c)$)	2.32	2.81	3.46

Table 3.1: Information content of a distance function on S_n (in the sense of information entropy, supposing a uniform symbol distribution). The weakest bound is the information that is needed to discern every pair of symbols (first row). Symmetric functions can not distinguish between a pair a, b and the converse b, a , which lowers the bound by about 1 bit (second row). The third row shows the combined information of all presented distances. The fourth row shows the information that the conjugacy class of the transfer symbol contains ($\#c$ refers to the number of conjugacy classes in S_n). This forms an upper bound for the information of a bi-invariant distance.

are not similar but complementary. The set of left- and right-invariant metrics respectively have much in common.

Table 3.1 compares the information content of distance measures for different sequence lengths. The upper bound of $2 \log_2(n!)$ bits marks the maximum information that a function of two symbols can contain. If assuming symmetry, the bound is reduced by about 1 bit. For comparison, the joint information entropy of the distance measures presented above is calculated. As mentioned, the partition (or equivalently the conjugacy class) of the transfer symbol contains all information a bi-invariant metric can contain. Since bi-invariance implies a high degree of symmetry, such measures contain less information.

3.2.3 The Kullback-Leibler Distance

Symmetry

The Kullback-Leibler distance [51] was introduced in section 2.3.3 as a natural distance measure between probability distributions. Since the asymmetric construction with a sample and a reference distribution is not always appropriate, let us take a look at an approach to symmetrize the distance (see [104]):

$$\begin{aligned}
 d(a, b) &:= d_{\text{KL}} \left(a, \frac{a+b}{2} \right) + d_{\text{KL}} \left(b, \frac{a+b}{2} \right) \\
 &= \sum_i a_i \log_2 \left(\frac{2a_i}{a_i + b_i} \right) + b_i \log_2 \left(\frac{2b_i}{a_i + b_i} \right).
 \end{aligned} \tag{3.33}$$

As mentioned, the Kullback-Leibler distance measures the number of wasted bits, for a message of distribution a , which is transmitted using a code optimized for the distribution b . The symmetric distance d measures the number of wasted bits, if both a and b are transmitted using a common code optimized for $\frac{a+b}{2}$.

Since the support of $\frac{a+b}{2}$ always contains the support of a and the one of b , the distance d is defined for any a and b . The separation property of a metric,

$$d(a, b) = 0 \Leftrightarrow a = b, \tag{3.34}$$

is fulfilled because it is valid for d_{KL} . The symmetry axiom

$$d(a, b) = d(b, a) \quad (3.35)$$

holds by construction. Only the triangle inequality

$$d(a, c) \leq d(a, b) + d(b, c) \quad \forall a, b, c \quad (3.36)$$

fails. This comes from the fact that it fails for the Kullback-Leibler distance.

Triangle Inequality

A fundamental property that distinguishes the Kullback-Leibler distance from a metric is that it does not grow fast enough in the infinitesimal limit. More precisely, the linear coefficient vanishes:

$$\lim_{\epsilon \searrow 0} \frac{d}{d\epsilon} d_{\text{KL}}(x, (1 - \epsilon)x + \epsilon y) = 0, \quad (3.37)$$

for any other element y of the corresponding distribution space. If the second derivative does not vanish (provided a well-behaved function, for instance piecewise monotonic) every x has a neighborhood, where d is *convex* as a function of y , and the following proposition applies.

Remark 3.9. *Let $d : (x, y) \mapsto d(x, y)$ be a distance function on an interval. If d is strongly convex as a function of y , then it is not a metric.*

Proof. Let d be a metric on an interval $[a, b]$. Suppose that d is convex as a function of y . Consider the middle of the interval, $c := \frac{1}{2}(a + b)$. By symmetry of d , we have

$$d(a, b) = d(b, a). \quad (3.38)$$

Concavity at a implies that

$$\frac{1}{2}d(a, b) > d(a, c). \quad (3.39)$$

By concavity at b and symmetry, we have

$$\frac{1}{2}d(a, b) > d(c, b). \quad (3.40)$$

It follows that

$$d(a, b) > d(a, c) + d(c, b), \quad (3.41)$$

which means that d does not respect a triangle inequality, in contradiction to the preconditions. \square

Remark 3.9 essentially says that, in the case of the Kullback-Leibler distance, the metric properties already fail at the lowest scale: within a 1-dimensional infinitesimal neighborhood. Fig. 3.11a illustrates the failure of the triangle inequality for a random sample of distributions. Fig. 3.11b evaluates a one-dimensional example, with distributions $a := (0.25, 0.75)$, $b := (p, 1 - p)$, and $c := (0.5, 0.5)$. The triangle inequality demands $d(a, b) + d(b, c)$ (red) to be minimal at $p = 0.25$, and $p = 0.5$, which fails here.

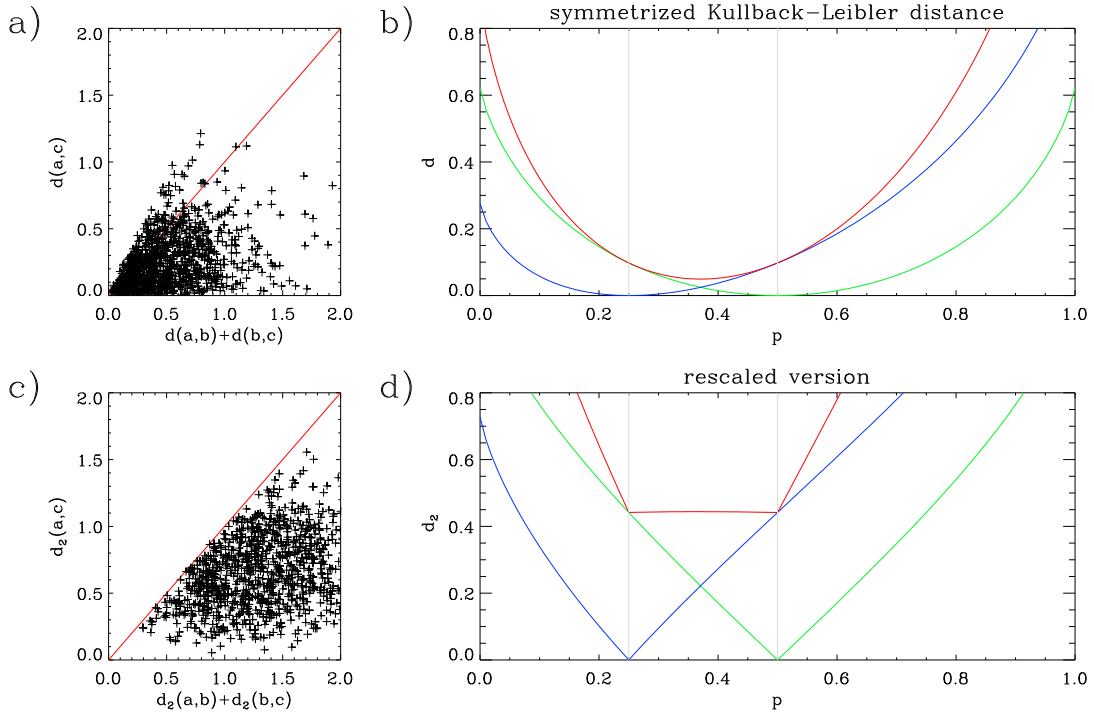


Fig. 3.11: a) values of d for a random set of distributions in 5 dimensions. b) $d(a, b)$ (blue), $d(b, c)$ (green) and the sum (red), for distributions $a := (0.25, 0.75)$, $b := (p, 1 - p)$ and $c := (0.5, 0.5)$. The triangle inequality demands that the sum (red) has minima at $p = 0.25$ and $p = 0.5$. c), d) the corresponding graphs for the rescaled distance d_2 from eq. 3.42. The numerical example shows no violation of the triangle inequality.

Remark 3.9 suggests that the triangle inequality can possibly be fixed by a nonlinear *rescaling* of the Kullback-Leibler distance. A square root ansatz,

$$d_2(a, b) := \sqrt{d_{\text{KL}}\left(a, \frac{a+b}{2}\right)} + \sqrt{d_{\text{KL}}\left(b, \frac{a+b}{2}\right)}, \quad (3.42)$$

leads to a positive linear coefficient in the infinitesimal limit (this can be checked by a straightforward calculation).

The separation and symmetry properties of d are not changed by this rescaling. Fig. 3.11c and d show no violation of the triangle inequality, such that d_2 possibly fulfills all the axioms of a metric. To prove this, one would need to show the following:

$$d_2(a, c) \stackrel{?}{\leq} d_2(a, b) + d_2(b, c) \\ \forall a, b, c \in [0, 1]^n \mid \sum_i a_i = \sum_i b_i = \sum_i c_i = 1 \quad (3.43)$$

$$\begin{aligned}
&\Leftrightarrow \sqrt{\sum_i a_i \log_2 \left(\frac{2c_i}{a_i + c_i} \right)} + \sqrt{\sum_i c_i \log_2 \left(\frac{2a_i}{a_i + c_i} \right)} \\
&\leq^? \sqrt{\sum_i a_i \log_2 \left(\frac{2b_i}{a_i + b_i} \right)} + \sqrt{\sum_i b_i \log_2 \left(\frac{2a_i}{a_i + b_i} \right)} \\
&\quad + \sqrt{\sum_i b_i \log_2 \left(\frac{2c_i}{b_i + c_i} \right)} + \sqrt{\sum_i c_i \log_2 \left(\frac{2b_i}{b_i + c_i} \right)}.
\end{aligned} \tag{3.44}$$

Apart from proving the metric properties, one has to ask how useful the resulting measure is. The symmetrization and rescaling are probably the least possible modifications to the Kullback-Leibler distance that allow to fulfill the axioms of a metric. However, they remove essential characteristics of the Kullback-Leibler distance, like the unboundedness in the context of 'nearly-forbidden' events, or the vanishing differential in the infinitesimal limit. Therefore, it is probably not a natural measure for distributions any more. Supposing a finite sample space, both symmetrized distances d and d_2 are highly correlated (correlation coefficient $c \approx 0.95$) to the euclidean metric. I conclude that the usefulness of such a measure is limited because in most cases it is probably preferable to either live with the non-metric Kullback-Leibler distance or use a more straightforward metric like the euclidean one.

3.2.4 Distance to Independence

Statistical dependence is one way to describe similarities between the components of a coupled system. In an analogy to *mutual information*, I discuss an approach of Monetti et al. [65], where an independent version of the time series is artificially created, and compared to the original data.

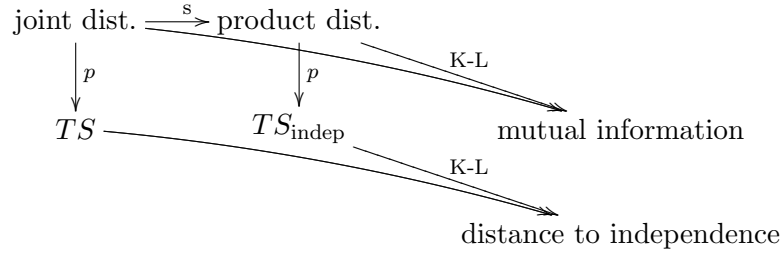
In this case, the original data consists of two time series. The first step is to make the two components independent. Shuffling the underlying time series would result in a uniform state symbol distribution, and therefore remove all of the information contained. For this reason, the sequences are shuffled at the level of state symbols. This corresponds to considering the product of the marginal symbol distributions.

The most straightforward way of comparing is the Kullback-Leibler distance between the joint distribution and the artificial product distribution. The result is called the *mutual information* of the two sequences (see for instance Cover and Thomas [24]).

Instead of distributions of symbol pairs, one can compare the corresponding transfer symbol distributions. I will refer to this as the *distance to independence* of two symbol sequences (or of their underlying time series). Let

$$p : (a, b) \mapsto a^{-1}b \tag{3.45}$$

be the mapping of a pair of symbols to their transfer symbol. This induces a (linear) projection of the space of distributions on $S_n \times S_n$ to the space of distributions on S_n , reducing the dimensionality from $n!^2 - 1$ to $n! - 1$. The only difference between mutual information and the distance to independence of transfer symbols is this projection step, before calculating the Kullback-Leibler distance. The following diagram illustrates the relation, where s is the above mentioned shuffling of the sequences, which generates the product distribution, and p is the projection from pairs of state symbols to transfer symbols:



Compared to the mutual information, the main advantage of the distance to independence is that it does not require an estimation of the joint distribution of the two symbol sequences. It is therefore possible to obtain significant results with smaller sample sizes (the joint distribution has $n!^2$ degrees of freedom, while the transfer symbol distribution has $n!$).

The following remark will show that the projection from state symbols to transfer symbols does not increase distances, which implies that the mutual information is an upper bound for the distance to independence:

Remark 3.10. *Merging elements in a probability space does not increase Kullback-Leibler distances.*

Proof. The Kullback-Leibler distance is defined as

$$d_{\text{KL}}(p, q) = \sum_{x \in X} p(x) \log_2 \left(\frac{p(x)}{q(x)} \right), \quad (3.46)$$

where p and q are probability distributions over a discrete set X . Let a and b be two disjunct events, which are to be merged. The corresponding terms of eq. 3.46 before and after merging are

$$p(a) \log_2 \left(\frac{p(a)}{q(a)} \right) + p(b) \log_2 \left(\frac{p(b)}{q(b)} \right) \quad \text{and} \quad (p(a) + p(b)) \log_2 \left(\frac{p(a) + p(b)}{q(a) + q(b)} \right), \quad (3.47)$$

with $0 \leq p(a), p(b), q(a), q(b) \leq 1$. Then, the following estimates apply:

$$\log_2 \left(\frac{p(a) + p(b)}{q(a) + q(b)} \right) \leq \log_2 \left(\frac{p(a) + p(b)}{q(a)} \right), \quad \log_2 \left(\frac{p(a) + p(b)}{q(b)} \right), \quad (3.48)$$

which lead to

$$\begin{aligned} (p(a) + p(b)) \log_2 \left(\frac{p(a) + p(b)}{q(a) + q(b)} \right) &\leq p(a) \log_2 \left(\frac{p(a) + p(b)}{q(a)} \right) \\ &\quad + p(b) \log_2 \left(\frac{p(a) + p(b)}{q(b)} \right) \\ &\leq p(a) \log_2 \left(\frac{p(a)}{q(a)} \right) + p(b) \log_2 \left(\frac{p(b)}{q(b)} \right). \end{aligned} \quad (3.49)$$

□

In order to give an idea of the difference between the two measures, the following example shows a change in two symbol sequences, which is detected by mutual information but leaves the distance to independence invariant:

Example 3.11. *It is possible to change the joint distribution of two symbol sequences without changing the transfer symbols or the marginal distributions. One starts with a product distribution and asks for a change that leaves the transfer symbol distribution invariant. The idea is the following: choose suitable pairwise different symbols a, b, c, d and change the joint distribution in the following way (each $+/-$ means a change in probability by the same amount):*

	a	b	c	d
a	$+$	$-$	$.$	$.$
b	$-$	$+$	$.$	$.$
c	$.$	$.$	$-$	$+$
d	$.$	$.$	$+$	$-$

The question is, if there exists an appropriate choice for a, b, c, d . The elements on the diagonal are mapped to the identity transfer symbol, thus their contributions cancel out. Set

$$ab^{-1} = cd^{-1}, \quad (3.50)$$

then the contributions above the diagonal go to the same transfer symbol and cancel out. For the ones below, one needs $ba^{-1} = dc^{-1}$, which is equivalent to eq. 3.50. Setting $a := 1$ and $b := cd$, one needs $c, d \neq 1$, with $c \neq d$ and $cd \neq 1$. These exist for sequence length $n \geq 3$.

3.3 Change of Sequence Length, and Entropy Rate

Another reason to study the transition between different sequence lengths is the information content of a symbolic representation. The following sections deal with the conditional distributions of a symbol given its predecessor(s). It is often too complex to consider the whole past of a symbol. As an approximation, one can study what the knowledge of one symbol in the sequence implies about its successor. To do this, I modeled the transition from one symbol to the next as an expansion following a truncation of the corresponding delay vector(s). In section 3.3.5, this is used to derive estimations of the entropy rate of symbol sequences.

The sequence length of a symbolic representation determines the number of possible order patterns. With increasing sequence length, the set of symbols gets larger and a symbolic representation potentially captures more information per time step. Therefore the sequence length can be considered as a parameter for the level of detail. From the perspective of rank orders, adding or removing points in the delay vector is a natural morphism, connecting rank orders of different sequence length. This section aims to describe this transformation in algebraic terms.

A first straightforward question is, if an increase of the sequence length corresponds to a refinement of a symbolic measure or leads to a completely different one. Consider a single delay vector used to define one state symbol. On the level of rank orderings, the order of a set contains all information about the order of any subset. It follows that a series of state symbols determines all state symbols with lower sequence length. In this sense, a raised sequence length leads to a refinement of the representation. Section 3.3.1 will show that this is not the case for transfer symbols, i. e. a long transfer symbol does not always determine a shorter one.

I propose a convention that allows to include symbols of different sequence length in equations. In terms of permutations, a permutation of $n - 1$ elements can be considered as a permutation of n elements, which fixes the last one. Formally, this defines a canonical embedding of the group S_{n-1} into S_n . In terms of rank orders, this corresponds to the expansion of

a delay vector by one point, which (by convention) is given the highest rank (see fig. 3.12a and b). To facilitate the readability and avoid misunderstandings, small letters stand for symbols of short sequence length $n - 1$ and capital letters for sequence length n . Note that formally, all equations refer to the group structure of S_n .

3.3.1 Expansion

Let us begin by describing the expansion of a delay vector by an additional data point. Let s be the corresponding state symbol of sequence length $n - 1$, and suppose that the new data point has rank k . To obtain the symbol of the expanded delay vector, starting from the canonical embedding of s , the highest row is moved from rank n to rank k , raising the ranks from k to $n - 1$ by one (as an example, fig. 3.12 shows $k = 3$). This corresponds to the action of the cycle

$$\varphi_k := (k, \dots, n) \quad (3.51)$$

from the left. Thus, the expanded delay vector is described by the state symbol

$$S = \varphi_k s. \quad (3.52)$$

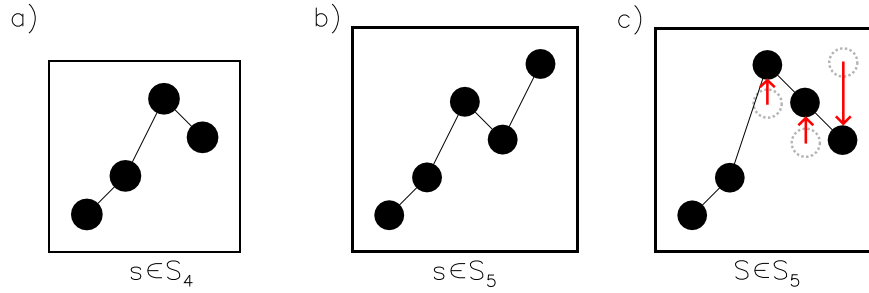


Fig. 3.12: Expansion of a state symbol. a) short symbol $s \in S_4$ b) canonical embedding of s into S_5 c) an expansion of $s \in S_4$ with an additional point of rank 3 corresponds to the action of φ_3 on the canonical embedding from the left (indicated by the red arrows).

Since the embedding can be done iteratively, an expansion from length n to $n + m$ is described by a composition of several cycles,

$$(k_m, \dots, n + m) \dots (k_1, \dots, n + 1) \quad (3.53)$$

acting from the left, where k_i is the rank of the i -th additional point within the first $n + i$ points. Note that the definition of φ_k implicitly contains the sequence length, which in this case changes in each iteration. Formally, all terms of eq. 3.53 are considered as elements of S_{n+m} .

As a next step, eq. 3.52 is used to describe the expansion of a transfer symbol. In terms of the information content of a symbolic representation, the question here is what amount of additional information is added by an extra point of data. Let $s_1, s_2 \in S_{n-1}$ be state symbols, which are expanded by data points with rank k_1 and k_2 , respectively. The resulting expanded transfer symbol is

$$\begin{aligned} T &= S_1^{-1} S_2 \\ &= s_1^{-1} \varphi_{k_1}^{-1} \varphi_{k_2} s_2. \end{aligned} \quad (3.54)$$

In the context of the information content of a symbolic representation, one would like to write this as a function of the short transfer symbol $t = s_1^{-1}s_2 \in S_{n-1}$. The pairs of state symbols that correspond to t can be expressed as

$$\{(q, qt) | q \in S_{n-1}\}. \quad (3.55)$$

Thus, the set of possible expanded transfer symbols is

$$T = q^{-1}\varphi_{k_1}^{-1}\varphi_{k_2}qt \quad \text{for } q \in S_{n-1}, k_1, k_2 \in \{1, \dots, n\}. \quad (3.56)$$

In order to describe this set, first consider the middle part:

$$\varphi_{k_1}^{-1}\varphi_{k_2} = (n, \dots, k_1)(k_2, \dots, n) = \begin{cases} (n, k_2, \dots, k_1 - 1) & \text{for } k_1 > k_2 \\ (n, k_2 - 1, \dots, k_1) & \text{for } k_1 < k_2 \\ Id & \text{for } k_1 = k_2 \end{cases} \quad (3.57)$$

This is the set of possible expansions for $t = id$ and $q = id$. Following eq. 3.51, the left-action of the permutation $\varphi_k^{-1}\varphi_l$ first lowers the highest point to rank l , and then raises the point of rank k to the highest rank. Eq. 3.57 describes the dependence of the expanded transfer symbol on the ranks k_1, k_2 of the additional points.

Note that the multiplication with t in eq. 3.56 is a bijection of S_n , hence it shuffles the symbols, preserving multiplicities. For the moment, assume $t = id$ and focus on the conjugation with q . Since $q \in S_{n-1}$, the conjugation is only done with permutations that have a fixed point at the end. The equivalence classes of this operation are the conjugacy classes of S_n , refined by the additional information in which sort of cycle the last point is located. The classes that occur are (note that $\varphi_{k_1}^{-1}\varphi_{k_2}$ can not result in more than one cycle)

- $k_1 = k_2$ results in the identity, which occurs in $\#(C) = n$ cases. The identity forms a class of its own, with cardinality $|C| = 1$.
- A k -cycle including the last point (with $k \in \{2, \dots, n\}$). For each k , this sort of cycle occurs for the parameters $k_1 - k_2 = \pm k - 1$. This leads to

$$\#(C) = 2(n - k + 1) \quad (3.58)$$

occurrences. The cardinality of the classes is

$$|C| = (n - 1)! / (n - k)!. \quad (3.59)$$

The conjugation action generates from each point a uniform distribution over its class. Thus, after conjugation, the frequency of each permutation of a class C is

$$\#(C) \frac{|S_{n-1}|}{|C|}. \quad (3.60)$$

This completely describes the expansion behavior of $t = id \in S_{n-1}$. Since t is applied after the conjugation action, different values of t lead to a permutation of the same relative frequencies.

Coming back to the information theoretic context, for a given t there generally are more than n possible values for T . This implies that, given T , t is generally not unique. Thus, expanding the delay vector does not only introduce new information, but also destroys some of the existing information.

3.3.2 Truncation

In terms of rank orders, the truncation of a delay vector is much simpler than an expansion, because no additional information is introduced. The truncation is a projection from the group S_n to S_{n-1} . Reversing eq. 3.52 leads to

$$\begin{aligned} s &= \varphi_k^{-1} S \\ &= \varphi_{S(n)}^{-1} S. \end{aligned} \quad (3.61)$$

Note that 3.61 explicitly contains $S(n)$, which comes from the fact that truncating is a non-invertible transformation. It would be convenient to have an expression without this dependence.

To describe the truncation of a transfer symbol, reverse eq. 3.56:

$$t = q^{-1} \varphi_{k_2}^{-1} \varphi_{k_1} q T. \quad (3.62)$$

In this equation, the right hand side always exists, but it is only a valid solution for t if it is an element of S_{n-1} , i. e. if it fixes the point n . It is useful to distinguish between two cases:

1. Suppose that T fixes n . Then, the rest of the right hand side must also fix n . Conjugation with $q \in S_{n-1}$ does not change this property, hence $\varphi_{k_2}^{-1} \varphi_{k_1}$ also fixes n , and eq. 3.57 gives $k_1 = k_2$. Thus, $\varphi_{k_2}^{-1} \varphi_{k_1} = id$. This is independent of the value of k_1 and k_2 , therefore the truncated transfer symbol t is unique for any T that fixes n .
2. Any other T maps n to $T(n)$, thus the term $q^{-1} \varphi_{k_2}^{-1} \varphi_{k_1} q$ must map $T(n)$ to n . Hence, one needs k_1, k_2 such that $\varphi_{k_2}^{-1} \varphi_{k_1}$ maps $(qT)(n) =: x$ to n . Eq. 3.57 leads to $(k_1, k_2) = (x, i)$, with $i = x + 1, \dots, n$, and $(x + 1, i)$, with $i = 0, \dots, x$. Consequently, if T does not fix n , then for a given q there are n possibilities for t .

For compatibility with the symbolic formalism from section 3.1.3, one would like to write the truncation as an operator, i. e. an object that can act both from left and right and follows an associative law. Unfortunately, this is not possible, as the following counterexample illustrates: suppose there exists an operator A , whose left action is the truncation:

$$[2314]A = [231] = [2413]A. \quad (3.63)$$

Multiplication with $[3421]$ from the right leads to

$$[2314]A[3421] = [2413]A[3421]. \quad (3.64)$$

If $a[3421]$ is a well-defined symbol, this leads to $[2314] = [2413]$, which is a contradiction. This shows, that $A[3421]$ can not be a well defined symbol. Hence, there exists no corresponding right-action for A . Consequently, A can not be written as an operator.

3.3.3 Conjugacy Classes under Change of Sequence Length

As a characteristic for the the algebraic properties, I will consider conjugacy classes. Table 3.2a shows what happens to state symbols of the same conjugacy class in a truncation. In the table, the conjugacy classes are sorted first by number of moved elements, then by longest cycle.

There is some 'diagonal-like' structure, where most symbols retain similarities to their image. Furthermore, the table shows sporadic forbidden transitions. However, the behavior of the conjugacy classes is far from hierarchical, i. e. the conjugacy class of the long symbol does not determine that of the short one.

As seen in section 3.2.2, the conjugacy class contains 3.0 and 2.6 bits of information, for sequence length 6 and 5 respectively. However, only 0.26 bits of this are mutual information (with respect to the truncation). The above total order on the set of conjugacy classes allows the definition of a correlation coefficient between the class of long and of short symbols, which is 0.36 between the considered sequence lengths 5 and 6. In conclusion, a change of sequence length is straightforward on the level of order patterns, but algebraic properties can change considerably.

Now I ask the same question in the context of transfer symbols. I consider all possible pairs of state symbols that can lead to a certain transfer symbol of length n . The last time step (on the level of the pair of rank orderings) is cut off, and the resulting transfer symbol of length $n - 1$ is recorded. Table 3.2b shows the resulting conjugacy class distribution.

Tables 3.2a and b are surprisingly similar. However the latter has a more distinguished diagonal structure, reflected in a correlation coefficient of 0.51 (compared to 0.36 for the first). It is not clear why table 3.2b only contains multiples of $1/3$, i. e. the entries appear in groups of 240.

3.3.4 Transition between Overlapping Symbols

The reasoning of the preceding sections allows to describe the transition from one symbol within a symbolic representation to the next one in the sequence. Like the expansion and truncation, this is a simple and natural transformation in terms of rank orders, but it is not obvious at all how it affects algebraic properties. Let (S_i) be the symbolic representation of a time series (as in definition 3.2), with an equidistant sampling pattern.

Starting from a state symbol S_i , an expression is needed for the following state symbol in the series, S_{i+1} . S_i is truncated by cutting off the first point. Formally, the point is first transported to the last position by the action of $(1, \dots, n)$ from the right, i. e. by permuting columns. Afterwards, the last point, which now has rank $S(1)$, is removed by the action of $\varphi_{S(1)}^{-1}$ from the left (see eq. 3.61). Hence, the short state symbol is

$$s_i = \varphi_{S(1)}^{-1} S_i(1, \dots, n). \quad (3.65)$$

Then, the short symbol s_i is expanded by the action of φ_k from the left:

$$S_{i+1} = \varphi_k \varphi_{S(1)}^{-1} S(1, \dots, n), \quad (3.66)$$

where k is the rank of the next data point in the corresponding time series. Note that the rank is considered within the set of the last n data points.

Eq. 3.66 can be used to describe the transition between subsequent transfer symbols T_i . Let S_i and S'_i be the state symbols of two time series, and k and k' the ranks of the next data

a) state symbols

	conjugacy class of S_i										
	(-)	(2)	(3)	(2+2)	(4)	(3+2)	(5)	(2+2+2)	(3+3)	(4+2)	(6)
conjugacy class of s_i	(-)	(2)	(3)	(2+2)	(4)	(3+2)	(5)	(2+2+2)	(3+3)	(4+2)	(6)
(-)	1	1	1	0	1	0	1	0	0	0	1
(2)	0	11	6	7	9	6	10	0	2	5	4
(3)	0	1	25	5	20	22	19	1	5	6	16
(2+2)	0	0	1	19	7	22	13	5	2	10	11
(4)	0	1	4	7	41	22	46	2	10	23	24
(3+2)	0	0	2	4	4	32	16	4	12	26	20
(5)	0	1	1	3	8	16	39	3	9	20	44

b) transfer symbols

	conjugacy class of T_i										
	(-)	(2)	(3)	(2+2)	(4)	(3+2)	(5)	(2+2+2)	(3+3)	(4+2)	(6)
conjugacy class of t_i	(-)	(2)	(3)	(2+2)	(4)	(3+2)	(5)	(2+2+2)	(3+3)	(4+2)	(6)
(-)	1.0	1.67	1.33	0.00	1.00	0.00	0.67	0.00	0.00	0.00	0.33
(2)	0.0	11.33	8.67	11.00	10.00	6.00	7.33	0.00	0.67	2.33	2.67
(3)	0.0	1.00	25.33	5.33	26.00	23.33	20.67	0.33	4.67	4.00	9.33
(2+2)	0.0	0.00	0.67	19.67	5.00	26.00	12.67	6.33	1.33	10.67	7.67
(4)	0.0	0.67	2.67	5.00	41.33	22.67	54.00	1.33	7.33	21.00	24.00
(3+2)	0.0	0.00	0.67	2.00	2.67	31.33	10.67	4.67	16.00	30.67	21.33
(5)	0.0	0.33	0.67	2.00	4.00	10.67	38.00	2.33	10.00	21.33	54.67

Table 3.2: Conjugacy classes (sequence length 5 versus 6). The tables show the numbers of possibilities that a short symbol of one conjugacy class (rows) is mapped to a long symbol of another class (columns). The classes are noted by their composition into cycles, for instance (3 + 2) means a two-cycle and a three-cycle, and (-) means the identity (i. e. no cycle at all). a) State symbols, there are $6! = 720$ possibilities. b) Transfer symbols, there are $n!^2$ possibilities, the numbers are rescaled to a sum of 720, so that they can be compared to part a) and the sum over a column is again the cardinality of the corresponding conjugacy class. This corresponds to dividing by the number of 720 state symbol pairs that lead to the same T_i .

points of the corresponding time series. Then, eq. 3.15 and 3.66 imply

$$\begin{aligned}
T_{i+1} &= S_{i+1}^{-1} S'_{i+1} \\
&= (\varphi_k \varphi_{S_i(1)}^{-1} S_i(1, \dots, n))^{-1} \varphi_{k'} \varphi_{S'_i(1)}^{-1} S'_i(1, \dots, n) \\
&= (n, \dots, 1) S_i^{-1} \varphi_{S_i(1)} \varphi_k^{-1} \varphi_{k'} \varphi_{S'_i(1)}^{-1} S'_i(1, \dots, n) \\
&= (n, \dots, 1) S_i^{-1} \varphi_{S_i(1)} \varphi_k^{-1} \varphi_{k'} \varphi_{(S_i T)(1)}^{-1} S_i T(1, \dots, n).
\end{aligned} \tag{3.67}$$

For the question of redundancy in the symbolic description, i. e. mutual information between transfer symbols, it would be interesting to study how T_{i+1} behaves when S_i is varied (or is unknown). With the given algebraic description, this is difficult, because S_i enters at multiple places. The reason for this is the unfavorable description of the non-invertible truncation action (eq. 3.61), which illustrates the profound differences between the perspectives of rank orders and permutations.

3.3.5 Entropy Rate of a Symbolic Representation

The entropy rate of a stochastic process (S_i) is defined as the expectation value for the entropy of a symbol given the past of the series:

$$H = \mathbb{E}_i \{H(p(S_{i+1}|S_i, S_{i-1}, \dots))\}. \tag{3.68}$$

An upper bound is attained by independent uniformly distributed symbols, with an entropy rate of $\log_2(n!)$ bits. For a series of state symbols with equidistant sampling pattern $\tau = (0, \dots, n-1)$, the delay vectors of consecutive symbols s_i and s_{i+1} overlap. Therefore, the symbols are not independent, and one has to subtract the mutual information between a symbol and the past of the series. In the case of an equidistant sampling pattern, this mutual information consists of the rank order of the first $n-2$ values of the current symbol's delay vector. The remaining information is the rank of the last point, with respect to the first $n-2$ points. This rank is a 'one out of n ' information. This leads to a refined upper bound of $\log_2(n)$ bits, which is attained if the order of the last data point is uniformly distributed.

In a situation with a non-equidistant sampling pattern, all overlaps of a delay vector with its past must be considered for the restriction they pose on its rank order. As an example, consider the first k Fibonacci numbers as spacing of the sampling pattern (see fig. 3.13). This leads to $k-1$ overlapping pairs of values. The information contained in these overlaps even depends on the current symbol. In the example of fig. 3.13, it is possible that the three ranked pairs determine the rank order of the first four points completely, e. g. 'up-down-up' implies [2314]. It can also determine only parts of it, e. g. 'up-up-down' still leaves five options: [1342], [1423], [1432], [2341], [2431]. Therefore, the expected mutual information has to be considered.

Even more indirect information is possible. Suppose s_{i_0} implies $a > b$, and s_{i_1} implies $b > c$. Then we know that $a > c$, even if a and c do not appear in the same symbol. This is highly implicit information and depends not only on the sampling pattern but also on the values of the involved symbols. This can play a role for the entropy rate if a and c appear together in a symbol later than i_0 and i_1 . However, this sort of redundancy does not happen for equidistant sampling patterns, and therefore does not interfere with the following considerations.

The information content of a transfer symbol sequence is a more complex problem, so I will only discuss the case of an equidistant sampling pattern here. A straightforward upper

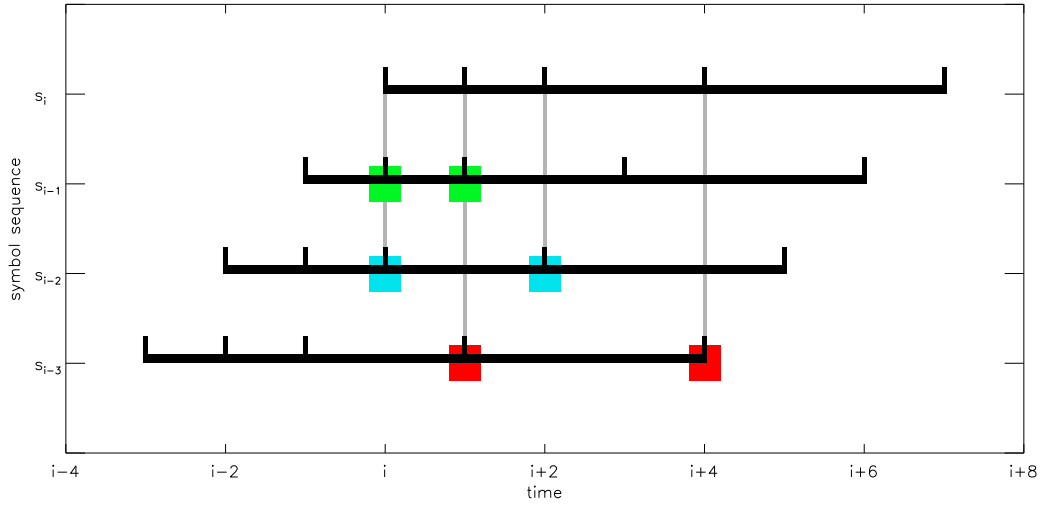


Fig. 3.13: For a sampling pattern $\tau = (0, 1, 2, 4, 7)$, the symbol s_i overlaps with each of the preceding symbols $s_{i-1}, s_{i-2}, s_{i-3}$ in one pair of values.

bound for the entropy rate is given by the combined entropy rate of the two underlying state symbol sequences, for which the aforementioned bound gives $2 \log_2(n)$ bits.

In order to obtain the entropy rate of the transfer symbol series, consider the conditional distribution of a transfer symbol t_{i+1} , given the complete past (t_i, t_{i-1}, \dots) of the series. In a first approximation, consider the $n!$ pairs of state symbols that correspond to the current transfer symbol t_i . Each state symbol has n possible successors, and a pair of successors determines the next transfer symbol t_{i+1} . For fixed t_i , this leads to an event space of $n!n^2$ cases for the distribution of the next transfer symbol t_{i+1} .

In contrast to the above situation for state symbols, the knowledge of preceding transfer symbols $(t_{i-1}, t_{i-2}, \dots)$ may forbid a certain number of those pairs. The expected entropy of this conditional distribution is the entropy rate of the series of transfer symbols. Therefore, the expectation value ranges over all overlapping preceding transfer symbols (the preceding $n - 1$ ones).

Using eq. 3.67, the entropy rate of the transfer symbol can be estimated (table 3.3; I consider T, k and k' in eq. 3.67 to be uniformly distributed). Since only the information of the preceding one or two symbols is considered, possible redundancies are neglected and the bound for the entropy rate is probably not attained. Note that for sequence length $n = 4$, there are only two preceding transfer symbols that share information with the current one, hence the estimate 3.76 is the final bound. Note that the above reasoning does not prove that the bound is actually attained by a pair of time series.

The results suggest that transfer symbols retain most of the information that is contained in the state symbol sequences. This implies that they capture most of the information that is contained in the corresponding pair of state symbol series, essentially carrying less redundancy, making them more efficient as a filter for relevant information.

Upper bounds for entropy rate [bits]			
n	4	5	6
from state symbols ($2 \log_2(n)$)	4	4.64	5.17
from $p(T_i T_{i-1})$	3.94	5.63	7.42
from $p(T_i T_{i-1}, T_{i-2})$	3.76	5.17	

Table 3.3: Estimated upper bounds for the entropy rate of a transfer symbol sequence (equidistant sampling pattern). The first row shows the upper bound given by the entropy rate of two state symbol sequences. The second row gives an estimation in terms of the conditional distribution for T_i given T_{i-1} . The third row uses the conditional distribution given both T_{i-1} and T_{i-2} . The missing value is due to the cost of calculation, which increases from left to right and from bottom to top.

Chapter 4

Application to a Model System: A Coupled Map Lattice

This chapter presents an application of symbolic representations to a *coupled map lattice* (CML). Section 4.1 gives an introduction to CML as commonly used prototype model systems to simulate the behavior of spatio-temporal systems of coupled oscillators. The lattice geometry, coupling mechanism, and local evolution of the chosen model are explained.

In section 4.2, the dynamical regimes of the system are examined, using well-known established measures to obtain a reference description of the various dynamical regimes. In this way, the two-dimensional parameter space is divided into reasonable subsets corresponding to prominent regimes.

Section 4.3 studies symbolic descriptions of the system dynamics, focusing on local synchronization effects. The algebraic order of transfer symbols contains enough information to allow a good classification of the different dynamical regimes, while reducing the dimension of the description space considerably. Furthermore, this section deals with forbidden symbols and the transitions between different dynamical regimes. Moreover, transfer symbol distributions are used to define different measures of symbolic complexity.

In section 4.4, the length and behavior of transients is studied in terms of a symbolic description. Section 4.5 deals with the stability of the stationary state, discussing the growth of global perturbations, the spatial propagation of local perturbations, and the effect of changes in the coupling parameters. This includes a model with spatially varying coupling parameters, where one large lattice is built as a representation of the whole parameter space. This allows to study the interaction of different coupling parameters in a single lattice. Section 4.6 closes the chapter with an approach using a symbolic description to predict the long term dynamics based on an early transient state of the system.

4.1 Introducing the Model System

4.1.1 Coupled Map Lattices

The focus of this chapter is the description of collective behavior, which emerges as a result of the interaction of individual active oscillators. In such systems, coupling between nonlinear oscillating objects can lead to *synchronization* and the emergence of global order. Phenomena of collective behavior are observed in a variety of systems from very different fields (see also Pikovsky et al. [76] for a broad overview):

- There are various approaches to explain synchronous flashing within groups of fireflies, ranging from an illusion (Laurent [52]) and random effect to a response to a leading individual (see Buck [19]). More recent explanations describe a coupling of individual oscillators without any hierarchy (i. e. no leading individual), where the details of the coupling mechanism differ from one species to another (see Buck [20]).
- The *Belousov-Zhabotinsky reaction* is an oscillating chemical reaction. The initial discovery in the early 1950s first received little attention ([111], cf [98]). In a spatially extended system, neighboring volume elements of the solution are coupled by diffusion of ingredients. This leads to an *excitable medium*, allowing traveling waves (Zaikin and Zhabotinsky [113], Winfree [110]). A model of a similar excitable medium based on a rock-paper-scissors game (Durrett and Levin [28]) was shown to exhibit the same sort of characteristic spiral waves (Reichenbach et al. [79]).
- At its opening in 2000, the Millennium Bridge in London, a lightweight pedestrian bridge over the River Thames, experienced a problem with unexpected lateral vibrations and had to be closed soon afterwards. The effect could be explained by walking pedestrians acting as oscillators coupled by the bridge. The effect of emerging synchrony repeatedly occurred once the pedestrian density on the bridge exceeds a certain threshold (Strogatz [99]). By now the bridge has been modified to suppress the vibration effects.

Many fundamental behavioral features of coupled systems can already be observed when considering a finite number of locally coupled time-discrete oscillators connected in a simple geometry, a so called *coupled map lattice* (CML). Characteristic features of a CML are (see Chazottes and Fernandez [23])

1. discrete time dynamics,
2. discrete nature of the underlying space (lattice or network), in most cases consisting of identical components, and
3. continuous local variables (real numbers or vectors).

In other words, a CML is a dynamical system which is discrete in time and space. It differs from a *cellular automata* by its continuous state space, and from a *partial differential equation* (PDE) by its discrete space and time. In nature, there are many coupled systems that are modeled by PDEs. These systems are often too complex to be studied analytically, therefore a discretization in space and time can be a useful approximation. In any case, such an approximation is necessary in order to numerically simulate a physical system described by a PDE. Since this discretization step in both space and time is all that distinguishes a PDE from a CML, one might say that by using a numerical simulation, one turns a PDE into a CML.

CML can show, dependent on the parameters, a multitude of behavior like chaos, synchronized oscillations, intermittency, emergence of spatial patterns or stable steady states (see [7], [8], [25], [45]). They are therefore widely used as model systems for the rich dynamical behavior that is characteristic for coupled systems. Even though the different sorts of emerging spatio-temporal behavior are often obvious from a qualitative perspective, it is not always clear how to formalize the description of their order properties. In this context, symbolic representations are particularly well-suited for the application to coupled map lattices.

4.1.2 The Logistic Map

Since a CML is time-discrete, the behavior of the components is described by a recursion formula. Here, I will use the *logistic map*, which is a simple discrete model for population dynamics and a standard example for the emergence of chaos. It is defined by the *first order difference equation* (see May [63] for an overview of this class of models):

$$x_{n+1} = rx_n(1 - x_n) =: f(x). \quad (4.1)$$

In the original interpretation of eq. 4.1, the value $x_n \in [0, 1]$ describes the population size of a species at time n . The first factor $r \in [0, 4]$ is a control parameter for the growth rate. The growth is limited by the population size (second factor) and a third factor that can be interpreted as an effect of limited space or resources. While the time-continuous *logistic equation* always converges to a stable equilibrium, the logistic map can exhibit oscillations and even chaotic dynamics.

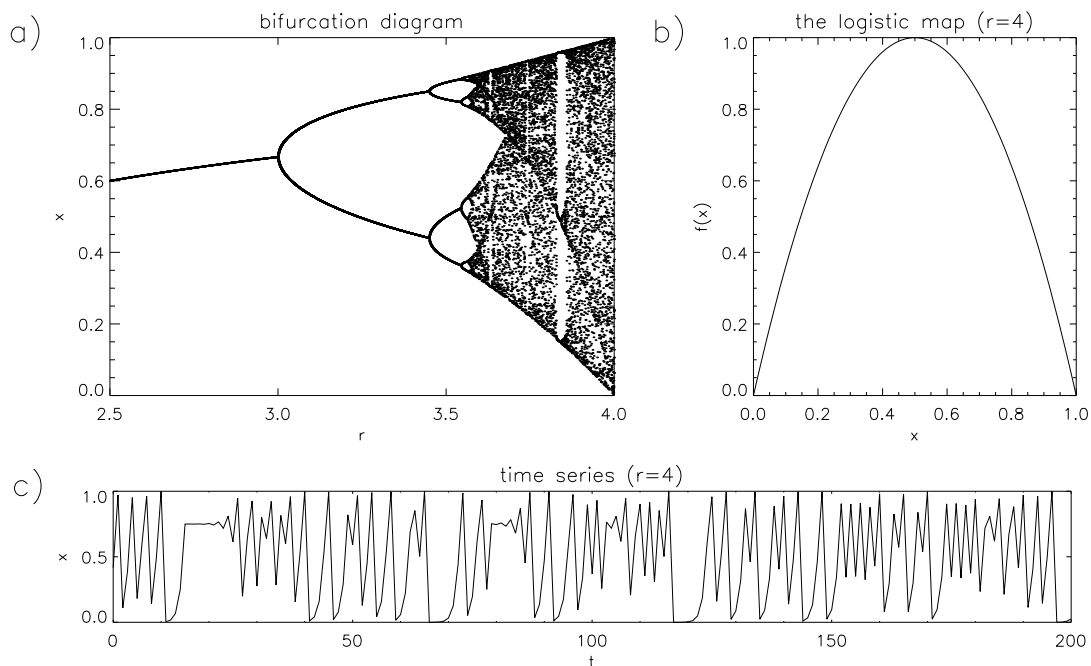


Fig. 4.1: The logistic map. a) Bifurcation diagram for the control parameter $r \in [2.5, 4]$. b) Mapping for $r = 4$. c) Segment of a time series for $r = 4$ and generic initial condition.

In order to sketch the dynamics of the logistic map, it is useful to study its bifurcation behavior. A *bifurcation diagram* characterizes the dynamics of a system by its typical long

term values. This is done by plotting values from sufficiently large times as a function of a control parameter of the system. Fig. 4.1a shows the bifurcation diagram of the logistic map for $r \in [2.5, 4]$. In a sequence of bifurcations called *period doubling cascade*, the system undergoes a transition from a stable equilibrium to a chaotic regime. The chaotic regime is frequently interrupted by *self-similar periodic windows*, whose size, position and order follow a universal scaling relation [32]. The logistic map has frequently been used as a base component to model coupled systems (see for instance [8], [27], [45], [70]).

4.1.3 The CML Model System

Geometry and Coupling

The model used here is a square lattice of cells, each described by the logistic map and coupled to its four nearest neighbors. The boundary conditions are periodic, hence the actual geometry of the lattice is the one of a flat torus (as opposed to the surface of a solid 'donut', which contains regions of both positive or negative curvature). Following the model of Atmanspacher et al. [8], the coupling mechanism is described by

$$x_k = (1 - \epsilon)f(x_{k-1}) + \frac{\epsilon}{4} \sum_{x' \sim x} ((1 - \alpha)f(x_{k-1})' + \alpha x'_{k-1}), \quad (4.2)$$

where f is the logistic map with $r = 4$ and \sim denotes the neighbor relation of the lattice. The parameter $\epsilon \in [0, 1]$ is the total coupling strength. The model describes two kinds of coupling: instant coupling, where each cell is drawn to the value of its neighbors, and delay coupling, where each cell is drawn to the value its neighbors had before the logistic map was applied, see fig. 4.2. The second control parameter $\alpha \in [0, 1]$ is the percentage of the coupling that is attributed to the delayed effect.

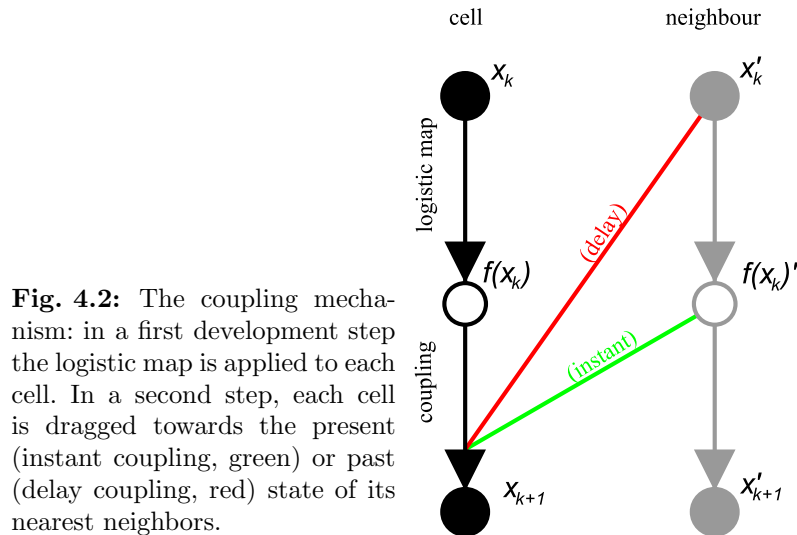


Fig. 4.2: The coupling mechanism: in a first development step the logistic map is applied to each cell. In a second step, each cell is dragged towards the present (instant coupling, green) or past (delay coupling, red) state of its nearest neighbors.

In order to obtain a first impression of the rich dynamical behavior of the system, let us consider some limit cases. At $\alpha = 0$, the coupling corresponds to the classic model introduced by Kaneko [45]. Without coupling ($\epsilon = 0$), each cell individually follows the well-known dynamics of the chaotic logistic map. For maximal coupling strength $\epsilon = 1$, the state x_k of a cell

depends only on the previous states x'_{k-1} of its neighbors, but not on its own past x_{k-1} . This splits the system into two independent subsystems (see section 4.2.3 for details on this effect).

Together with related coupling schemes, the model was used in [7] [8] to study stabilization behavior, focusing on stable equilibrium points. This work takes a more general perspective, including various other regimes with different degrees of spatial and/or temporal order.

In the following, $x(t) \in X$ will denote the *state* of the system at the t -th iteration, where $X = [0, 1]^{n \times n}$ is the *state space* of the system. The value of a single cell is denoted by $x_i(t)$, and a set $\{x(t) | t \in [t_0, t_1]\}$ is called a trajectory of the system.

The system was numerically simulated using a 4th order Runge-Kutta method (see [78]).

4.1.4 Model Assumptions

The construction of eq. 4.2 separates the local evolution $x_k \mapsto f(x_k)$ and the coupling $f(x_k) \mapsto x_{k+1}$ into two different steps. In a realistic model, such a construction only makes sense if the corresponding processes do not overlap. Sometimes it is said that the time scales of the processes must be different, but I propose that it is mainly the separation (or the amount of overlap, respectively) that matters. Examples where a separation of this kind would be appropriate are biological systems where the processes are tied to different seasons, or where one of the processes happens in short bursts.

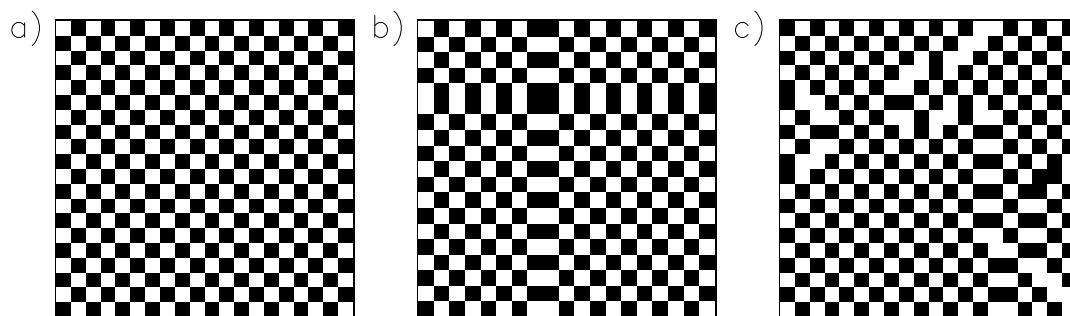


Fig. 4.3: The *checkerboard* structure. a) Global order without defects. b) Global defect at odd side length. c) Defects separating incompatible phases.

The geometric structure of the square lattice with its high symmetry is an important assumption. In this geometry, there exist spatial structures that do not exist for random networks, possibly influencing the synchronization properties. The most prominent example in this system is the *checkerboard* structure: the cells of a square lattice of even side length can be split into two groups, such that any cell of one group is connected only to cells of the other group (fig. 4.3a). For even side length the structure is compatible with the periodic boundary condition, for odd side length it can not exist without global defects¹ (fig. 4.3b). In some

¹Consider a *Riemannian manifold*, and a structure that is defined locally and can be continued smoothly on the neighborhood of any point where it is defined. When starting from a base point and continuing the structure in every direction, one can get problems at points where the shortest path to the base point is not unique. This set of points is called the *cut locus*. There, the structure may not be well defined, because the continuations via different paths may contradict. Therefore, the cut locus is an upper bound for the defects that can not be eliminated if a pattern is not compatible with the topology of a space. On a flat 2-Torus, the cut locus (for any base point) consists of two intersecting rings, which are marked by the defects in fig. 4.3b.

regimes there are locally stable checkerboard solutions, which either eventually spread over the lattice, or leave defects separating different incompatible phases of the solution (fig. 4.3c).

4.2 Prominent Dynamical Regimes

4.2.1 Conventional Measures

This section presents conventional measures that are commonly used to examine the dynamics of complex systems. They are used to identify different regimes of the system and to locate them within the parameter space.

Bifurcation Diagrams

Fig. 4.4 shows typical bifurcation diagrams (as introduced in section 4.1.2) of the system. Since in this case both the system and the parameter space have more than one dimension, a graph can not show the full information. The plots show bifurcation diagrams along cuts of the parameter space, where the delay α is fixed and the coupling strength $\epsilon \in [0, 1]$ is varied. On the vertical axis, values from randomly chosen cells are plotted.

Chaotic states show distributions that are scattered over parts or the complete state space. They are interrupted by ordered windows, where there is regularity in space and/or time, up to strictly periodic limit cycles. There are 'noisy' period doubling cascades, where the noise can originate from spatial (structures with or without defects) or temporal (i. e. intermittency or multiple attractors) phenomena. Furthermore, there exists a 'clean' period doubling cascade (e. g. $\epsilon = 0.8$, from $\alpha = 0.42$ to 0.175). Another prominent feature is the splitting of the long term states into two or more *bands*, which may be a sign for phase-synchronized dynamics with fluctuating amplitudes.

Lyapunov Exponents

As a common indicator for chaos, the *maximum Lyapunov exponent* (MLE, see section 2.1.1) is shown in fig. 4.5a. It is calculated from the time series of single cells using the algorithm proposed by Wolf et al. [112] with a delay-coordinate embedding (using 10^3 data points and a sampling pattern $\tau = (0, 1)$). The result is averaged over the lattice. The algorithm does not yield negative values of the MLE. Thus, negative fluctuations are set to zero and the result vanishes on a large area of the parameter plane. Note that the calculation of negative Lyapunov exponents needs information on the transient dynamics. Therefore, they might not be accessible by studying a single trajectory with a possibly short transient.

Recurrence Rate

In the study of temporal properties of a trajectory, one can investigate temporal structures in terms of the recurrences of past states. In many systems, the existence of recurrences is given by the Poincaré recurrence theorem (theorem 2.1 in section 2.1.1).

This motivates the definition of *recurrence plots* (see Eckmann et al. [29] and Marwan et al. [61]), which describe the repetition of similar states along a trajectory. The recurrence plot

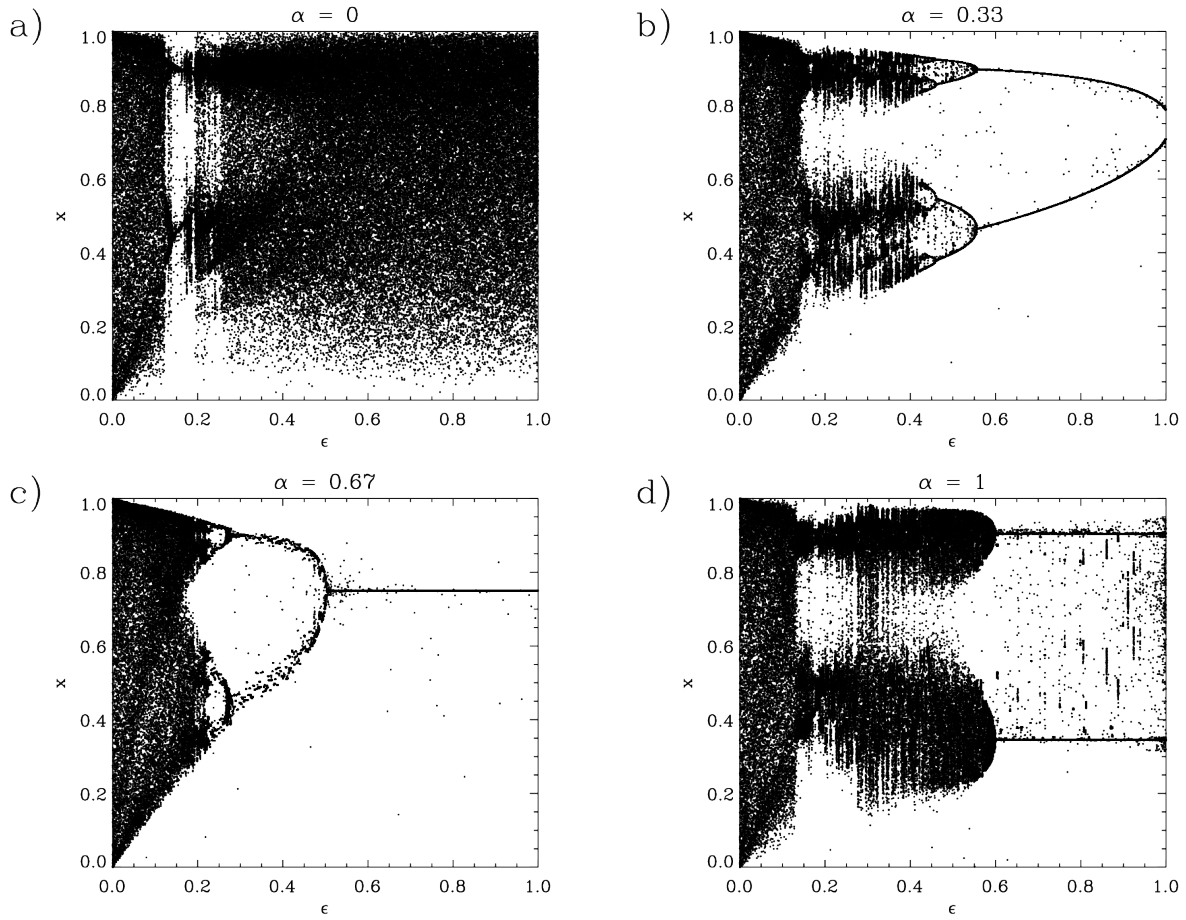


Fig. 4.4: Bifurcation diagrams for a lattice of 20×20 cells. Starting from a random initial condition, random samples are plotted from times $t \geq 10^5$. a) $\alpha = 0$, b) $\alpha = 0.33$ c) $\alpha = 0.67$ d) $\alpha = 1$, with ϵ running from 0 to 1.

of a trajectory $x(t)$ is a two dimensional matrix defined as

$$r_{\tau_1 \tau_2} = \begin{cases} 1 & \text{if } d(x(\tau_1), x(\tau_2)) \leq d_0 \\ 0 & \text{else,} \end{cases} \quad (4.3)$$

where d is a distance measure, and d_0 the distance threshold that defines a recurrence. Often, the threshold is chosen such that a given *recurrence rate* r (relative frequency of recurrences) is attained. *Recurrence quantification analysis* offers a multitude of methods to analyze and quantify the structures found in recurrence plots. Groth [39] introduced the application of recurrence plots to symbolic representations as *order recurrence plots* (see also Schinkel et al. [87], Jordan et al. [44]).

As a straightforward measure for the behavior of the system in time, I make use of the recurrence rate (see fig. 4.5b). The base space for the recurrence plot is the state space of the system with a Euclidean distance measure, and a trajectory is followed for 200 time steps. A small distance threshold $d_0 = 10^{-4}$ is used, in order to focus on exact returns to previous states. Due to the high embedding dimension (400 for a lattice of 20×20 cells), a notable number of events is observed only if the system as a whole is on a periodic orbit.

Correlation of Neighboring Cells

I investigated the spatial properties of the different regimes by evaluating the system at one point in time. A basic concept of spatial order is that the state of a cell is similar to that of its neighbors. To quantify this with a straightforward linear measure, the correlation coefficient between the values of neighboring cells is calculated based on the state of all cells at one moment. This measure, shown in fig. 4.5c, can be used to distinguish different kinds of cluster formations: while positive correlation coefficients indicate coherent areas of uniform behavior, negative coefficients point to a spatially regular but alternating cell behavior, primarily forming patches of the checkerboard structure shown in Fig. 4.3.

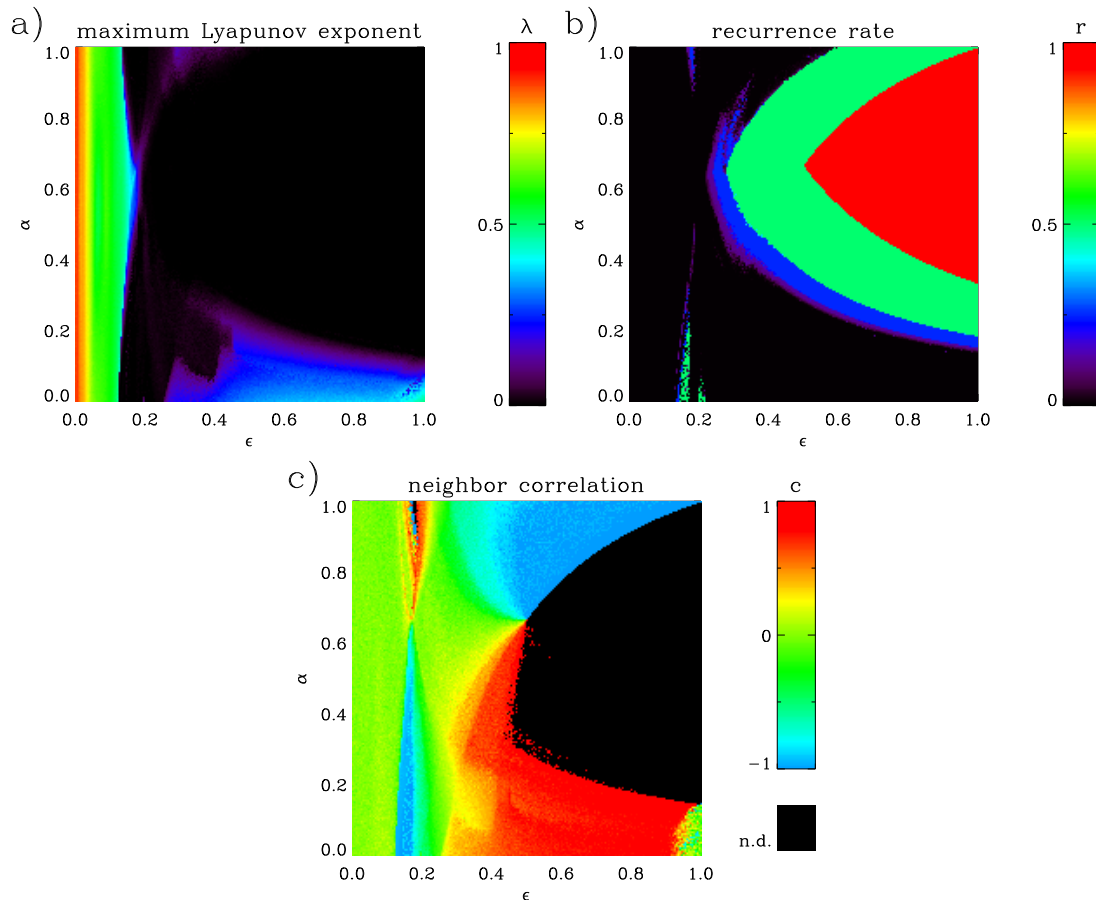


Fig. 4.5: Description of the parameter space by means of conventional measures: a) Maximum Lyapunov exponent (MLE, from one time series, averaged over the lattice). b) Recurrence rate. c) Correlation between neighboring cells in the lattice (not defined if all cells have the same value, i. e. for total synchronization).

4.2.2 Phase Diagram of the Parameter Space

As a summary of the characterizations introduced in section 4.2, fig. 4.6b displays the main regimes of the model system. The regions are defined in terms of a hierarchical set of rules (the decision tree is shown in fig. 4.6a):

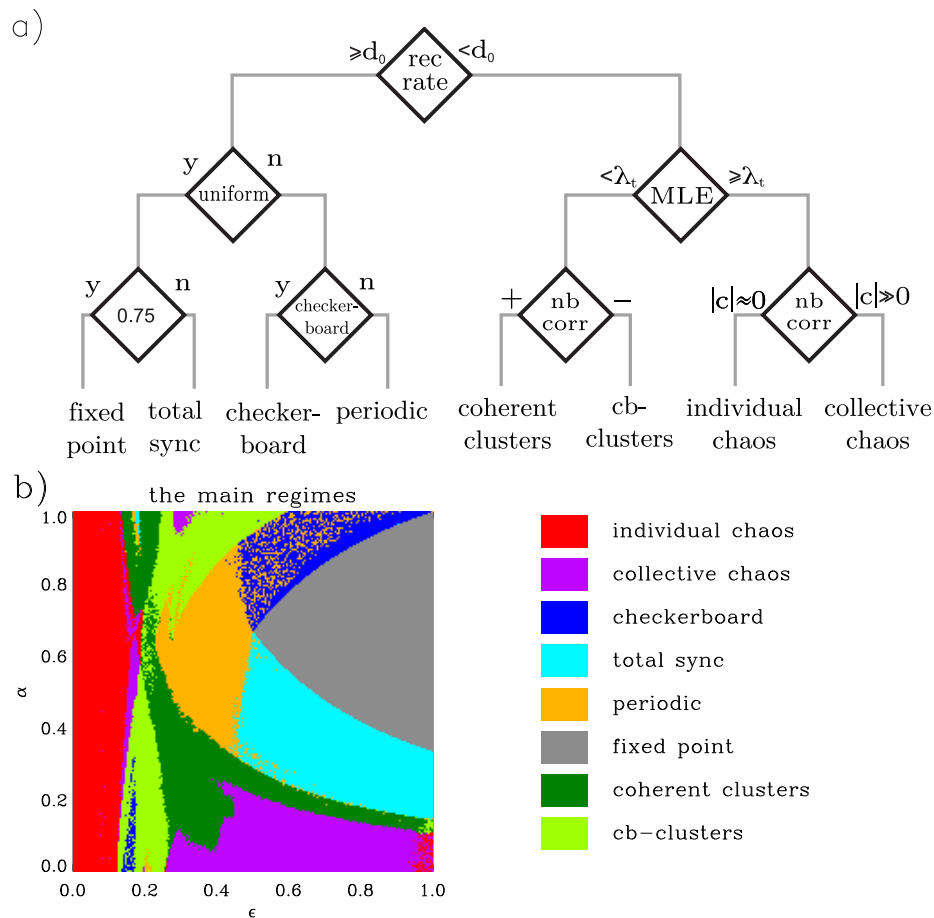


Fig. 4.6: Phase diagram of the main regimes. a) Decision tree. b) Phase diagram.

1. At the highest level of the decision tree, temporal regularities are considered. Periodic regimes are detected by means of a (significantly) positive recurrence rate. The used threshold $d_0 = 0.05$ corresponds to ten times the area of the plot diagonal.
2. Within the periodic regimes, total synchronized states are distinguished from those that are not spatially uniform. The regimes of total synchronization are divided into the temporally uniform cases, where all cells have reached a fixed-point (gray color) and those with period of at least two (light blue). The states that do not show total synchronization again split into two classes of spatial behavior: First regular checkerboard patterns (dark blue) and second, spatially irregular periodic areas (yellow).
3. Among the remaining (non-periodic) states, first the MLE is used to discriminate between chaotic ($\lambda > \lambda_t$) and non-chaotic ($\lambda < \lambda_t$) behavior, with a threshold of $\lambda_t = 0.08$. The resulting two classes can be subdivided with respect to their spatial uniformity, using the correlation between the time series of neighboring cells. Spatially uncorrelated chaotic behavior ($|c| < c_t$, red) is observed, as well as 'collective' chaotic behavior with correlation between neighboring cells ($|c| \geq c_t$, purple), using a separation threshold $c_t = 0.15$. Within the non-chaotic states, there is a transition from coherent clusters of synchronized behavior to clusters of cells with alternating behavior forming the afore-

mentioned checkerboard pattern. To represent this transition, I differentiate between positive (dark green) and negative next neighbor correlations (light green).

4.2.3 Characterization of the Regimes

Individual Chaos

At the left border of the parameter space ($\epsilon = 0$), the system consists of uncoupled cells, thus each cell independently exhibits the chaotic dynamics of the logistic map. Note that for $\epsilon = 0$, the delay α has no effect. Hence the corresponding parameter sets all describe the same coupling mechanism. The MLE starts at 0.9 for $\epsilon = 0$, which is the Lyapunov exponent of an isolated logistic map. For increasing ϵ , it first gradually declines to a plateau of about 0.5–0.6, then sharply drops to 0, giving the region a distinct boundary. See fig. 4.7a for a typical system state and time series of this regime.

Collective Chaos

In the context of a system of coupled oscillators, the term *order* can refer to different concepts, including *collective* or *predictable* behavior. The second chaotic regime at the bottom of the parameter space (fig. 4.7b) is noteworthy because the coupling leads to dynamics that are collective but not predictable, indicating that these concepts of order do not always coincide. With increasing coupling strength ϵ , the behavior becomes slightly more spatially ordered. The right border with $\epsilon = 1$ deserves special attention, see below. The Lyapunov exponent reaches values of 0.2–0.4.

Fixed Point

The logistic map has an unstable fixed point at 0.75, which for the coupled system becomes stable for some control parameters (fig. 4.7c). The synchronization first occurs at $\alpha = \frac{2}{3}$. This is probably related to a result by Masoller and Marti [62], who studied a related system, and observe that a coupling mechanism with mixed delays (in their case randomly chosen) leads to better synchronizability than uniform delays. The transition occurs via a dying period-2 oscillation, which is totally synchronized at small α , while it forms a checkerboard geometry for large α . This transition will be examined analytically in section 4.2.4.

Periodic

In the phase diagram (fig. 4.6b), the region around the fixed point forms a regime of periodic oscillations, in the sense that the time series of each cell is periodic (fig. 4.7d). When approaching the inner border to the fixed point regime, the oscillations decay, while at the outer border the cells lose their coherency. The spatial structure varies in a smooth transition from spatially uniform (*total synchronization*) to anti-phase clusters forming *checkerboard* patterns. These two extremes of spatial order will be treated as different regimes.

Total Synchronization

In *total synchronization* (fig. 4.7e), every cell has exactly the same time series, thus the state of the system is spatially uniform. At the boundary to the collective chaos regime a period doubling cascade is observed. This is the only regime exhibiting periods longer than 2. Note

that formally, total synchronization includes the fixed point, but it is useful to treat it as a separate regime.

Checkerboard

As introduced in section 4.1.4, the symmetry of the lattice geometry allows a splitting into two clusters with only inter-cluster connections. Within the period-2 regime, there is such a splitting into two anti-synchronized clusters (fig. 4.7f). At the border to the non-periodic regimes, the oscillations lose coherency. Since there exist two incompatible phases of the checkerboard structure, there are cases where both phases are present (separated by a line of defects). For odd lattice sizes this configuration can not exist globally, and therefore such defects must exist. Since the checkerboard structure is equally common for even and odd lattice sizes, global defects seem not to have an important effect on its stability.

The Clustered Regimes

The rest of the parameter space is governed by dynamics that are neither chaotic, nor strictly ordered. Since there is a transition between spatially smooth states and local checkerboard patches, I split these cases into two regimes, namely states with positive and negative neighbor correlation. This corresponds to a tendency for coherent clusters or checkerboard-clusters (fig. 4.7g and h), respectively.

Amritkar and Jalan [6] study a related system (scale-free network) for $\alpha = 1$, and observe several regimes. For ϵ running from 0 to 1, they find turbulent behavior, phase synchronized clusters, intermittent phase synchronization, and finally a regime of anti-phase clusters. This is in good agreement with the regimes observed here.

The Border at $\epsilon = 1$

This section will explain why the extremal parameter $\epsilon = 1$ corresponds to an exceptional coupling mechanism. In this case, the coupling equation (eq. 4.2) becomes

$$x_{t+1} = \frac{1}{4} \sum_{x \sim x'} ((1 - \alpha) f(x'_t) + \alpha x'_t), \quad (4.4)$$

and the next iteration x_{t+1} of a cell depends only on the state x'_t of the neighbors but not on x_t .

Suppose the lattice size is even. To understand the consequences of the extremal coupling, consider the lattice as a checkerboard with each cell labeled as either black or white. The next step of any black cell depends only on the current state of its neighbors, all of which are white. Hence, knowing the initial condition ($t = 0$) of the white cells is enough to determine the state of all black cells at the odd times, and all white cells at the even times. In other words, this part of the system information forms a subsystem that is uncoupled from the rest of the lattice. The rest of the cells forms a similar subsystem, consisting of the black cells at odd times and the white cells at even times.

For small α , this behavior is clearly reflected in the dynamics. The collective chaos region for small α and large ϵ is mainly characterized by locally correlated states. However, in the neighborhood of $\epsilon = 1$ there appear fluctuating checkerboard patches, which can be explained as an interleaving of two independent clusters in a checkerboard pattern. In the

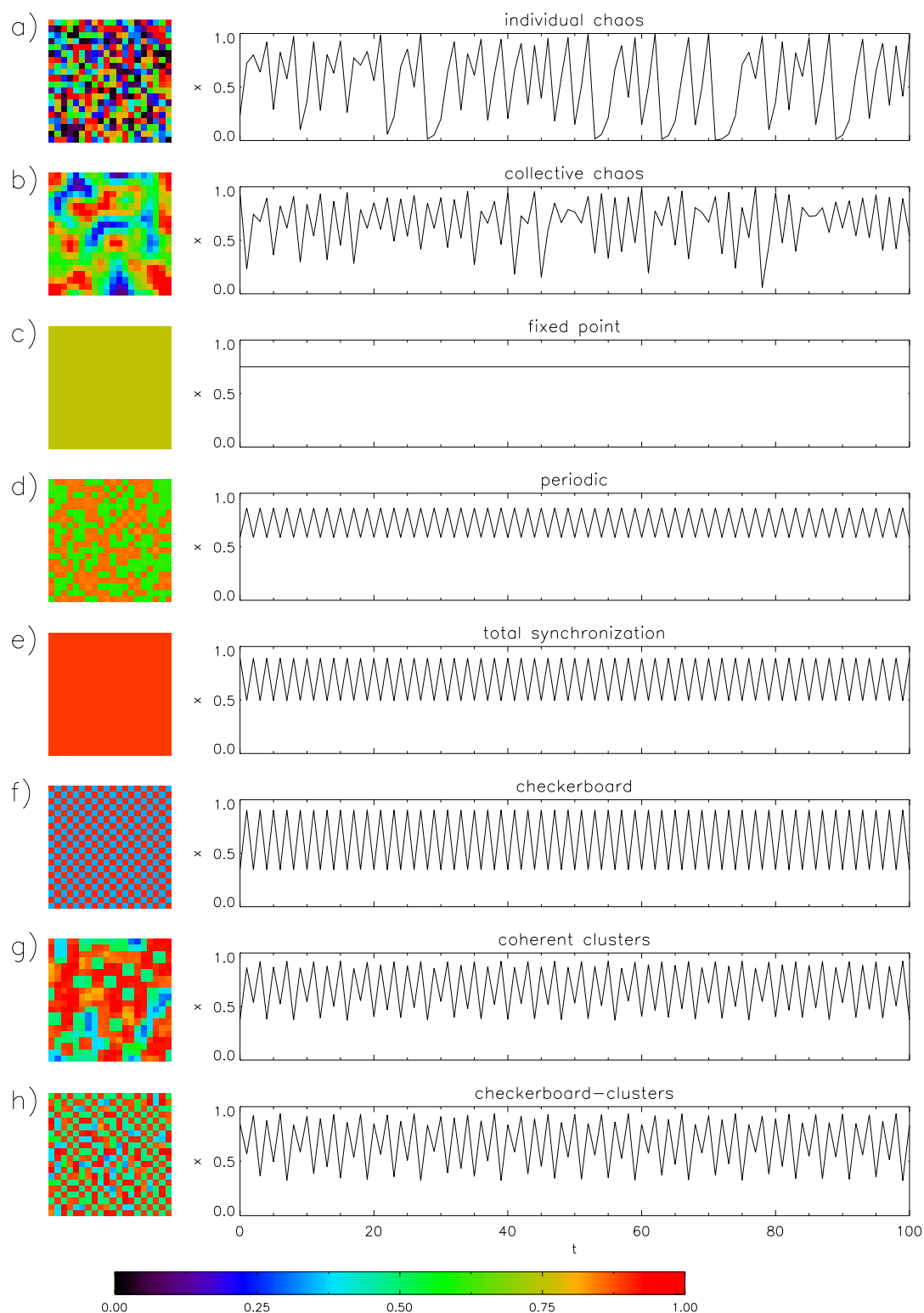


Fig. 4.7: Typical lattice states (left) and corresponding time series of a single cell (right) for the main regimes: a) Individual chaos b) Collective chaos c) Fixed point d) Periodic e) Total synchronization f) Checkerboard g) Coherent clusters h) Checkerboard-clusters.

ordered regimes at larger α , there is no apparent change when ϵ approaches 1, because both subsystems approach the same ordered state.

In conclusion, in all cases, the two subsystems have similar dynamics. In the chaotic regime, the independence leads to uncorrelated behavior of the two halves, while in the fixed point regime independent systems still lead to a uniform result. One might expect to occasionally see opposing phases in the periodic regime, which are not observed. I conjecture that the starting procedure of the system favors certain phases, leading to a symmetry breaking (which is discussed in section 4.2.5). See also section 4.5.2 for the fact that, dependent on the implementation, numerical roundoff errors can induce a coupling in the order of the computational accuracy (about 10^{-15} for double precision floating-point arithmetic).

4.2.4 Analytical Description of the Fixed Point Regime

For the fixed point regime, some considerations can be done in an analytical manner. They confirm the boundaries of the region in the state space and explain the spatial structure in the adjacent regions. This section summarizes analytical work of Atmanspacher et al. [7] on the stability of the fixed point. They worked on a coupled map lattice, and studied several sorts of coupling, including the system discussed here. They describe the coupling of the lattice in terms of its *adjacency matrix*

$$A_{ij} = \begin{cases} 1 & \text{if } x_i \sim x_j \\ 0 & \text{otherwise} \end{cases} \quad (4.5)$$

and its *valence matrix*

$$V_{ij} := \begin{cases} \sum_j A_{ij} & \text{if } i = j \\ 0 & \text{otherwise} \end{cases} \quad (4.6)$$

For the system used here, A has a relatively simple form, and $V = 4 \cdot Id$. The eigenvalues of $V^{-1}A$ are [7]

$$\lambda_k = \frac{1}{2} \cos(\phi_1) + \frac{1}{2} \cos(\phi_2) \quad \text{with} \quad \phi_i = \frac{2\pi k_i}{n}, k_i = 0, \dots, n-1. \quad (4.7)$$

Stability Conditions

For a stability analysis of the fixed point, they consider fluctuations in the basis (u_k) of eigenvectors of $V^{-1}A$:

$$u_n := \bar{u} + \delta a_n^k u_k, \quad (4.8)$$

where \bar{u} is a constant solution. Applied to the system (eq. 4.2), this leads to

$$\delta a_{n+1}^k = (1 - \epsilon) f'(\bar{u}) \delta a_n^k + \epsilon \lambda_k ((1 - \alpha) f'(\bar{u}) \delta a_n^k + \alpha \delta a_n^k). \quad (4.9)$$

Inserting the logistic map (eq. 4.1), the constant solution \bar{u} is stable if the following inequalities hold:

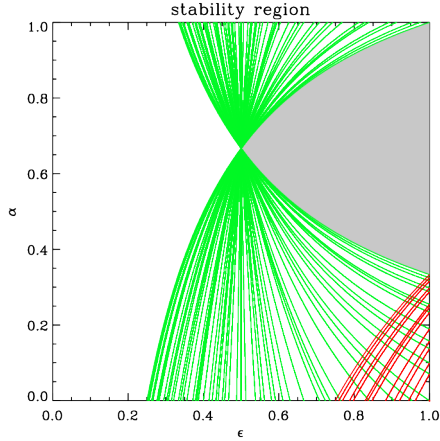
$$1 < \epsilon(2 + \lambda_k(3\alpha - 2)) < 3 \quad \forall k. \quad (4.10)$$

Fig. 4.8 shows the critical sets of the inequalities of eq. 4.10, in other words the parameters for which the middle part equals either 1 (green) or 3 (red).

Note that the λ_k are bounded by ± 1 . These bounds define the strictest conditions,

$$\alpha > \frac{1}{3\epsilon} \quad \text{and} \quad \alpha < \frac{4}{3} - \frac{1}{3\epsilon}. \quad (4.11)$$

Fig. 4.8: Stability region of the fixed point. The lines mark the critical parameters where an eigenmode gets unstable. The stability region (gray) is on the right of all green and on the left of all red lines.



For even side length, $\lambda_k = \pm 1$ is always attained, for odd side length the value -1 is only attained in the limit of large lattice sizes. These borders are in agreement with the fixed point regime as it is observed in numerical simulations. Note that, at the upper border, the condition for the smallest eigenvalue -1 ceases to hold, at the lower border the condition for the largest eigenvalue $+1$ gets critical. The tip at $\alpha = \frac{2}{3}$ is critical for all eigenvalues.

Eigenvectors

The eigenvectors correspond to different modes of perturbation with respect to the constant solution. In our system, there are two important modes corresponding to the strongest stability conditions (eq. 4.10). They are the first emerging degrees of freedom of the dynamics outside the fixed point regime. These modes can be given explicitly (example for size 6). With blocks of the form

$$a := \begin{pmatrix} 0 & 1 & 0 & 0 & 0 & 1 \\ 1 & 0 & 1 & 0 & 0 & 0 \\ 0 & 1 & 0 & 1 & 0 & 0 \\ 0 & 0 & 1 & 0 & 1 & 0 \\ 0 & 0 & 0 & 1 & 0 & 1 \\ 1 & 0 & 0 & 0 & 1 & 0 \end{pmatrix}, \quad b := \begin{pmatrix} 1 & 0 & 0 & 0 & 0 & 0 \\ 0 & 1 & 0 & 0 & 0 & 0 \\ 0 & 0 & 1 & 0 & 0 & 0 \\ 0 & 0 & 0 & 1 & 0 & 0 \\ 0 & 0 & 0 & 0 & 1 & 0 \\ 0 & 0 & 0 & 0 & 0 & 1 \end{pmatrix}, \quad (4.12)$$

the adjacency matrix has a block form,

$$A = \begin{pmatrix} a & b & 0 & 0 & 0 & b \\ b & a & b & 0 & 0 & 0 \\ 0 & b & a & b & 0 & 0 \\ 0 & 0 & b & a & b & 0 \\ 0 & 0 & 0 & b & a & b \\ b & 0 & 0 & 0 & b & a \end{pmatrix}. \quad (4.13)$$

The results of numerical simulations suggest the following candidates for eigenvectors: at the lower border there is complete synchronization, which corresponds to the vector

$$v := (1, 1, 1, 1, 1, 1, 1, 1, 1, 1, 1, \dots). \quad (4.14)$$

The behavior at the upper border corresponds to the 'checkerboard-vector'

$$w := (1, -1, 1, -1, 1, -1, \dots, -1, 1, -1, 1, -1, 1, \dots). \quad (4.15)$$

It is easy to check, that these are the eigenvectors of $V^{-1}A$ with eigenvalues 1 and -1 , which means they are the first undamped modes that emerge when leaving the fixed point regime. For odd lattice size, a 'checkerboard vector' does not exist. Hence, the smallest eigenvalue of $V^{-1}A$ is slightly larger than -1 and has a multiplicity of 4 (both cosine terms each have two minima). Therefore, more complex behavior is expected at the upper border. Numerical simulations suggest that the corresponding modes have the form of checkerboard patterns with global defects (see section 4.1.4). At the tip of the stationary region, the stability conditions for all eigenvalues are violated. In agreement with this, spatially unordered behavior is observed in the numerical simulations.

4.2.5 Dependence on Initial Conditions

In the study of CML, one normally uses a random initial condition. However, the used generating mechanism is often not specified in detail. In this section, I discuss an observation, where the probability distribution of the random initial condition leads to a symmetry breaking, which can have a considerable influence on the synchronizability of the system.

The system has a regime, where it locally develops clusters with a synchronized period-2 oscillation, which alternates around the fixed point at 0.75. At large times, either one of the phases spreads over the whole lattice, or the system stabilizes, forming a small number of clusters.

Since the system is invariant under time shift, one would expect the two possible phases to be uniformly distributed. However, when drawing the initial value of each cell independently from a uniform distribution, a significant preference for one phase is observed (namely the one that corresponds to low values at even time steps). Using the natural distribution of the logistic map leads to the same result. In a situation where two phases compete for dominance, such a bias for one of them probably favors total synchronization (as opposed to the coexistence of stable clusters).

In order to examine the consequences of this symmetry breaking for the system's capability to synchronize, I modified the distribution of the random initial condition such that the phases become more equally probable at large times. The new distribution has a fixed median m , and the upper and lower half of the probability is distributed uniformly in the intervals $[0, m]$ and $[m, 1]$, respectively. I quantified the asymmetry of the phases by the difference between the number of cells in each phase (fig. 4.9a). The synchronizability of the system was measured by the spatial standard deviation of the system, at large times after transients (fig. 4.9b). The initial condition with $m = 0.1$ leads to a fairly symmetric average distribution of the phases. However, it allows coexisting clusters in regions where the standard initial condition ($m = 0.5$) only allows total synchronization.

I conclude that the mechanism of choice for random initial conditions has a considerable influence on the synchronizability of the system. It would be desirable to start the system in a 'neutral' way that preserves its symmetries. However, it is not clear how to define such a 'neutral' distribution for random initial conditions in a natural way (note that such a distribution will probably depend on the system parameters).

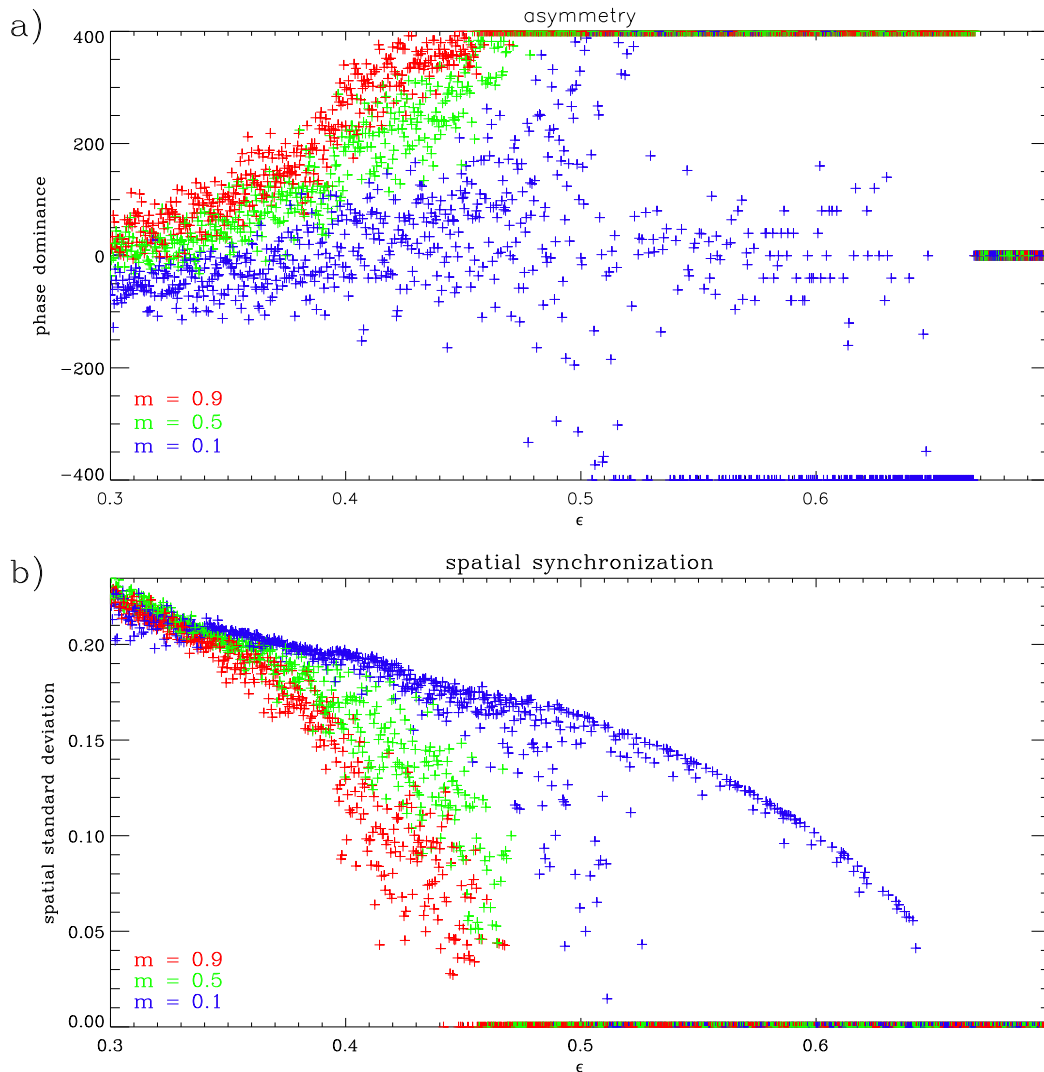


Fig. 4.9: Initial conditions and symmetry. Comparison of different generating distributions for random initial conditions, for parameters in the periodic regime ($\alpha = 0.5$, $\epsilon \in [0.3, 0.7]$). The transition at $\epsilon \approx 0.67$ marks the beginning of the fixed point regime. a) Asymmetry in the distribution of the two phases. b) Spatial standard deviation σ of the system state ($\sigma = 0$ indicates total synchronization).

4.3 Symbolic Description of the System Dynamics

4.3.1 Order Distribution of Transfer Symbols

Now that the system is introduced and the dynamical regimes are known, I present an application of symbolic representations to CML, in order to show, how this description reflects their properties.

A focus of the analysis was the emergence of local order. As aforementioned, the coupling mechanism (eq. 4.2) defines a neighborhood relation between the cells of the lattice. Using this, the local dynamics of the lattice can be described by transfer symbols between the time series of neighboring cells. This allows a spatially resolved description. Since the system is discrete in

time, the choices for the embedding parameters are limited to integer delays. I used a uniform sampling pattern with $\tau = 1$ and $n = 4$.

A central concept in this work is the distribution of the algebraic order of transfer symbols, counted over all pairs of neighboring cells in the lattice. This can be considered as a mapping to a simplified state space of the high-dimensional system. At sequence length $n = 4$, the order can take the values from 1 to 4, hence a normalized distribution has 3 degrees of freedom. Formally, the simplified state space is the *affine space* spanned by the orders 1 to 4, however the set of normalized order distributions is the *convex hull* of the orders. In contrast, the full state space of the system, considering the 20×20 lattice used here, has 400 dimensions.

Such a low-dimensional description space is useful for visualizing states of the system in a condensed manner, to plot transient behavior, for cluster analysis, and to sample structures in the space with a reasonable amount of data (see 'curse of dimensionality' in section 3.1.6).

In the following, I will show that the proposed order distribution captures essential properties of the system's dynamics, and is powerful enough to distinguish the main dynamical regimes of the system. This gives an idea of the aspects of the dynamics that are uncovered by the symbolic representation.

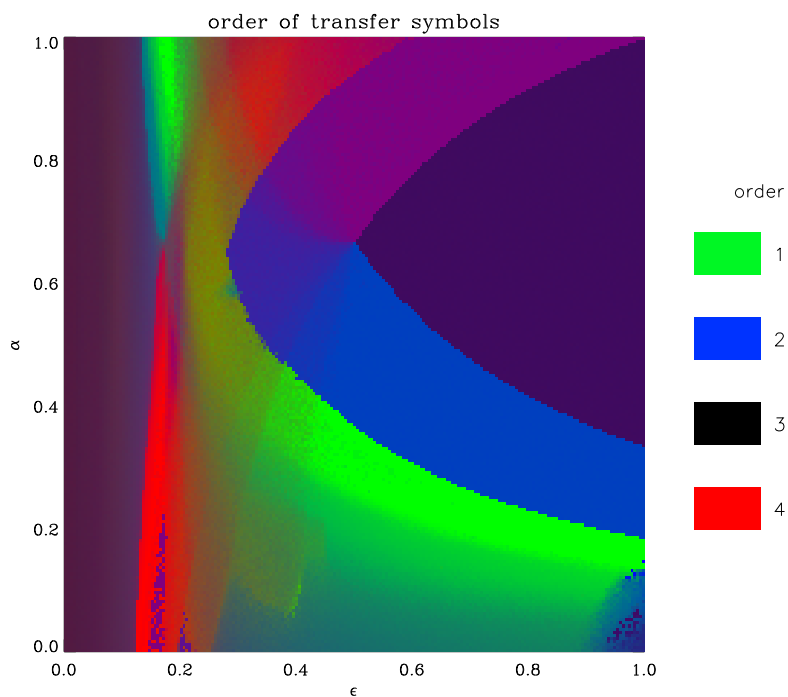


Fig. 4.10: Algebraic order of transfer symbols between neighboring cells (sequence length $n = 4$, from a sample of 100 iterations after an initial period of 10^5 , to avoid transient behavior). The order distribution (over the full lattice) is encoded in the RGB channels of the image (red=4, green=1, blue=2).

In fig. 4.10, the order distribution is encoded in the RGB channels of the image (red = 4, green = 1, blue = 2). Note that, since the distribution is normalized, the last order density is redundant. Also note that this mapping only partially uses the available colors, namely the *simplex* that is the convex hull of the colors *red*, *green*, *blue* and *black*, which covers less than half of the color space. When comparing the result to the map drawn in section 4.2.2 (fig. 4.6b), most of the regions can be discriminated by the distribution of the algebraic order.

Fig. 4.11 shows system states for different coupling parameters as a scatterplot. The different graphs can be considered as 2-dimensional projections of one scatterplot, drawn in the affine vector space spanned by the orders 1 to 4. The main regimes are color coded in the same scheme as in fig. 4.6b.

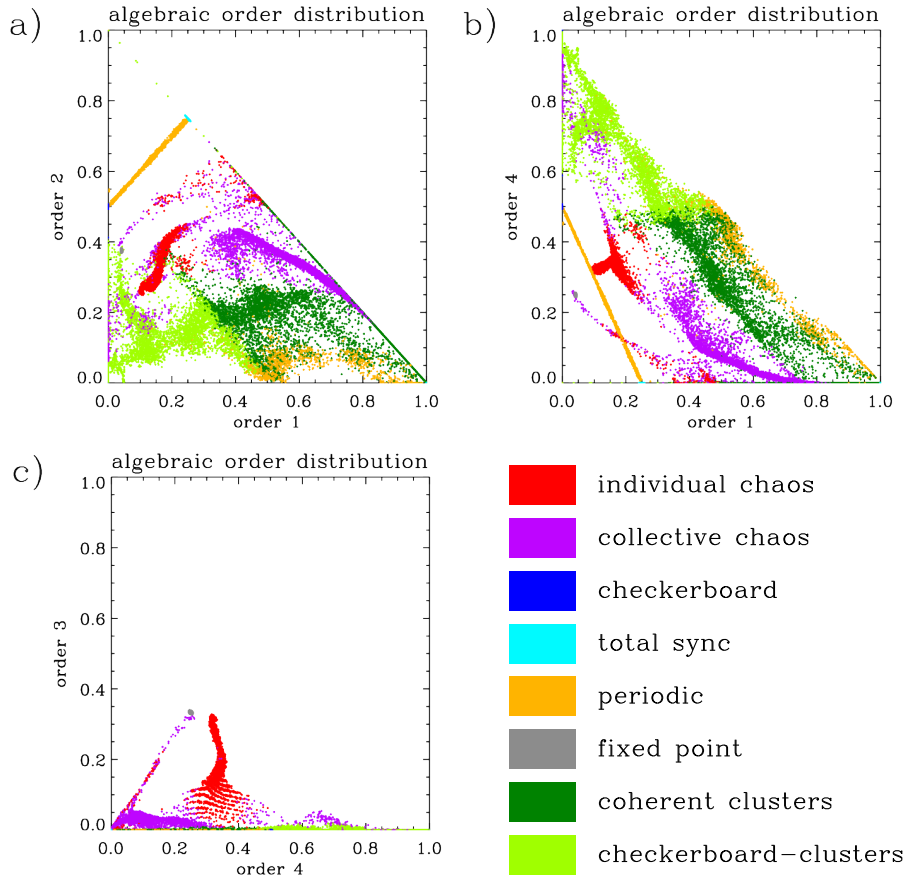


Fig. 4.11: Distribution of the algebraic order of transfer symbols, for the converged system (from a sample of 100 time steps after an initial run of 10^5 iterations, sequence length $n = 4$). a) Order 1 vs 2. b) Order 1 vs 4. c) Order 4 vs 3.

Altogether, the populations corresponding to the different regimes are spread out as distinct clouds of points. The regimes are separated well, and most intersections that are present in the 2-dimensional figures are resolved in the 4-dimensional space. Note for instance, in fig. 4.11a and b, that the chaotic regimes are separated from the rest in the order-3 dimension. Parts of the periodic regime (yellow) have a similar symbolic signature as the coherent clusters regime. There is no continuous transition between these two yellow groups, suggesting that the symbolic description has an abrupt transition, which does not exactly coincide with the onset of periodicity. This is probably related to longer periods, which do not lead to ambiguities in symbols of short sequence length.

As expected, the fixed point is represented by a cloud of points around a unique distribution. Most of the periodic regime spans a straight line between its two extreme configurations, namely checkerboard patterns and total synchronization. This is a linear transition, because there is a unique distribution for synchronous and opposing pairs of period-2 cells, respectively (see section 4.3.2 for details). A qualitatively similar but more noisy transition can be seen between the corresponding non-periodic regimes, ranging from positive to negative neighbor correlation (dark/light green). In conclusion, the space provides considerable information to distinguish the prominent regimes.

4.3.2 Prototypical Symbol Distributions

This section studies the characteristic symbolic signatures for some of the dynamical regimes of the system. Fig. 4.12 shows typical order distributions for the regimes defined in section 4.2. Some of these distributions can be derived analytically.

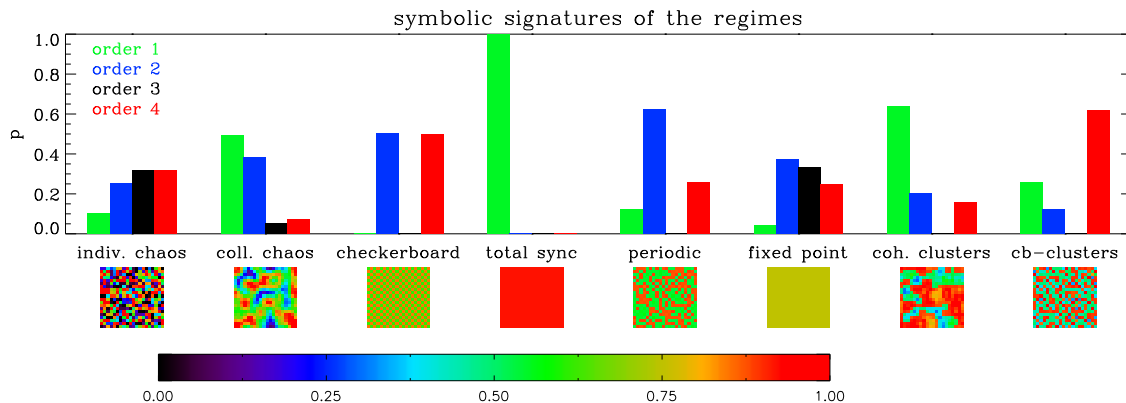


Fig. 4.12: Order distributions for typical representatives of the different regimes (order 1 = green, 2 = blue, 3 = black, 4 = red). As before, ambiguities are resolved by random choice. The color bar refers to the system states drawn below the corresponding order distributions.

Fixed Point

When the time series of each cell is constant, the symbols have the maximum possible ambiguity (any symbol is allowed). Hence, for random choice, the symbol distribution is uniform, and the expected order distribution reflects the number of symbols in each order class. In the parameter space, there exists a well-defined border where the amplitude of the dying oscillation passes the distance threshold of 10^{-6} , at which values are considered as ambiguous. At this border, the order distribution changes discontinuously.

Period-2

In order to understand the resulting symbolic signatures from the period-2 regime, I will start with the simpler cases, first considering the resolution of ambiguities by canonical choice. In the period-2 regime, each pair of cells oscillates either synchronously or anti-synchronously. If a pair of cells oscillates synchronously with period 2, then the state symbols are equal, and the transfer symbol always is the identity. Thus, the signature is 100% order 1. For an non-synchronous (i. e. anti-phase) period-2 pair, the transfer symbol always is (12)(34), leading to a signature of 100% order 2. The order distribution of any spatial configuration is then determined by the relative frequency of synchronous and anti-synchronous pairs.

Now consider the resolution of ambiguities by random choice. For period 2 and sequence length $n = 4$, a delay vector has ambiguities between the 1st and 3rd and between the 2nd and 4th point of each state symbol. The *symmetry group* of the ambiguous delay vector is

$$\{id, (13), (24), (13)(24)\}. \quad (4.16)$$

On the level of state symbols, the resolution by random choice corresponds to the action of a random element r from the above symmetry group on the canonical symbol (from the right,

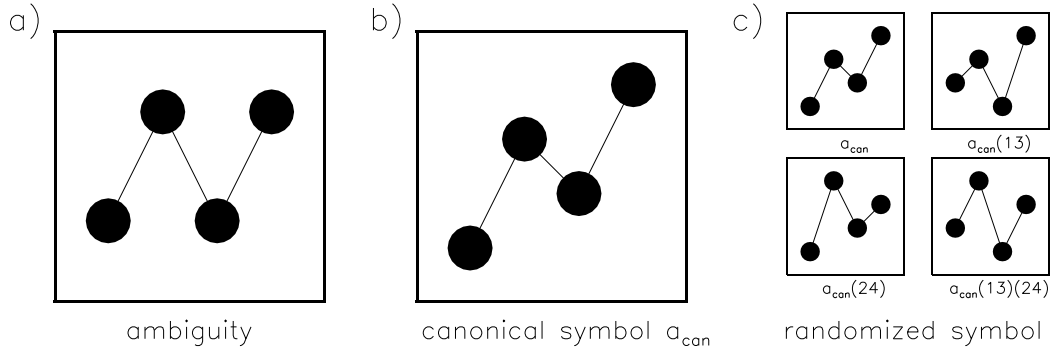


Fig. 4.13: Resolution of ambiguities. a) An ambiguous delay vector. b) The resolution by canonical choice ranks equal values in ascending order, leading to a canonical symbol a_{can} . c) A random choice between the possible resolutions corresponds to the multiplication of a_{can} with a random element from the symmetry group of the ambiguity.

		r_1			
		1	(13)	(24)	(13)(24)
r_2	1	(12)(34)	(1234)	(1432)	(14)(23)
	(13)	(1432)	(14)(23)	(12)(34)	(1432)
	(24)	(1234)	(12)(34)	(14)(23)	(1234)
	(13)(24)	(14)(23)	(1432)	(1234)	(12)(34)

Table 4.1: The possibilities for a random choice transfer symbol $t_{\text{rnd}} = r_1^{-1} t_{\text{can}} r_2$, for $t_{\text{can}} = (12)(34)$.

i. e. acting on the columns). Fig. 4.13 shows the involved symbols. In the case of a transfer symbol,

$$t_{\text{can}} = a_{\text{can}}^{-1} b_{\text{can}}, \quad (4.17)$$

two such elements (independently chosen) end up at both sides of the canonical transfer symbol:

$$t_{\text{rnd}} = (a_{\text{can}} r_1)^{-1} b_{\text{can}} r_2 = r_1^{-1} t_{\text{can}} r_2. \quad (4.18)$$

In the case of a synchronous pair, the result from canonical choice was the identity. For random choice, two (independently chosen) permutations as above are applied. This leads to 25% order 1 and 75% order 2, matching the results from the simulation (compare the 'total sync' regime in fig. 4.11). Note that the example for total synchronization in fig. 4.12 is not taken from the period-2 regime.

For an anti-phase pair, the canonical transfer symbol is $t_{\text{can}} = (12)(34)$. Table 4.1 shows the possibilities for t_{rnd} . This leads to an order distribution of 50% order 2 and 50% order 4, again matching the observed results (see the checkerboard regime in fig. 4.12). Also note fig. 4.11, where most of the periodic regime is on the line spanned by the total synchronization and the checkerboard regime.

Alternating

Now I will consider alternating behavior that is not period-2. Near the periodic region, let us suppose that there is a distinctive period-4 component, in the sense that any of the former ambiguities (from the period-2 case) are resolved in the same way if they are a multiple of 4

points apart. In the case of synchronous dynamics, it seems plausible that both time series have the same phase in the period-4 rhythm, i. e. have the same state symbols (hence 100% order 1 transfer symbols). This matches the observations in the area below the period-2 region, where the total synchronization regime passes to the coherent clusters regime (see fig. 4.10).

In the case of non-synchronous pairs, still assuming a distinct period-4 component, each cell can only be one step before or after its anticorrelated neighbor in the period-4 rhythm. In both cases, the transfer symbol is a 4-cycle, leading to a signature of 100% order 4, in agreement with the simulation results. Note that the period-4 rhythm is not assumed to be stable as long as changes in rhythm are not too frequent.

For the alternating behavior, the agreement between these theoretical considerations and the numerical simulations is seen most clearly in fig. 4.15a, which visualizes the symbolic signature along the transition between the two extremes considered here.

Uncoupled

In the uncoupled system ($\epsilon = 0$), the time series of different cells are necessarily independent. Hence, the state symbols at a fixed time are iid, with a distribution that is characteristic for the chaotic logistic map. This determines the transfer symbol distribution and therefore explains the order distribution.

Extreme Coupling

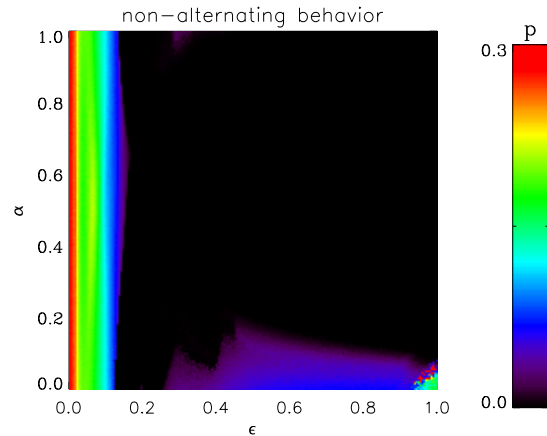
In the extreme-coupling case $\epsilon = 1$, the system splits into two subsystems (see section 4.2.3), both of which have chaotic dynamics. Neighboring cells always belong to different subsystems. Furthermore, the correspondence (which cell belongs to which subsystem) changes every time step. This means that each time series – and, as a consequence, each state symbol – contains information from both subsystems. Under these circumstances, the symbolic signature is probably dominated by the random relations between the independent subsystems. I conclude that this regime calls for a description that treats the subsystems separately, therefore transfer symbols are not a favorable method.

4.3.3 Forbidden Symbols and Suppressed Classes

The symbols of length 4 reveal an interesting example of forbidden symbols (see Amigó [4]). Symbols of order 3 only appear in the weakly coupled region on the left, and of course in the fixed point region where the symbols are determined purely by the random choice mechanism for resolving ambiguities.

Behavior that alternates between above and below the fixed point at 0.75 is frequently observed. In a symbolic description of sequence length 3, this alternating behavior can be expressed as a restriction of the set of state symbols. Violations of this restriction are seen as occurrences of the 'forbidden' state symbols [012] or [210]. Fig. 4.14 shows the frequency of those forbidden symbols, which (like in the case of a single logistic map) is strongly correlated to a positive MLE of the system (compare to fig. 4.5).

Fig. 4.14: Non-alternating behavior: relative frequency of the state symbols [012] and [210], in the long term behavior after an initial period of 10^5 steps. Constant time series are shown in black since the question for alternation needs pairwise different values.



4.3.4 Transitions Between Dynamical Regimes

Transitions of the system are examined by evaluating the transfer symbol distribution along a path in the parameter space. The measures used in this section are the order distribution of transfer symbols (over all pairs of neighboring cells, over 100 time steps), and the state of the system. As before, all samples are taken after an initial period of 10^5 time steps, in order to examine the long term behavior.

In the non-periodic regimes, I observed a smooth transition from the checkerboard configuration (anti-phase neighbors) to localized clusters of in-phase neighbors (fig. 4.15a), leading to a configuration where the whole lattice is totally synchronized. Note however, that the symbols used here can not distinguish between total synchronization and phase synchronization with fluctuating amplitudes. In the middle of the transition, the spatial configuration fluctuates over time, allowing order-2 symbols to appear.

A similar transition was found in the period-2 regime. The mechanism behind these transitions is that pairs of in-phase (respectively anti-phase) neighbors have a characteristic distribution. Therefore, the overall distribution is linear with respect to the ratio of in/anti phase pairs of neighboring cells in the lattice (as explained in section 4.3.2).

In fig. 4.15b, a path from the fixed point to the collective chaos regime is examined. The fixed point has a unique order distribution, which jumps to the symbolic signature of period-2 total synchronization (see again section 4.3.2 for details about those distributions). Outside the period-2 regime, total synchronization is represented by 100% order-1 symbols, and there is a smooth transition to collective chaos.

Fig. 4.15c/d show a path along the lower border ($\alpha = 0$) of the parameter space. Starting in the individual chaos regime, it passes an ordered window (note the two sorts of checkerboard-like spatial order patterns with different symbolic fingerprints), and ends in the collective chaos regime. The last samples have a symbol pattern coming from two independent chaotic clusters in a checkerboard configuration.

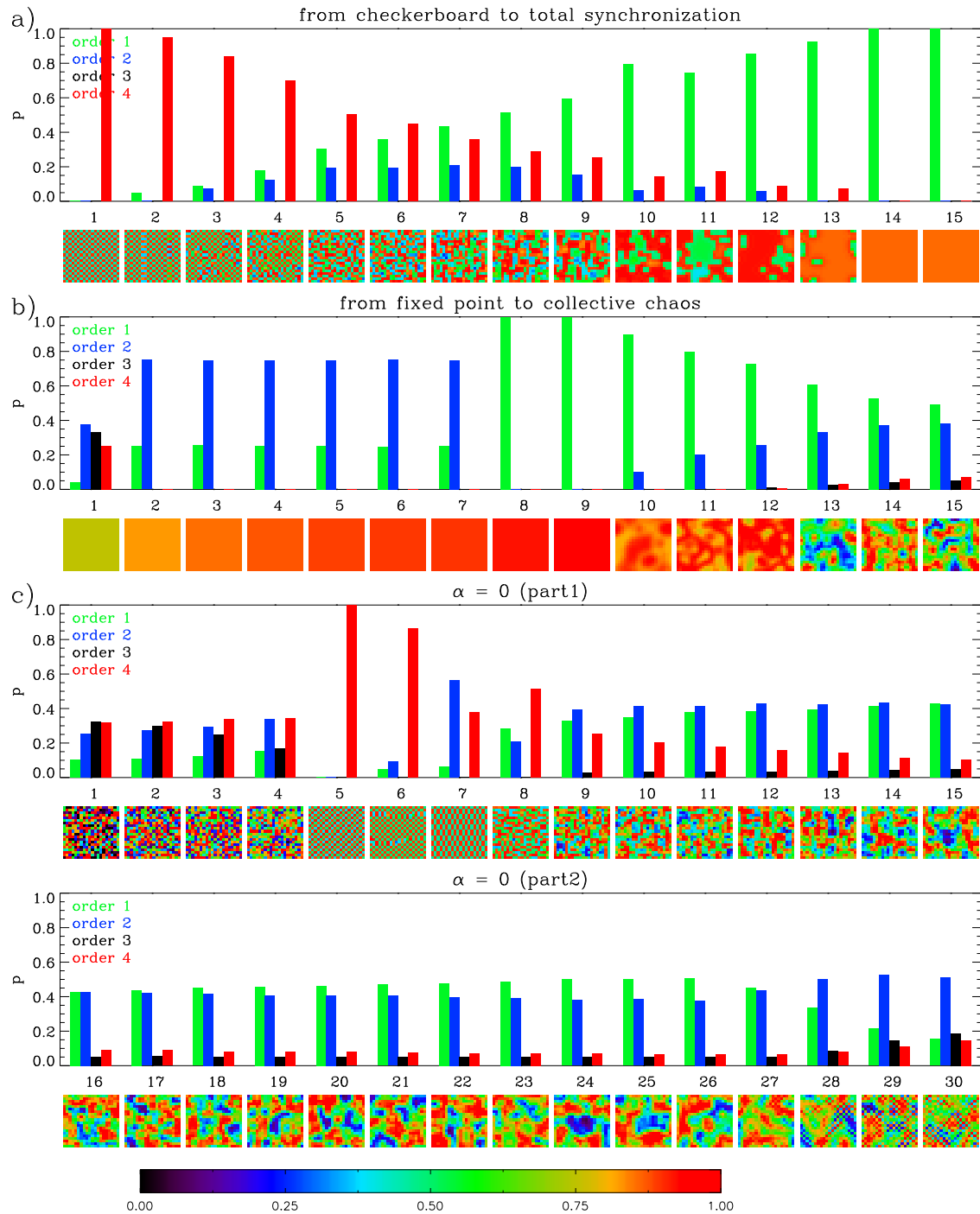


Fig. 4.15: Transitions. Transfer symbol order distribution (green = 1, blue = 2, black = 3, red = 4) and system state (rainbow color table) for samples along a path in the parameter space. a) Non-periodic phase-synchronized configurations from checkerboard (anti-phase neighbors) to total synchronization (in-phase neighbors). b) From total synchronization to collective chaos. c) From individual chaos through a periodic window to collective chaos. The color bar refers to the system states shown below the corresponding order distributions.

4.3.5 Symbolic Complexity Measures

In the collection of measures of order in section 2.3, one of the general terms was complexity. This section will apply some of the concepts introduced there to the symbolic description of the coupled map lattice.

Section 2.3.2 presents a complexity measure for probability distributions, constructed out of an order measure and a disorder measure. I applied the measure to the transfer symbol distribution of neighboring cells. As the order measure, I used the Kullback-Leibler distance between the measured symbol distribution p and a uniform reference distribution p_{ref} . The disorder measure was the entropy of the symbol distribution. This leads to the symbol-based complexity measure

$$c(p) = H(p) d_{\text{KL}}(p, p_{\text{ref}}). \quad (4.19)$$

Fig. 4.16a shows a measure of 'local complexity', where the complexity measure was calculated for each cell separately, and averaged over the lattice. This describes the complexity of a typical pair of neighboring cells. From this perspective, the fixed point is almost simple (the distribution is not exactly uniform because of the low sample size), as is much of the clusters regimes outside of the period-2 region. When entering the period-2 region from the outside, the symbols become ambiguous. Since I resolved ambiguities by random choice (see section 3.1.5), a random element enters the transfer symbols (the resulting distributions are derived in section 4.3.2), and gives the region a large complexity. This seeming burst of complexity is not part of the system but a result of the symbolic description. The transition itself is real however, because the qualitative dynamics change abruptly at the boundary of the period-2 region.

For a model of 'global complexity' (fig. 4.16b), the complexity measure was calculated only once, for the symbol distribution of the whole lattice. This description is sensitive to the spatial diversity among neighbor pairs. In this description, the clusters regimes become complex, reflecting their inhomogeneous spatial structure.

In fig. 4.16c and d, the measure is applied to the algebraic order distribution of transfer symbols. The reference distribution for the order measure is the cardinality of the order classes, i. e. the order distribution that corresponds to a uniform symbol distribution. As expected, the complexity of the fixed point vanishes. There are several regions where the order complexity is lower than the symbol complexity. This suggests that the configuration is complex from a combinatorial but simpler from an algebraic perspective, e. g. because many of the involved symbols have similar algebraic properties.

Amigó et al. [5] propose, as a complexity measure, the number N of different symbols occurring in a symbol sequence. Fig. 4.16e and f show this measure for the transfer symbols of neighboring cells, on the basis of single neighbor pairs and the whole lattice, respectively. In this case, I resolved ambiguities via canonical choice, which is more appropriate for this kind of measure (see section 3.1.5). The local measure is highly similar to the Lyapunov exponent (compare with fig. 4.5a, which is also calculated based on local dynamics). In the clusters regimes, as above, the difference between the local and global measures are due to different kinds of neighbor pairs. In the collective chaos regime, such a distinction between different pairs should not persist in the long run. I conclude that the lower local measure comes from *false forbidden patterns* [5], caused by the limited sample size (100 symbols, compared to $4 \cdot 10^4$ for the global measure). Still, the similarity to the Lyapunov exponent suggests that it might be useful to ignore rare symbols for this measure, which would also result in some robustness

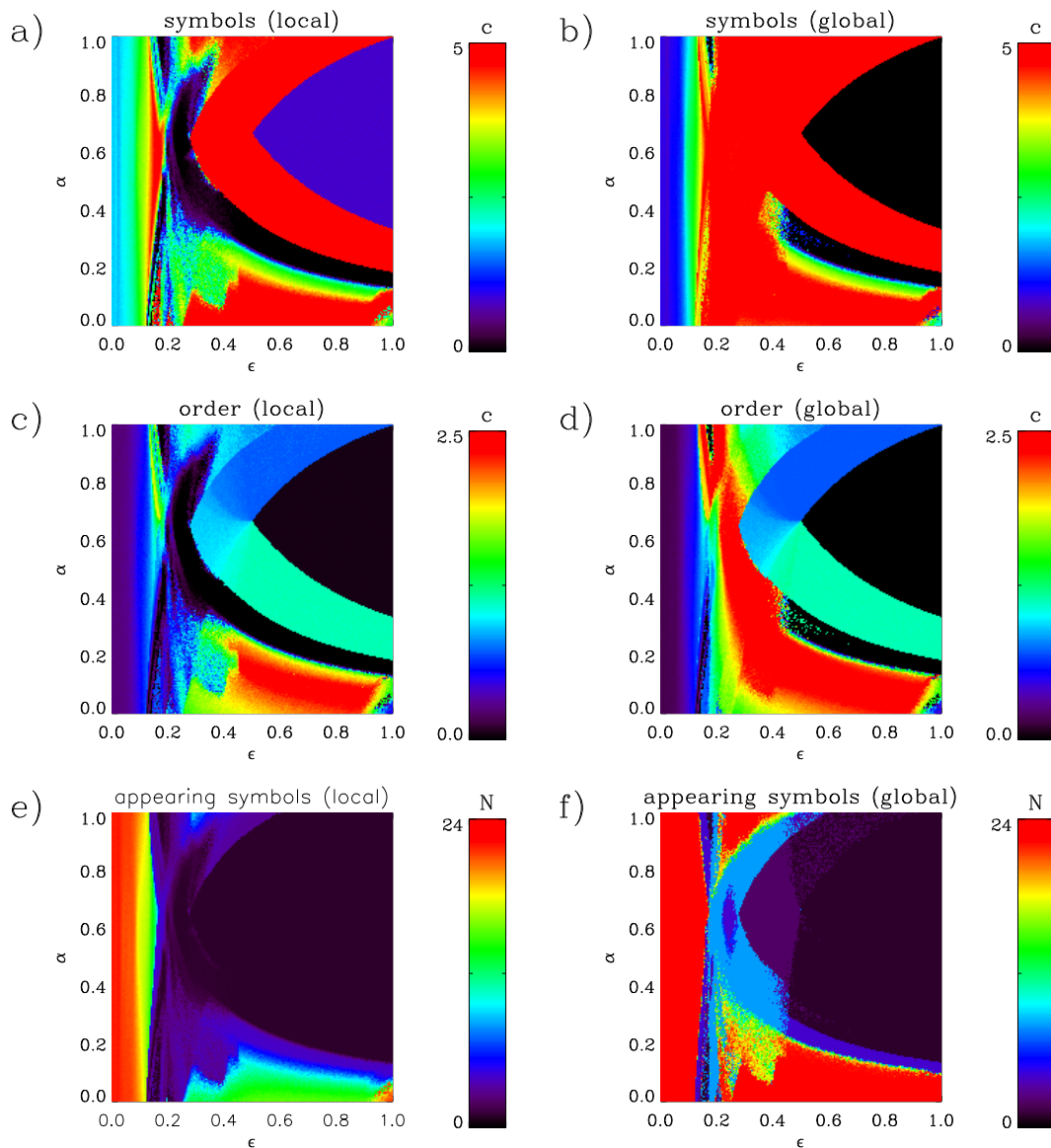


Fig. 4.16: Complexity measures in terms of transfer symbol distributions (sequence length $n = 4$). a) Local complexity (each cell separate) b) Global complexity (symbol distribution over the whole lattice). c) Local complexity of the order distribution d) Global order complexity e) Number of allowed symbols (local) f) Number of allowed symbols (global).

against noise. Especially the dynamics of high-dimensional systems often exhibit characteristics normally typical for a contamination with noise.

In conclusion, different aspects of complexity can be expressed in terms of symbol distributions. Some of the measures have strong filtering properties, concentrating on spatial or temporal order. They distinguish complex relations between neighbors from local structures involving different sorts of (simple) pairs of neighbors. For the measure discussed first, the definition of the reference distribution is not necessarily canonical, but reflects a choice about which sorts of behavior are considered as simple in a specific research context.

4.4 Convergence and Stationarity

One of the main topics in the study of a complex system is its long term behavior. One asks for regularity properties of the long term dynamics, and tries to distinguish them from *transient behavior*.

In physics, a *steady state* of a system is characterized by properties that are constant over time. There is a corresponding term of *stationarity* for random processes, which means that the joint probability distribution of the process is invariant with respect to translations in time (or space, if applicable). In this stochastic sense, stationarity is a prerequisite for the application of many statistical and analytical techniques in the framework of both linear and nonlinear data analysis, e. g. autocorrelation and Lyapunov exponents.

In the context of dynamical systems, stationarity is related to the convergence to an *attractor* (see section 2.1.2). For studying properties of the attractor using a trajectory, it is important to examine the time scale of this convergence (called *transient time* in the following). This knowledge is necessary, e. g. for studying stability properties (section 4.5), but also for delay-coordinate embedding of the attractor (see section 2.2). Usually the convergence to the attractor is expressed in a metric sense, where – at least for sufficiently small deviations – one expects a roughly exponential decay of the distance to the attractor.

Definition 4.1 (Convergence). *In a metric space (Y, d) , a sequence $f : \mathbb{N} \rightarrow Y$ converges to a limit $l \in Y$ if and only if*

$$\forall \epsilon > 0 \exists t_0 > 0 \text{ such that } d(f(t), l) < \epsilon \quad \forall t > t_0. \quad (4.20)$$

In other words, any ϵ -neighborhood of the limit l contains almost all points of the sequence. In most real-life cases, one can only expect approximate stationarity, because of asymptotic convergence and the presence of internal and external noise. Furthermore, only finite time series are available in most cases. Therefore, a practical definition of stationarity needs to distinguish between fluctuations of the observable on one side, and movements that are part of the convergence process on the other. The question is, at which time the dynamics of any transient processes have become sufficiently small, that the time series reflects the long term dynamics of the system. In cases where the distance to the attractor can be measured or approximated, the transient time usually refers to the passing below a distance threshold, which is chosen to ensure a sufficient level of stationarity.

Note that a practical concept of stationarity depends on the context, the time scale and the objective of the experiment. As an example, consider the *circadian rhythm* (see also section 4.1.1) of a physiological system, which is coupled to the daylight conditions. It might be stationary on the time scale of a few days, but exhibit strong seasonal trends on the time scale of a year. One investigation might consider these as part of the stationary state, while another one might consider the seasonal dependence as an external perturbation.

For the CML model system, one has to choose an appropriate observable, and define a suitable convergence criterion. Section 4.3 showed that the transfer symbols of neighboring cells allow for a good description of the system's dynamics. Therefore, the convergence process was described primarily in terms of the probability density of the algebraic order of transfer symbols. In contrast to the metric description mentioned above, the discrete symbolic description tends to ignore the asymptotic convergence, and instead indicates if the trajectory possesses the main dynamical properties of the attractor. Consequently, a symbolic description often converges within finite time if the system has an asymptotic convergence. On the other hand,

unlike the metric case, a constant symbolic description does not indicate a fully converged system. There may still be activity left, for example in cases of *intermittency*, where dynamics that are almost constant or periodic are followed by bursts of activity in irregular intervals.

4.4.1 Transient Times

I estimated the transient time for the model system in terms of the symbolic description. In an *ex post* approach, I assumed that after a sufficiently large time t_s all transient processes are terminated. Thus, the following trajectory $x(t)|_{t \in [t_s, t_{\max}]}$ is a typical representative for the long term behavior of the system, which is supposed as stationary. The trajectory $x(t)$ of the system is described by an observable $f(t) \in Y$, where (Y, d) is a convex subset of an affine space, equipped with a distance measure d (only distances and convex combinations are needed). As mentioned, the observable must be chosen in a way that it reflects the objective of the experiment. In the application to the CML system, the observable $f(t)$ was the algebraic order distribution of transfer symbols (sequence length $n = 4$) of neighboring cells, over the whole lattice and $\delta t = 2$ time steps. Hence, the set Y is the space of order distributions, equipped with the Kullback-Leibler distance d_{KL} (defined in section 3.2.3).

I used the end part $x(t)|_{t \in [t_s, t_{\max}]}$ of the trajectory as a training sample. The stationary state was characterized by the mean value f^{mean} of the observable. To decide if a given value of the observable represents a stationary state, I considered the Kullback-Leibler distance between the observable $f(t)$ and its average value f^{mean} in the stationary state. The variation of the stationary state was quantified by the median distance:

$$d_m := \text{median}\{d_{\text{KL}}(f(t), f^{\text{mean}})|t \geq t_s\}. \quad (4.21)$$

The threshold for stationarity was defined in terms of the variation:

$$d_t := \max\{10d_m, 10^{-2}\} \quad (4.22)$$

The lower limit 10^{-2} for the threshold was chosen to give some robustness against sporadic fluctuation in the long term behavior, which might happen outside of the sample for d_m and then would lead to sporadic false long transients. The *transient time* was defined as the time when a moving average of window size 2 passes (and stays below) the threshold d_t . Supposing a roughly exponential convergence, I took samples of $f(t)$ at exponentially increasing distances, with $t_s = 10^5$.

Note that, so far, it was assumed that the system will always eventually reach a stationary state. Dependent on the objective of the experiment, it can be useful to define a stationarity test for the training sample, or to monitor the distance $d(f, f^{\text{mean}})$ for times after the 'calibration sample'. For the measure used here, large fluctuations are allowed in the long term limit, as a result volatile chaotic dynamics are defined as stationary states.

Also note that the approach can not be used in real time while the system is evolving (which would be useful for control purposes), because it calibrates on the end part of the trajectory. Some regimes have a unique long term limit, which can be determined in advance, but in general the long term limit depends on the initial condition.

Fig. 4.17a shows the transient time. As a measure for the fluctuations of the stationary state, fig. 4.17b shows the median d_m . In fig. 4.17c, snapshots of $d_{\text{KL}}(f(t), f^{\text{mean}})$ at different times are displayed. The individual chaos regime at small ϵ has no transient. The variation is moderate in this regime. The symbol distribution is broad, but the cells (and hence the

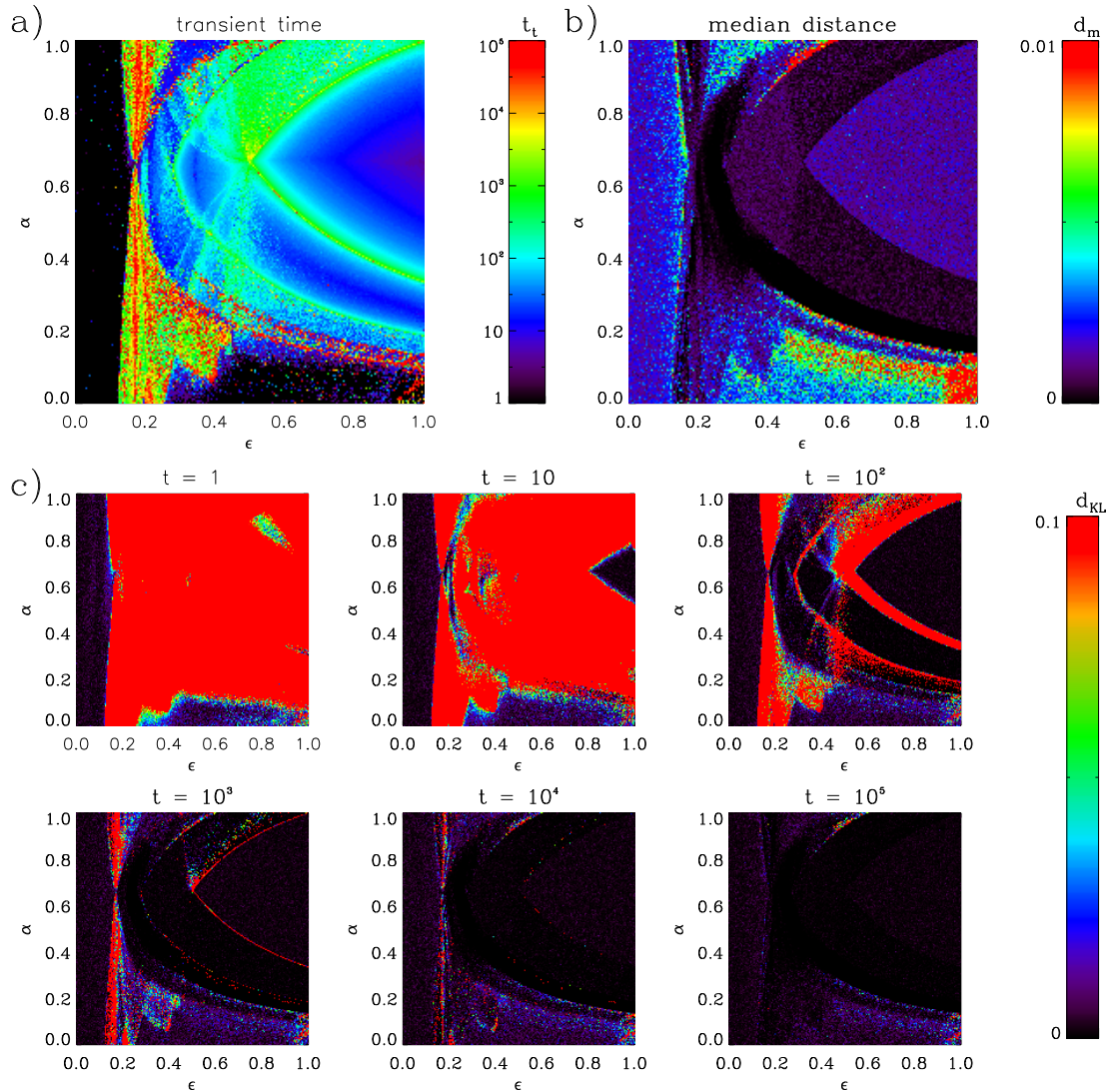


Fig. 4.17: a) Transient time. b) Median distance between $f(t)$ and f^{mean} in the long term limit. c) Distance between $f(t)$ and f^{mean} for specific times.

symbols for different pairs of neighboring cells) are independent, resulting in low statistical fluctuations. The non-zero results for the transient time are caused by statistical errors.

The regime of collective chaos (bottom right) has a higher variation, because the behavior of every cell is correlated to its neighborhood. The longest transients (several 10^4) are found in the clusters regimes, and in the periodic windows around $\epsilon = 0.2$. The periodic regimes for large ϵ have short or medium transients. There is no obvious correlation between the transient time and the amount of variation of the long term limit.

In the period-2 regimes, there are lines of increased transient time, which are similar to the lines where oscillation modes of the fixed point become unstable (fig. 4.8 in section 4.2.4).

4.4.2 Transient Behavior

Transients describe the process of the system settling on its attractor. Keeping the terminology from section 4.4.1, transient behavior is studied in terms of the order diagram introduced in section 4.3.1. The orders 1 and 4 have proven to be a useful representation space for the set of stationary states.

Fig. 4.18 monitors the development of some transients, starting from several random initial conditions for fixed parameter sets. The left column shows the distance between $f(t)$ and f^{mean} , the right column shows the evolution of $f(t)$ in a projection of Y to the plane of algebraic order 4 versus 1. Since the system always starts in a random initial condition, one might expect the starting point of the transients to be independent of the parameters, which is not the case. Since each symbol includes several time steps of data (see section 3.1.6), a symbolic description always carries information on the dynamics, which differ, dependent on the parameters. Furthermore, $\delta t = 2$ time steps of the symbolic description are used, in order to average over the two phases of the common alternating behavior. Hence, the starting point mostly depends on the parameters, with scattering due to the initial condition. In most cases, the choice of initial condition slightly shifts the transient, but has no influence on the overall development.

Fig. 4.18a depicts an example from the periodic regime, where the spatial structure is unordered. The system first goes through an intermediate state, before converging to the final state. Since there are many different stable spatial configurations, the system has multiple attractors. However, the different initial conditions lead to roughly the same order distribution, hence they have similar ratios between in-phase and anti-phase neighbor pairs. In the symbolic description, the transients follow a common corridor. The abrupt drop in distance comes from the discontinuous change of the symbolic description when an oscillation amplitude drops below the threshold for ambiguities (see section 3.1.5). Since symbol-based measures neglect oscillation amplitudes, a linear measure could probably show a more gradual convergence than the symbol-based measure, which tends to jump from the characteristic distribution of the non-ambiguous to the ambiguous state. On the other hand, the discontinuity is not an artifact but reflects a sudden change in the quality of the dynamics.

The fixed point (fig. 4.18b) has a unique final distribution. Even for fixed parameters ($\epsilon = 1, \alpha = 0.8$) the transient paths have a considerable dependence on the initial condition. The transient time mainly depends on the system parameters, ranging from a few steps up to 10^3 . The fixed point is reached mainly by damping of an alternating oscillation. Such a damped alternating oscillation corresponds to the state symbols [4132] and [1423]. If neighbor cells are in the same phase, the transfer symbols are 100% Identity. Dependent on the initial condition, the lattice may not be fully in-phase, and the cells may go through this transitional state at different times, therefore not every initial condition comes close to the distribution with 100% order 1. The path leads through the symbolic signatures of the coherent clusters regime (see fig. 4.11 in section 4.3.1), and depends on the distribution of phases in the intermediate damped alternating oscillation.

Like the fixed point, the stationary state of the (period-2) checkerboard regime (fig. 4.18c) has a strict order resulting in a unique symbol distribution, which is independent of the system parameters and the initial condition. Some longer transients are due to global defects, which take longer to straighten and find a stable configuration. At $t \approx 10 - 100$, there is an intermediate signature with mostly order 2 symbols, caused by damped alternating oscillations. As above, the state symbols of the intermediate state are [4132] and [1423], for anti-phase

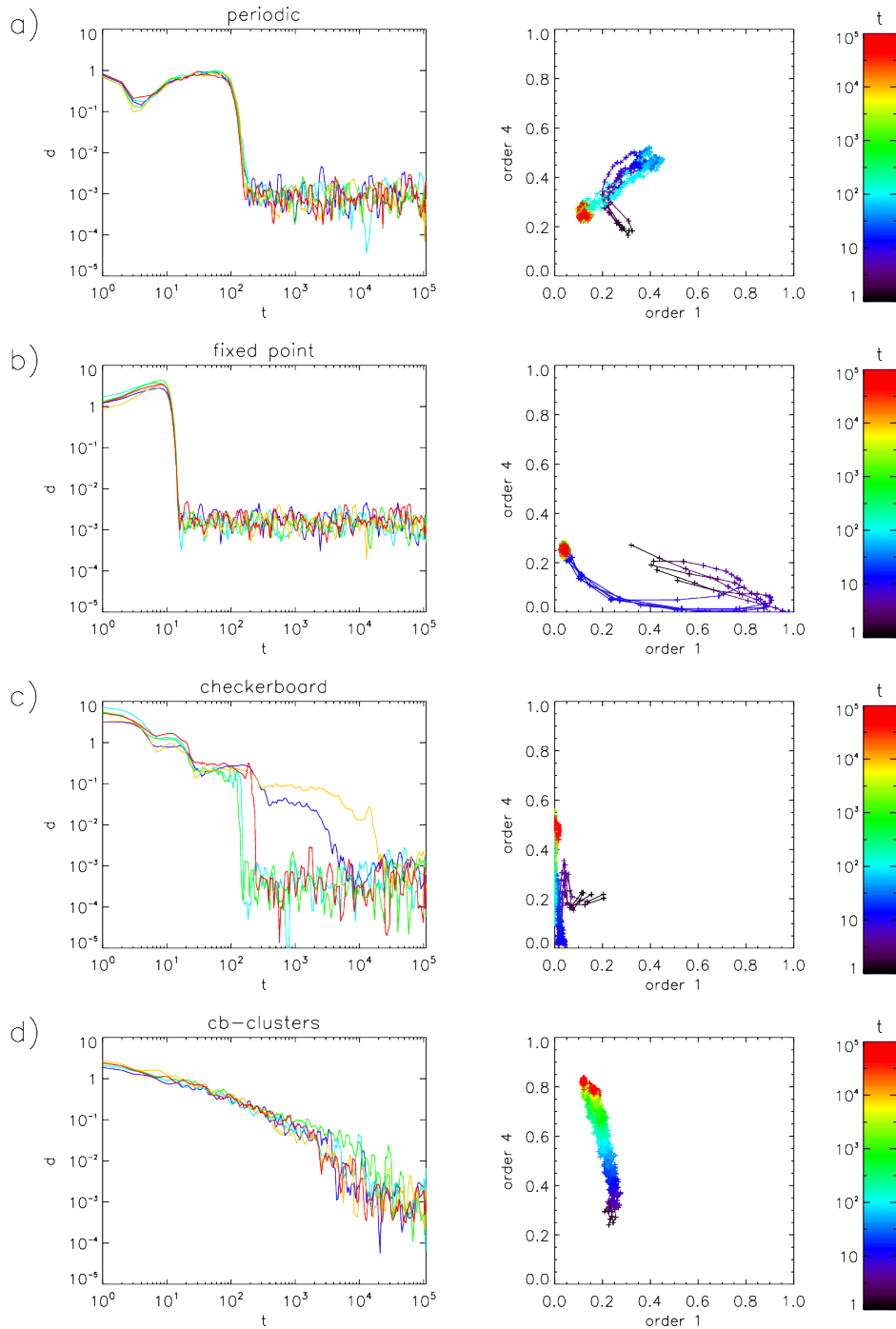


Fig. 4.18: Transient development of a set of 5 random initial conditions for a fixed parameter set. Left: Kullback-Leibler distance between the transfer symbol order distribution of time t and the stationary state. Right: Development of the transfer symbol order distribution. a) $\epsilon = 0.295, \alpha = 0.675$ (periodic). b) $\epsilon = 1, \alpha = 0.8$ (fixed point) c) $\epsilon = 0.82, \alpha = 0.995$ (checkerboard) d) $\epsilon = 0.2, \alpha = 0.2$ (checkerboard-clusters).

neighbors the transfer symbol is always (12)(34), which has order 2.

The clusters regimes (fig. 4.18d) normally display long transients. The variation is relatively small. However, an analysis of the distance $d_{\text{KL}}(f, f^{\text{mean}})$ after the calibration period shows that in some cases it increases again. This suggests, that some of the states are not stationary. There possibly are parameters for which the system performs a random walk, where each cell mainly shows alternating behavior but slowly fluctuates between the two possible phases.

4.5 Stability

The idea of stability is that a small perturbation applied to a system that is in a stationary state does not persistently change its characteristics. Thus, if the system has converged to an attractor, the dynamics are called stable if sufficiently small *perturbations* will not induce a divergence towards a different attractor. The stability of a state can be quantified by the growth rate of perturbations, or by the magnitude of perturbation that is needed to move the system state into the basin of attraction of another attractor. In mechanics for instance, this magnitude is often described in terms of energy as the *potential barrier* around a stable or metastable equilibrium point.

Perturbations can be one-time interventions changing the system's state, as well as temporary or permanent changes of the system mechanics. In the following, the effect of intrinsic and extrinsic perturbations is studied using conventional and symbolic descriptions.

Hereby, different kinds of perturbations are distinguished by three important characteristics. A dynamical system is defined by its state space together with a differential equation or recursion formula describing the development of a state. One can distinguish between an *external* perturbation, which changes the state of the system, and an *internal* perturbation, which changes the system equations, e. g. the coupling parameters. A perturbation is called *local* if it only affects a single part of the system directly (one cell in this case), and *global* if it acts on the whole system. The third property of a perturbation is its time scale, ranging from *one-time* to *persistent* perturbations.

Let $x(t)$ be the state of a system at time t , which is perturbed to a new state $x'(t) := x(t) + \delta x$. The effect of the perturbation can be quantified by monitoring the development of x and x' evolving simultaneously. There are basically two ways to compare x and x' . One is to quantify the growth or decay of their distance with respect to a metric of the state space,

$$d(\tau) := \|x'(\tau) - x(\tau)\|. \quad (4.23)$$

If the state space is (part of) an n -dimensional vector space, the most straightforward metric is the Euclidean distance:

$$d(x, y) := \sqrt{\sum_{i=1}^n (y_i - x_i)^2} \quad \forall x, y \in \mathbb{R}^n. \quad (4.24)$$

This approach describes the prediction accuracy for a future state, and leads to the concept of Lyapunov exponents (see section 4.2.1).

The other possibility is to monitor observables that describe the dynamics of the system. The concept of stationarity was defined in this way in section 4.4. The difference between these descriptions is apparent in the case of a chaotic attractor, which is stable in the second sense (a perturbed state generally returns to the attractor), but not in the first (a chaotic system has a positive Lyapunov exponent).

4.5.1 Global Perturbations

This section studies a global one-time external stimulus acting on a stationary state. Paying attention to the transient time, a random perturbation was added to each cell (iid normally distributed, mean zero, standard deviation $\sigma = 10^{-5}$). Note that the strongest form of this perturbation would make the current state completely random, destroying all information. This is equivalent to a restart of the system with a new random initial condition, hence the transient behavior (see section 4.4) is an extreme case of such a perturbation.

I examined the development of the distance $d(\tau)$. For small perturbations, exponential development is expected, leading to the ansatz

$$\gamma := \frac{\ln \left(\frac{d(t+\tau)}{d(t)} \right)}{\tau} \quad (4.25)$$

as an estimate for the growth of the perturbation, which is connected to the Lyapunov spectrum in the following way:

Remark 4.2. *Consider an infinitesimal random perturbation as a ball-shaped cloud of points in the state space. In different directions, it grows with the corresponding Lyapunov exponent λ_i . In the short term limit $\tau \rightarrow 0$, the expected growth exponent γ is the mean Lyapunov exponent. In the long term limit $\tau \rightarrow \infty$ (as long as the perturbation at time τ still is small), the maximum Lyapunov exponent (MLE) dominates. This fact is used to evaluate the MLE in [112].*

Fig. 4.19a shows γ as a function of the system's parameters. In its positive regime (fig. 4.19b), γ is in good agreement with the maximum Lyapunov exponent (MLE) as shown in fig. 4.5a. At the left border, γ is 0.85, which is a good approximation of the Lyapunov exponent of a single logistic map.

For infinitesimal perturbations Δx , one can assume exponential growth, and the exponent γ is independent of the time scale τ . In practice, for small time scales (e. g. $\tau = 2$ steps), there is considerable statistical noise, and for long time scales saturation effects lower the positive values of γ (within a bounded state space or attractor, a finite perturbation can not grow indefinitely). For intermediate values $\tau \approx 5-15$, γ is independent of τ , hence for this time scale the assumption of exponential growth is justified.

Fig. 4.19d illustrates that the growth exponent γ is a useful complementary measure to the symbolic description. Note that regimes with similar symbol distributions differ in their growth exponent and vice versa, which allows the separation of those regimes that can not be distinguished by their transfer symbol distribution alone.

4.5.2 Propagation of Local Perturbations

Another question of interest is the spatial propagation of perturbations. In order to examine this, only one cell of the system was perturbed (one-time perturbation of 10^{-5}). I studied the spatial spreading of the perturbation in terms of the distance between corresponding cells in the perturbed and unperturbed system.

It should be mentioned that the perturbations of this section are not generic, in the following sense: the global perturbation studied above leads to a state distribution that has a density, which is positive on the whole space. Hence, any set of positive probability has full dimension and positive volume. In contrast, the set of possible 1-cell perturbations is *meager*,

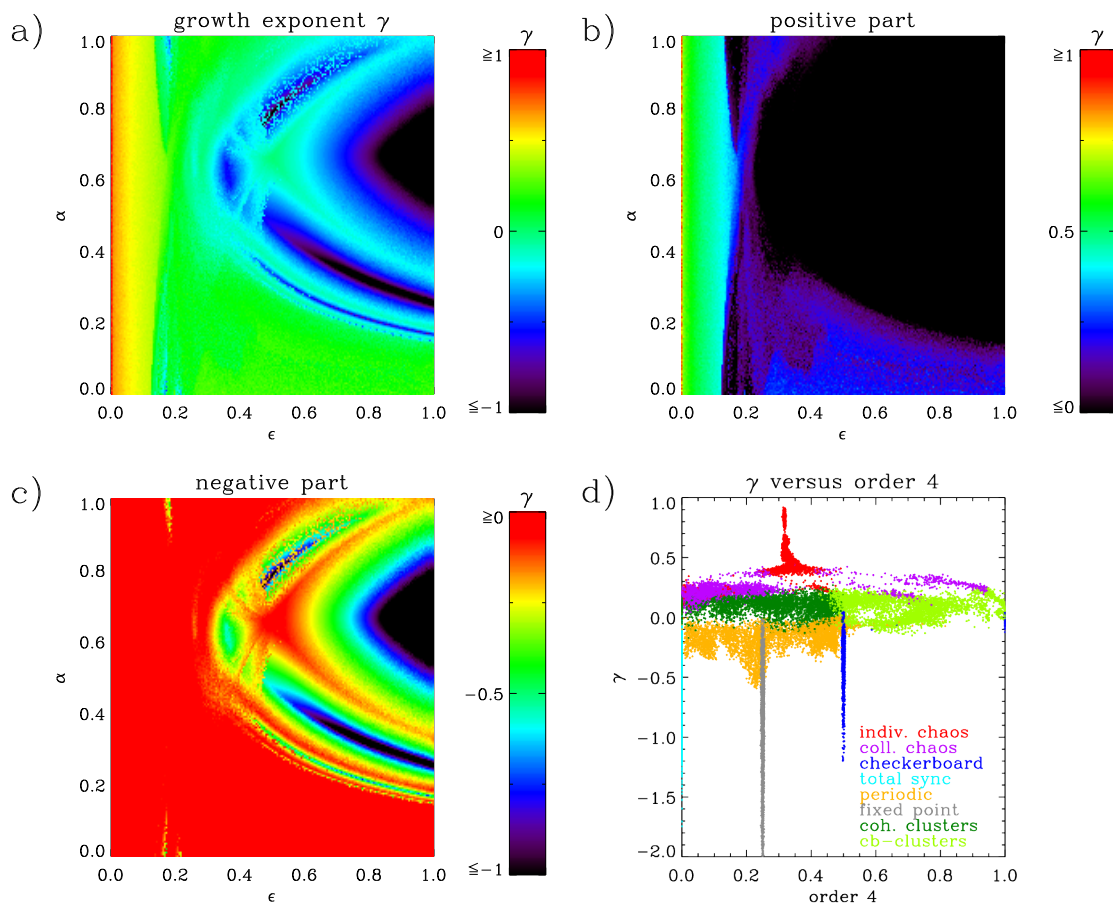


Fig. 4.19: The growth exponent γ for a global one-time external perturbation (iid perturbation with Gaussian distribution, $\sigma = 10^{-5}$, Euclidean distance between perturbed and unperturbed system, $\tau = 10$). a) Full range of γ . b) Positive part of γ (this makes a comparison with the MLE (fig. 4.5a) easier). c) Negative part of γ . d) Relative frequency of order 4 transfer symbols versus the exponent γ (the main regimes are color-coded like in fig. 4.18d).

in the sense that it has dimension 1 (except for the origin, where it is not a manifold) and vanishing volume.

The two chaotic regimes show considerable differences. In the individual chaos (fig. 4.20a), the perturbation expands quickly and regularly. The affected part of the lattice has the form of a *von Neumann neighborhood*, reflecting the coupling geometry (as defined in section 4.1.3). The front of the propagation wave is straight and the propagation speed is uniform. This suggests that the propagation is fast enough that the irregular dynamics in the red area do not influence the dynamics at the wave front considerably. When the perturbation in one cell has grown large enough for saturation effects to set in, the wave front is already too far away to be influenced by them.

In the regime of collective chaos (fig. 4.20b), the development is much more irregular. Due to the strong coupling, I conjecture that at high magnitude the propagation of perturbations from the center can be fast enough to influence the initial wave. When grown to full size

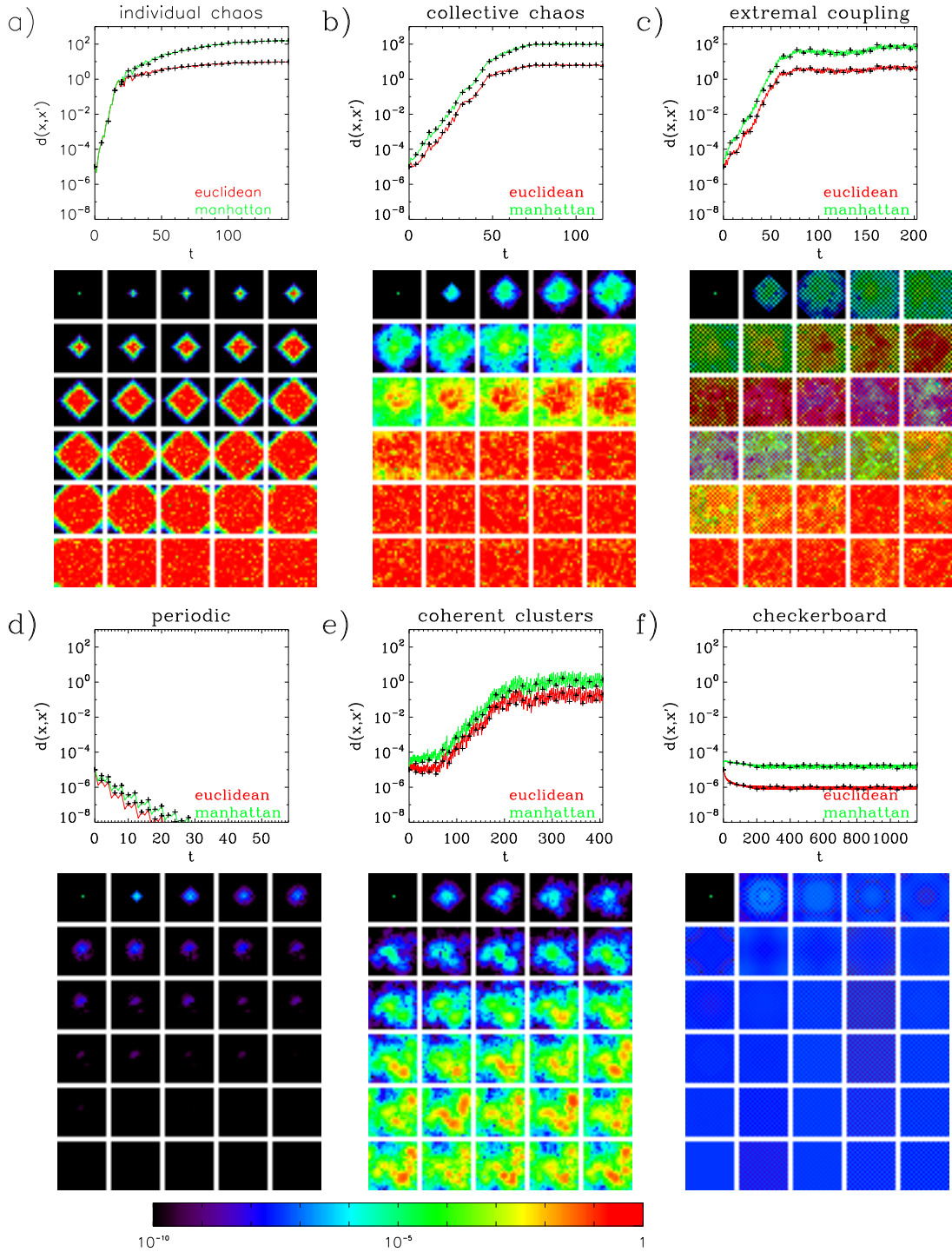


Fig. 4.20: Propagation of local perturbations. Upper panel: Distance between perturbed and unperturbed state, green= L^1 (Manhattan), red = L^2 (Euclidean). Lower panel: Deviation in each cell after a perturbation (the images are read from left to right, top to bottom, log-scaled, time scale is identical to the corresponding distance graph below). a) Individual chaos ($\epsilon = 0.005, \alpha = 0$). b) Collective chaos ($\epsilon = 0.5, \alpha = 0$). c) Extremal coupling ($\epsilon = 1, \alpha = 0.05$). d) Periodic ($\epsilon = 0.375, \alpha = 0.425$). e) Coherent clusters ($\epsilon = 0.375, \alpha = 0.355$). f) Non-periodic checkerboard ($\epsilon = 0.6, \alpha = 1$). Note that the time scales of the diagrams differ, corresponding to the time scales of the observed phenomena.

(in the order of the state space $[0, 1]$), perturbations behave irregularly and cause the initial uniformity to quickly break down.

Fig. 4.20c shows an example of an extremal parameter set ($\epsilon = 1, \alpha = 0.05$), where the future state of a cell depends only on its neighbors and not on its current state. Section 4.2.3 explained that this causes the system to split into two uncoupled components, which are distributed in a checkerboard pattern. Within an exact analytical calculation, a perturbation of one component can not affect the other. However, this is not necessarily the case in a numerical simulation.

In the numerical system, as expected, the perturbation spreads over one component of the system. However, after about 100 iterations, it influences the second component. The reason for this 'forbidden' behavior is in the implementation of the system, which means the design of the algorithmic solution, including the order in which certain operations are done. In the implementation used here, the components are connected by a coupling force, which only adds up to zero in an exact calculation. In the numerical simulation, it can deviate because of roundoff errors.

In conclusion, this example displays the effect of a perturbation in the order of the calculating accuracy (about 10^{-15} for double precision arithmetic). This gives an idea of the coherence time between different algorithmic implementations of the same numerical problem (about 100 iterations in this case). Finally, this is a manifestation of the strong dependence of chaotic systems on initial conditions.

Fig. 4.20d shows an example from the periodic region ($\epsilon = 0.375, \alpha = 0.425$). The exponential decay is faster than the spatial propagation over the lattice.

Fig. 4.20e shows stable coherent clusters ($\epsilon = 0.375, \alpha = 0.355$), where a perturbation grows, but saturates without any cell switching its phase. The Euclidean distance starts at 10^{-12} and reaches an equilibrium at 10^{-1} . This leads to the conclusion that the macroscopic order is stable, while the behavior on smaller scales is complex and still has many degrees of freedom.

Fig. 4.20f shows a checkerboard structure ($\epsilon = 0.6, \alpha = 1$). Like in the previous example, the perturbation does not change the macroscopic order. On a smaller scale, each cell keeps a distance of about 10^{-8} with respect to the unperturbed system, again illustrating the degrees of freedom remaining in spite of the macroscopic order.

Influence of Coupling Parameters

Within the study of a local (one-time external) stimulus, I studied the localization of the evolving perturbation. The idea is to classify the evolution of a perturbation on the scale between *individual* and *collective* behavior. Individual behavior means that a perturbation only affects a small neighborhood. In the collective case, it is uniformly distributed across the lattice, which collectively finds back into the common rhythm. Different parameter sets were used that lead to similar stationary states, in order to study the influence of the coupling parameters on the localization. To quantify localization features, a L^1 (Manhattan) and a L^2

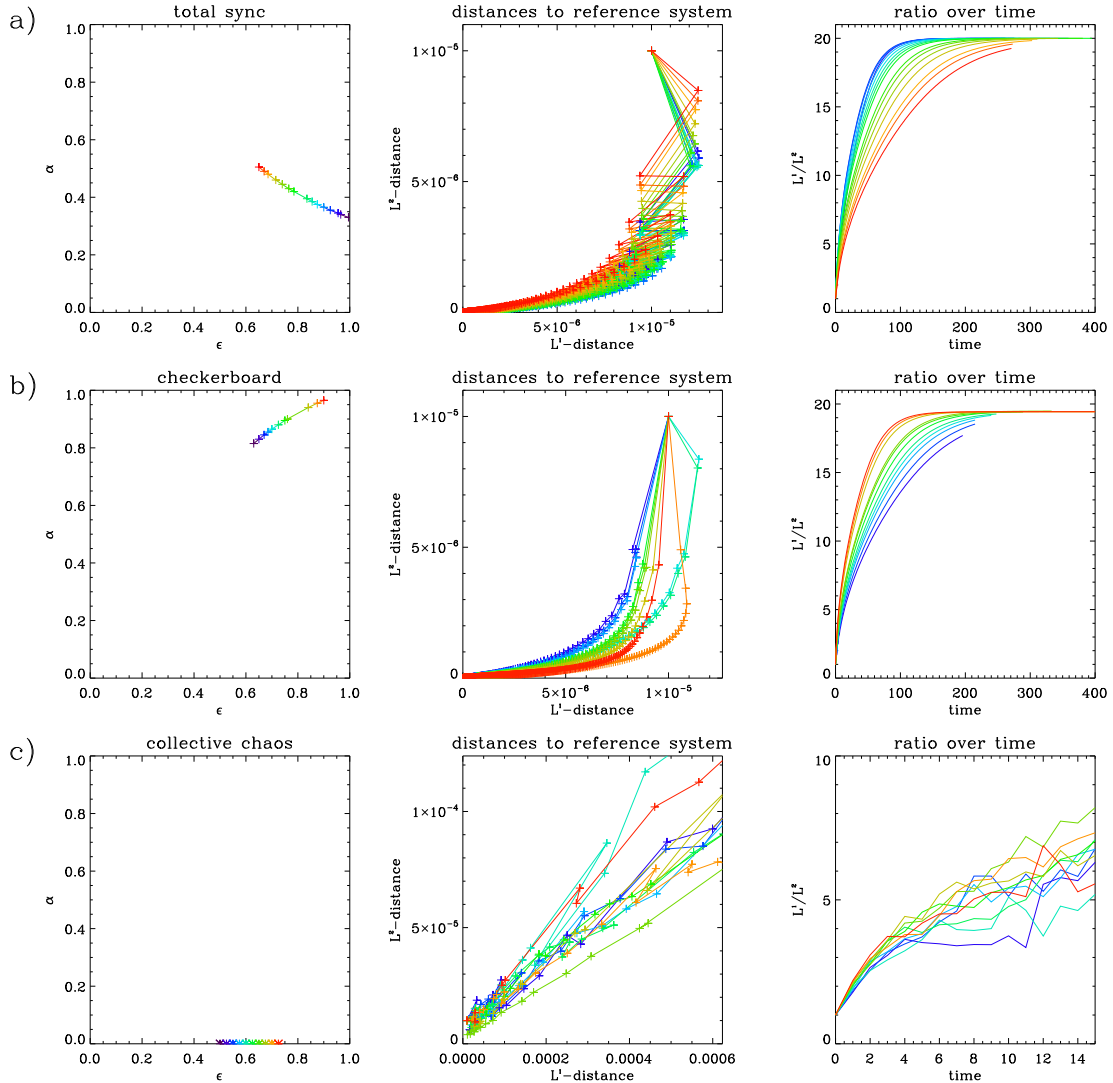


Fig. 4.21: Distance between perturbed and unperturbed system for different parameters that correspond to the same stationary state. Left column: Path in the parameter space (this defines the colors for the other diagrams). Middle column: L^2 (Euclidean) versus L^1 (Manhattan) distance. Right column: Ratio r over time. Rows from top to bottom: a) Periodic total synchronization. b) Periodic checkerboard regime. c) Collective chaos regime.

(Euclidean) distance measure was used,

$$d_{L^1}(x, x') = \sum_{i=1}^n |x'_i - x_i| \quad (4.26)$$

$$d_{L^2}(x, x') = \sqrt{\sum_{i=1}^n (x'_i - x_i)^2}, \quad (4.27)$$

which both measure magnitude, but respond differently to the spatial distribution of a perturbation. While the the L^1 measure counts the total amount of displacement, the L^2 measure assigns less weight to a spatially distributed perturbation. Hence, the ratio

$$r := L^1/L^2 \in [1, \sqrt{n}] \quad (4.28)$$

is a measure for the amount of localization. It reaches from 1 (for a concentration of the perturbation to a single cell) to \sqrt{k} (for a uniform distribution among k cells).

Fig. 4.21 compares the evolution of these measures for three different paths through the parameter space, where the parameter sets of each path correspond to a certain stationary state. Like in the first part of this section, I added a one-time stimulus of 10^{-5} to one cell, and monitored the development of the perturbed system $x'(t)$ with respect to $x(t)$.

The first two paths (fig. 4.21a and b) are associated with the spatially ordered periodic regimes (total synchronization and checkerboard structures, respectively, with fixed amplitude (period-2 oscillation with minimum 0.7 for path *a* and 0.65 for path *b*). In both examples, stronger coupling favors spatial spreading of the perturbation, while for lower coupling the evolution is more localized. Opposing correlations to α were observed for the two paths. This leads to the conclusion that in this regime the localization behavior predominantly depends on the coupling strength ϵ . Weak coupling corresponds to individual and strong coupling to collective behavior. Note that the alternating behavior in the middle diagram of fig. 4.21a is caused by the period-2 dynamics. In the checkerboard regime, the presence of two coexisting clusters of same size and opposite phase compensates this oscillation effect.

In the collective chaos regime (fig. 4.21c), the same correlation of collective behavior and stronger coupling was observed for short time scales (single time steps). For longer time scales, chaotic fluctuations dominate.

4.5.3 Perturbations of the Coupling Parameters

In many real world complex systems, the parameters can hardly be kept constant, but are subject to fluctuations, normally induced by the environment. Such a situation can be described as a perturbation acting on the system's control parameters. Here, the control parameters are modeled as

$$\alpha(t) = \alpha + \delta\alpha(t) \quad (4.29)$$

$$\epsilon(t) = \epsilon + \delta\epsilon(t), \quad (4.30)$$

where $\delta\alpha$ and $\delta\epsilon$ are iid normally distributed random variables (mean 0, standard deviation 0.01). Starting from a random initial condition and after an initial run of 10^5 iterations, I calculated transfer symbols of neighboring cells (sequence length $n = 4$, sample size $\delta t = 50$ iterations).

When comparing the results (fig. 4.22b) to the unperturbed system (fig. 4.22a), the most apparent change is the disappearing of the period-2 regime (blue/purple). The spatial order in this region remains the same, i. e. a fixed spatial configuration of the two phases. However, since the global average depends on the parameters, a parameter fluctuation leads to time-dependent but spatially homogeneous fluctuations in the system. These fluctuations exceed the distance threshold for ambiguities (10^{-3} vs 10^{-6}). For the symbolic description, the effect is similar to a different mechanism for resolving ambiguities: choose randomly, but make the same choice for all ambiguities occurring at the same pair of times.

Apart from the vanishing period-2 regime, fig. 4.22b shows no fundamental changes in the dynamics of the system. I conclude that the rest of the dynamics is stable with respect to noise in the coupling parameters.

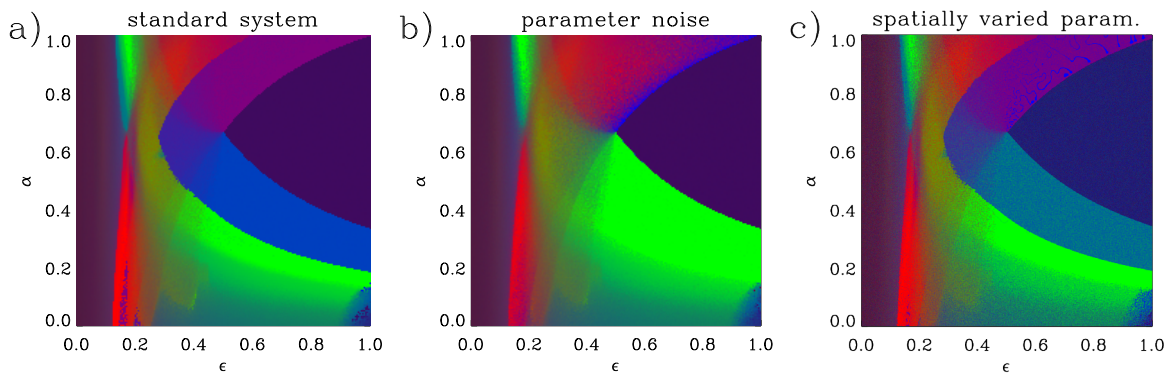


Fig. 4.22: Transfer symbols of neighboring cells (sequence length 4, statistic over 100 time steps), the order distribution is encoded in the RGB channels (red=4, green=1, blue=2): a) Unperturbed system. b) Perturbed system: the control parameters α and ϵ are contaminated by iid normally distributed noise (independently for each time step) with mean 0 and variance 0.01. c) The spatially varied system (4000×4000 cells, symbols of 8 iterations after an initial period of 10^4 steps).

4.5.4 Model System with Continuously Varying Parameters

Here, I want to present an alternative approach to parameter variation, which studies a system with control parameters that are constant in time, but vary in space. The cells were coupled in a two dimensional square lattice, and the coupling parameters for each neighboring pair of cells were dependent on its position in the lattice. The coupling strength ϵ and the delay α both ranged from 0 to 1, reproducing the geometry of the parameter space.

Since opposite boundaries now have different properties, the toroidal topology used so far is not suitable for this model. Therefore, open boundary conditions must be used, where the total coupling strength is distributed among less than four neighbors at the boundary.

For a huge lattice size (4000×4000 in this case), the parameter variation from a cell to its neighbors is small. If monitoring a small neighborhood within the lattice, one would expect it to behave like a small lattice with constant control parameters. This lattice is coupled to other lattices with different parameters, which act as external noise. Hence, a comparison of the spatially varied system to a set of isolated systems is another way to investigate the stability with respect to different control parameters.

Fig. 4.22c shows the transfer symbol distribution for pairs of neighboring cells as a function of the parameters. The diagram shares all major features with the original system (fig. 4.22a), which indicates that the general behavior is robust with respect to influences from neighboring regimes. As expected, the ordered regions (e. g. the fixed point) become slightly smaller, because noise from outside needs some buffer to be damped out. Above the fixed point, the checkerboard pattern is locally stable, while globally large clusters of the two possible phases coexist. Ambiguities are highly sensitive to perturbations, accordingly the distributions in the fixed point and periodic regions change slightly.

4.6 Predicting the Long-Term Behavior

Major parts of technology are based on our ability to predict the future behavior of a system given its present condition. Predictions are studied in a wide range of disciplines, from everyday examples like weather forecasts to the choice of medical treatments or the design of machines. Furthermore, making and verifying predictions is an important selection mechanism for competing scientific theories.

For the CML model, one would like to make predictions in several ways. The most straightforward approach is to predict the system state. This is generally not realistic, at least for regimes with positive Lyapunov exponents. However, not unlike to the case of the weather forecast, one is usually interested in certain dynamical characteristics of the system, which do not require full knowledge about the system state. For the CML model system, such characteristics are its symbolic description or the dynamical regime (as defined in section 4.2.2). Even though not literally a prediction, parameter estimation (from a given trajectory) is a closely related problem.

Section 4.4 showed that, for fixed parameter values, the transients corresponding to different initial conditions quickly converge to a common path (at least in the symbolic description). This suggests that the dynamics of this early non-stationary state is determined mainly by the parameters of the system. Hence, it is likely that a prediction of the long-term behavior of the system can be made given only the early state.

In this section, I present an approach using a variant of the method proposed by Sugihara and May [101], which I will briefly introduce. I used the order distribution of transfer symbols as a descriptor (with the terms from section 4.4), while they use a delay-coordinate embedding. The initial behavior was characterized by the order distribution $f(t_0) \in Y$ over the whole lattice at time t_0 . I used the order distribution $f(t_s)$ over the interval $t \in [100000, 110000]$ to characterize the long term dynamics, like in the definition of the transient time (section 4.4).

The test sample for the approach consisted of one trajectory $x'(t)$ (with random initial conditions and supposedly unknown parameters), where $f'(t_0)$ was used to make an estimate for $f'(t_1)$. The training sample consisted of the order distributions of the other $4 \cdot 10^4$ trajectories (the parameters ϵ and α varying in steps of 0.005), at times t_0 and t_1 . I considered the nearest neighbors of $f'(t_0)$ in the set of all the $f(t_0)$. Sugihara and May suggest that $f'(t_0)$ should lie inside the convex hull of its nearest neighbors (this was not tested here). The estimate for $f'(t_1)$ was defined as an average of the final state of the nearest neighbors, giving exponential weight to their original distances to $f'(t_0)$.

I evaluated the prediction in terms of the Kullback-Leibler distance between the order distribution of the the predicted and the real stationary state (see fig. 4.23). Fig. 4.23f shows the prediction error given a state in the long term dynamics, providing a lower bound for

the prediction accuracy. The remaining errors are caused by the fluctuations in the long term behavior, and by the prediction algorithm. In most cases, the knowledge of the first 1000 steps is enough to get near the accuracy bound.

In the clusters regimes, where long transients are common (see fig. 4.17), a good prediction is most useful. In these regions, the approximate long term development is clear after the first few iterations. In conclusion, in these cases the transient process takes much time but happens in a way that is regular in terms of the symbolic description.

Note that a stationary state at time t_0 is not sufficient for a good prediction. If other trajectories are in the same state at time t_0 but change their dynamics later, they will also influence the prediction for the stationary state. Therefore, the precondition for a good prediction is not stationarity of the trajectory in question, but the separation (in terms of the symbolic description) of trajectories with differing long term behavior.

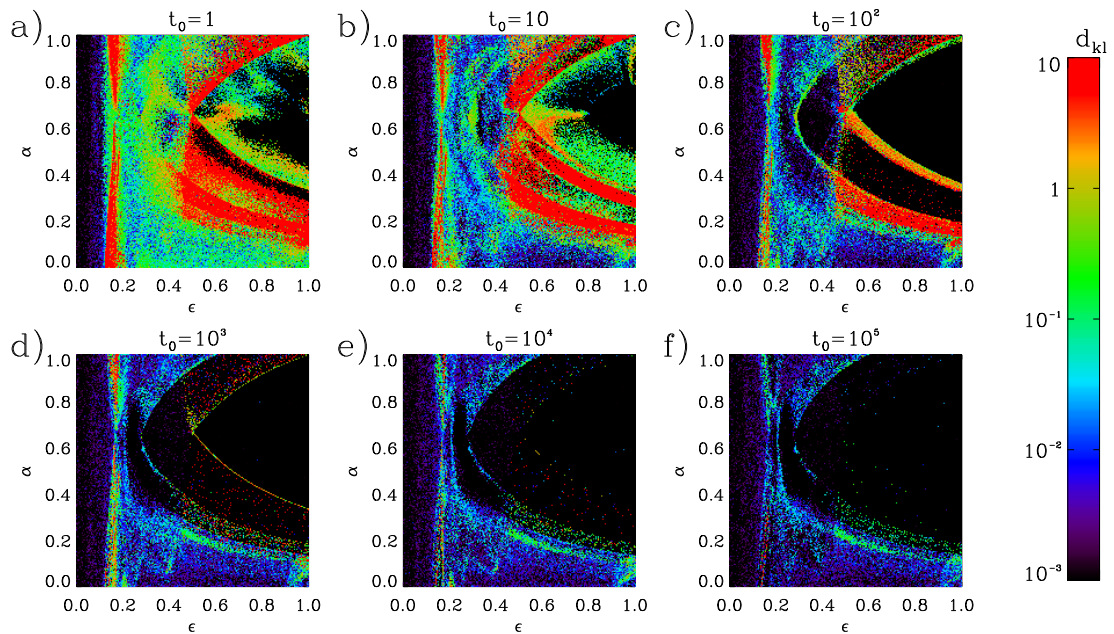


Fig. 4.23: Prediction error in terms of the Kullback-Leibler distance between the algebraic order distribution of the converged state and the predicted one, for different values of t_0 .

In a second approach, I predicted the regime of the stationary state. Since the set of regimes is discrete, the weighted average used above is not applicable. Instead, I used a voting method considering the nearest 5 elements. In the case of a tie, the set was enlarged until the 'winner' was unique.

Fig. 4.24 shows the prediction results, the true regimes and the corresponding error rates as a function of t_0 . Even after the first step, the main regions of the parameter space are visible to some extent, and the prediction is surprisingly accurate (65% recognition). For high t_0 , the recognition rate increases to 90%, which is mostly reached at $t_0 \approx 10^3$. Especially the individual chaos regime can be distinguished from the rest very early. Fig. 4.24g and h show the *false positive rates* (or *significance level*), i. e. the conditional probability

$$p_i^{fp} = p(\text{'regime \#i was predicted'} \mid \text{'the trajectory is from another regime'}), \quad (4.31)$$

and the *false negative rate* of the prediction,

$$p_i^{fn} = p(\text{'another regime was predicted'} \mid \text{'the trajectory is from regime \#i'}). \quad (4.32)$$

Most errors occur at regime boundaries where continuous transitions happen, for example between the coherent clusters and checkerboard clusters regime, or at the boundary to the collective chaos regime. In these cases, the boundaries are blurred by fluctuations of the dynamics (and hence of the symbolic description) both in the transient and in the converged state. Checkerboard structures with and without defects are a special case of this: all checkerboards start with defects, and even in the converged state, the difference between stable defects and defect-free checkerboard structures is subtle.

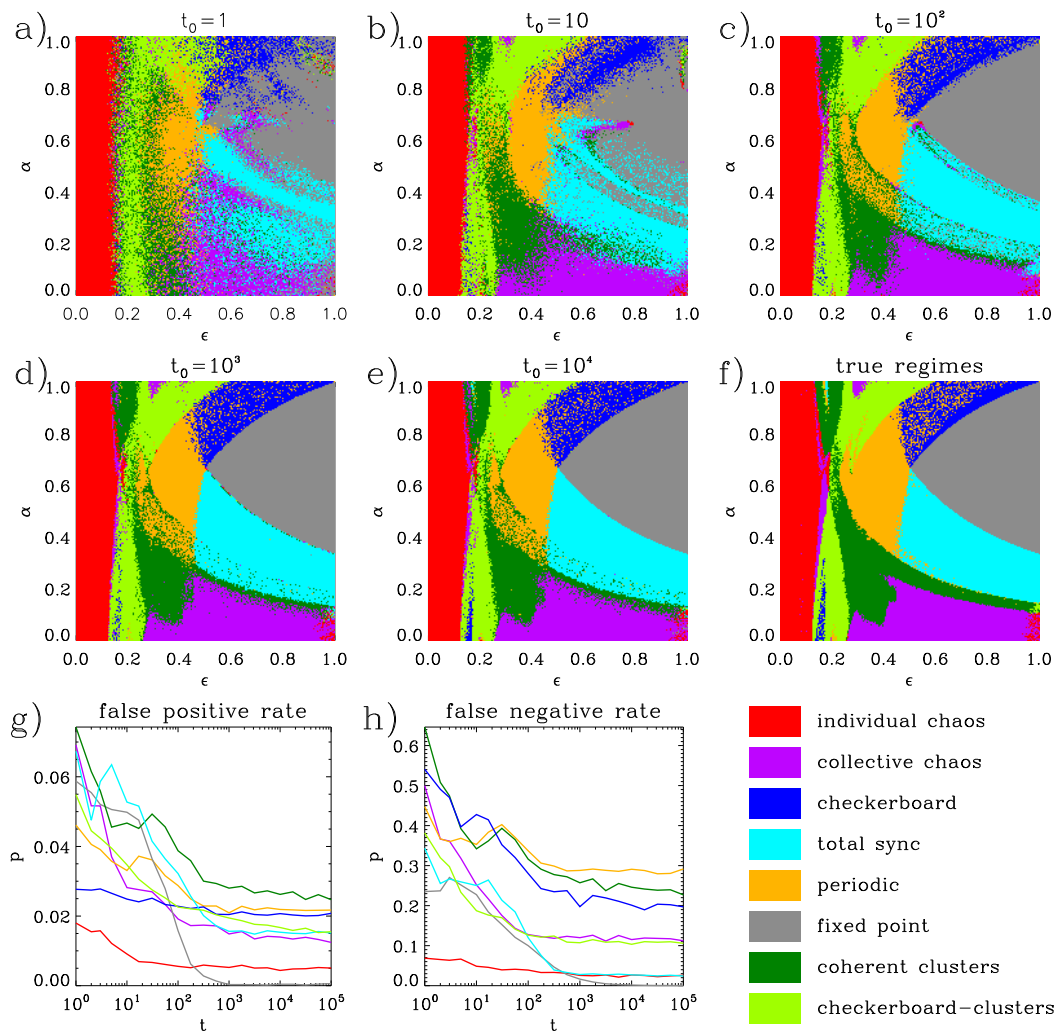


Fig. 4.24: Evaluation of the discrete prediction approach. a) – e) Predicted regimes for different values of t_0 . f) The regimes as defined in section 4.2. g) False positive rate. h) False negative rate.

Chapter 5

Application to a Life Science System: Multi-Channel EEG

This chapter is about an attempt to transfer methodological procedures developed in the framework of the investigation of coupled map lattices (CML) to *electroencephalographic* (EEG) data from the human brain. Section 5.1 starts the chapter with introductory remarks to technical aspects of the EEG recording, as far as they are necessary for the understanding of the following sections. It considers multiple aspects such as electrode placement, reference montage, voltage and frequency ranges, and artifacts. Section 5.2 gives important clinical and technical details about the examined data set, like the measuring protocol and electrode scheme.

Section 5.3 studies spatial aspects of the EEG data. As a first step, the entropy of transfer symbols is used to measure the level of interrelation between pairs of electrodes as a function of their distance. The aim is to show the existence of spatial structure in the EEG, motivating the use of transfer symbols. In the following, a low-dimensional description space is defined using the order of transfer symbols between the signals of adjacent electrodes, characterizing the transitions between states of consciousness. This description is used to construct a measure for the hypnotic component of anesthesia ('anesthetic depth'), which is evaluated quantitatively.

Section 5.4 is about *auditory evoked potentials* (AEP), which are the parts of the EEG signal related to the processing of acoustic stimuli. The known reproducible AEP components are described, together with necessary technical details. A symbolic representation is defined from single epochs of the original data, resulting in a description that potentially reveals information that would otherwise be lost in the commonly used averaging over multiple epochs. The separation of different states of consciousness is studied.

5.1 The Electroencephalogram

5.1.1 The Brain as a Coupled System

The human brain is probably the largest known real-world system that can be interpreted as a system of coupled oscillators. *Neurons* can be modeled as electrical oscillators and are coupled via *synapses* in a huge network with a complex geometry. Following Nunez and Srinivasan [68], I briefly introduce the relevant brain structures. The main functional parts of the human brain are the *brain stem* (which relays signals between the spinal cord and higher brain regions), *cerebellum* and the *cerebrum*. The outer layer of the cerebrum is called the *neocortex*, a region of about 10^{10} neurons, which are strongly interconnected (10^4 - 10^5 *synapses* per neuron). Its form resembles a folded sheet, with a thickness of 2-5 mm and a total area of up to 4000 cm². Most of the neurons in the neocortex are *pyramidal cells*, which are grouped in *microcolumns* (about 10^2) and *macrocolumns* (10^5 - 10^6 neurons). They act as electric dipoles, generating a potential that extends to the scalp if enough neurons are firing in sync (about 6×10^7 or 6 cm² of cortical tissue). The potentials that can be measured on the scalp are believed to mostly originate from the neurons of the neocortex.

5.1.2 Reasons to Study the Electrical Activity of the Brain

A state of consciousness is like a global mode of operation of the brain. Examples for states of consciousness are: relaxed wakefulness, concentration, REM sleep, unconsciousness, or coma. In the field of anesthesia, one important issue is monitoring the state of consciousness of surgery patients. Present day general anesthesia has three components, namely analgesic (suppressing pain), hypnotic (loss of consciousness) and (if necessary) muscle relaxation. If the hypnotic effect is not sufficient, *intraoperative awareness* [88] can occur. It is estimated to occur in about 0.1-0.2% of all cases, and can lead to severe psychological traumata. To prevent this, one would like to monitor the effect of the hypnotic component individually during a surgery.

The most direct indicator for consciousness is the response to command. This is not applicable if a muscle relaxant is administered, hence other methods of surveillance are necessary. Common methods, including the monitoring of vegetative parameters like heart rate and blood pressure, are of limited reliability [18]. For the distinction between different states of consciousness the EEG is a promising candidate, because it allows a more direct observation of the target organ of anesthesia (see Schneider et al. [89] or Bruhn et al. [18] for a review of EEG-based monitoring methods).

There are several pathologies associated with specific features of the electric activity of the human brain, like tumors or epilepsy. In cases like these, the EEG can be used as a differential diagnostic tool for detecting pathologies in a seemingly healthy brain, or for studying the underlying mechanisms.

Of course, the healthy brain is also an interesting system to study for its own sake. While many connections can be drawn between cognitive tasks and specific brain regions, the system as a whole is far from being completely understood and there are many open questions about the functioning of the human brain.

5.1.3 The EEG as an Observable of a Complex System

Recording surface EEG is a non-invasive way to access the electric field of the brain through electrodes placed on the scalp. Following Nunez and Srinivasan [68], the electric potential on

the surface is a mixture of signals from different regions, dominated by the neocortex. The typical scale of EEG signals is 20-50 μV , which is about a factor of 10^3 below the scale of an *electrocardiogram* (ECG). The surface EEG has a low spatial resolution (several cm), but a high resolution in the time domain (in the range of ms). However, high frequencies tend to be contaminated more strongly by noise.

Apart from the scalp EEG considered in this work, the EEG can be recorded with electrodes that are placed on the surface or even deep into the brain. This *intracranial* EEG can accurately measure local effects, at the price of severe surgical procedures. For ethical reasons, this approach is limited to patients with severe neurological pathologies. It is typically used preparatory for epilepsy surgery or tumor excision.

Measured Features

The *background activity* or *spontaneous EEG* (see [68]) is the part of the EEG that is not related to specific cognitive tasks. A straightforward description of such a time series is its power spectrum. In the context of EEG analysis, there is an established division of the frequency range in frequency bands. The power of different frequency bands is a commonly used observable, which can sometimes be associated with certain kinds of brain activity (see for instance Nunez [68]), and changes under the influence of anesthetics (Murphy [66]). Note that the conventions for the definition of the bands differ slightly for different sources. The background activity will be studied in the view of a symbolic description in section 5.3. See also Jordan et al. [44] for a summary of different approaches to measure anesthetic depth using order pattern analysis of the EEG background activity.

In addition to the background activity, so called *graphoelements* are local patterns in the EEG data, which can be an indication for certain pathologies. In the clinical situation, specially trained neurologists visually inspect EEG recordings for occurrences of known patterns. See Weinmann [107] for a catalog of defined graphoelements including numerous samples of EEG data. Note that the classification of a pattern as normal or pathologic is highly age-dependent. Symbolic representation are a promising method to describe such local patterns. However, graphoelements will not be considered here, because they are rather sporadic indications for certain properties of an individual. The subject of this chapter is the monitoring of the (highly variable) state of consciousness based on short samples of EEG data.

The expressions *evoked* and *event-related potentials* (EP/ERP) refer to the electrical activity on the scalp that corresponds to the processing of certain stimuli. They are small in amplitude, but can be accessed by repetition of similar stimuli, and can give valuable information because the activity can be related to certain cognitive functions. Section 5.4 will study the auditory evoked potentials (AEP) caused by binaural clicking stimuli.

Artifacts

Artifacts are features in the measured data that are not related to the processes to be observed, but originate in an interference from other processes or a disturbance of the measuring apparatus. There are many issues and effects in the course of an EEG measurement that can lead to artifacts. Due to individual differences in skin properties and effects like sweating, the surface conditions on the skin can vary spatially, between individuals, and in time. Hence, calibration is difficult and the scaling of the data must be considered with care. The measurement is done using an electrode cap, therefore any movement of the head or the cap is critical. Changes in

the impedance between the electrode and the skin can cause disruptions, or fluctuations in the scaling of the signals. Since the measured potential differences of the EEG are small, the whole measuring apparatus is vulnerable to electro-magnetic perturbations (the most obvious ones being 50 Hz-perturbations from the power supply). Furthermore, there can be influences from the *electrocardiogram* (ECG).

Muscle activity is accompanied by electrical signals, the *electromyogram* (EMG), which typically have magnitudes dominating the EEG signal. Since muscular signals mainly affect the high frequency ranges, it is common to use a lowpass filter before evaluating the EEG data, commonly used values for the upper limit range from 30 – 50 Hz (see Bonhomme and Hans [16]). Whitham [108] even reports observation of myogenic signals in frequencies down to 20 Hz. In studies of evoked potentials this limitation is usually bypassed by trigger-synchronized averaging over multiple *epochs*, i. e. samples of EEG data recorded after similar stimuli.

Reference Potential

Even though one is mainly interested in electric potentials, only potential differences can be observed, hence the potential at each electrode is measured with respect to a reference. Since there is no canonic global potential that qualifies as a 'mass', the reference potential has to be defined from the electrode values. Especially for the question of synchronization this can be an issue. Suppose several signals are measured with respect to a common reference. If the signals are independent and a perturbation is added to the reference, it shows up (with opposite sign) in all of the time series. This can lead to positive correlation coefficients, which could be spuriously interpreted as synchronization behavior.

For the surface EEG, there are numerous so called *reference montages* in use, like *bipolar recordings* (differences between closely spaced electrodes), or using *common reference* electrodes. One can also use an average over all or the neighboring electrodes as a reference, using simple averaging or more sophisticated methods like spline interpolation, see [67] – [69], [85] for details and comparative studies on some commonly used methods. In the following, the reference used was the average over all electrodes.

5.2 Experimental Setup

The data examined here was obtained as part of a study on *auditory evoked potentials* (AEP), which was designed and carried out at the *Department of Anesthesiology, Klinikum rechts der Isar, Technische Universität München* (Munich, Germany) [49]. 15 healthy probands were treated with *Propofol* using *target-controlled infusion* (TCI) while recording their EEG. The protocol starts with a 15 min *baseline* EEG of the awake proband, then Propofol was administered. The concentration was increased stepwise, until a *loss of consciousness* (LOC) was observed. Then, the concentration of Propofol was kept constant at this level for 15 minutes. Afterwards, the infusion was stopped and the EEG measurement was continued until 5 minutes after the *return of consciousness* (see the sketch of the protocol in fig. 5.1).

The state of consciousness was tested by the proband's response to the request of pressing the operator's hand. In order to study AEP, the probands were exposed to an auditive stimulus (a binaural clicking sound) about every 120 ms. The time delay was varied slightly (standard deviation $\sigma = 7.2$ ms) in order to avoid habituation effects. The times of these stimuli were recorded.

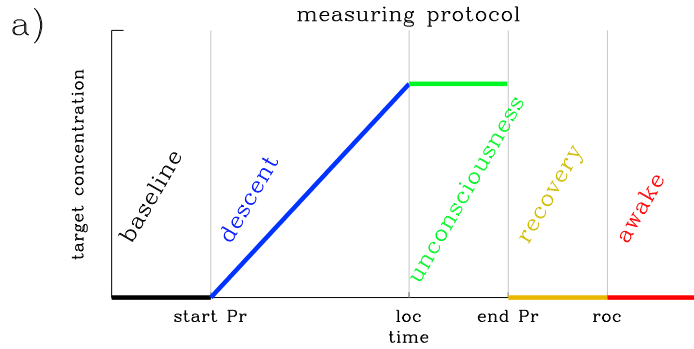


Fig. 5.1: The measuring protocol starts with 15 minutes of baseline EEG, then Propofol is administered with an increasing concentration until a loss of consciousness is observed. The concentration is kept constant for 15 minutes. Then, the infusion is stopped and the EEG measurement is continued until 5 minutes after the return of consciousness. These events separate the experiment into five regimes, which I refer to as *baseline*, *descent*, *unconsciousness*, *recovery*, and *awake*.

To obtain comparable data from surface EEG measurements, one needs a standardized scheme of scalp electrode positions that is applicable to different head sizes and shapes. The *international 10-20 system* [42] is such a standard set of positions, which is anchored on the *inion* and *nasion* points on the skull. Using these two landmarks, 21 electrode positions are defined using units of 10% or 20% of the inion-nasion distance. The data used here was obtained using an extended form of the international 10-20 System, consisting of 29 scalp electrodes (see fig. 5.2), with impedances $< 5 \text{ k}\Omega$, integrated in an electrode cap. For better visualization, a schematic diagram of the positions is shown (fig. 5.2) instead of an exact projection of the 3-dimensional geometry. The potentials are defined with respect to the average potential over all 29 electrodes:

$$\Phi_{\text{ref}} = \frac{\sum_{i=1}^{29} \Phi_i}{29} \quad (5.1)$$

The sampling rate of all time series was 5 kHz.

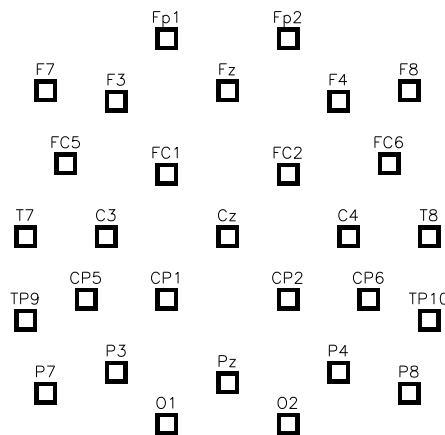


Fig. 5.2: Extended 10-20 system with 29 electrodes (schematic illustration, view from above with the nose pointing upwards).

5.3 Spatial Phenomena

5.3.1 Formal Similarities between Multi-Channel EEG and CML

As mentioned, the measurement scheme of the electrical activity of the brain, i. e. the topography of the electrode grid, suggests to transfer elements of the methodology developed for the coupled map lattices to the study of multi-channel electroencephalographic data. The positioning scheme of the electrodes defines a spatial structure on the set of time series. Since the coupling is complex and non-local, the concept of 'neighboring' electrodes is not as clear as in a CML. Because the zone of influence of an electrode is not well-defined and – on the other side – signals from an extended active region may be measured by multiple electrodes. Therefore, the different channels are not expected to be independent.

However, from a formal point of view, many of the questions addressed in the context of the coupled map lattices are similar to those arising in the analysis of EEG data. For instance the description and distinction of the system's dynamical regimes, like different states of consciousness in the case of the human brain. Another common aim in both fields is to identify structures of emerging order in different regimes of the system, and to relate them to certain parts of the system (see the spatially resolved measures in section 5.3). This can give insights about the internal mechanisms or be useful for the recognition of different regimes.

For example, Rodriguez [80] observed long-distance synchronization effects in the gamma band related with the visual perception of faces. Since other cognitive functions have similar effects, those should affect the background activity, in a way that depends on the state of consciousness. These effects can possibly be accessed by symbol-based measures like those used for the CML in the previous chapter.

5.3.2 Structure on Different Scales

In order to apply methods from coupled map lattices to EEG data, a first step is to provide evidence of spatial structure, i. e. investigate dependencies between the time series corresponding to different electrodes. This is a test of the premise that there are local synchronization effects, which is important to support the analogy between the coupled map lattice of the preceding chapter and the EEG, and to motivate the application of the methods used there.

For each pair of electrodes, I described the relation between the corresponding time series by a sequence of transfer symbols. The delay $\tau = 6$ ms turned out to give the best distinction between the states of consciousness. This measure mainly describes the alpha, beta, and gamma band: for sequence length $n = 5$, the time horizon is 24 ms, which corresponds to about 1/4 period at 10 Hz (alpha band), or about a full period at 40 Hz (gamma band). Therefore, I expect the symbols to be mainly sensitive for the *alpha*, *beta* and *gamma* bands. Lower frequencies are probably manifest as trends, which I expect to be largely masked by high-frequency signals. A digital filter for frequencies from 0.5-50 Hz was used.

As a measure for the degree of interrelations between the signals, I use the entropy of the transfer symbols, leading to a scalar value for each pair of electrodes. High entropy suggests randomness and is expected for a pair of independent signals. Low entropy is an indication for (not necessarily linear) correlations.

The electrode positions on the skull were given in spherical coordinates, hence it is natural to measure the distance between two electrodes in degrees. The electrode distances for a certain proband depend on the geometry of the individual skull, which was not recorded. Fig. 5.3 shows the transfer symbol entropy as a function of the electrode distance. The gray line marks the

upper bound of the entropy at $\log_2(n!) \approx 6.9$ bits. Curves were fitted by a polynomial of degree 4 for each individual.

For all probands, the dependence was highly similar. The scattering of the individuals was mostly due to the constant term of the polynomial, corresponding to an individual offset in entropy. In the unconsciousness regime, the offset was smaller and showed a larger scattering of the individuals. This suggests an individually different level of 'mean-field-synchronization', but could possibly be related to individual differences in the power spectrum.

At short electrode distances, there were clear signs of structure. I observed a dip at distances around 135° , most pronounced during unconsciousness, which possibly indicates long-range synchronization effects. The non-monotonic dependence on the distance indicates that this is not explained purely by neighboring electrodes sharing parts of their sources.

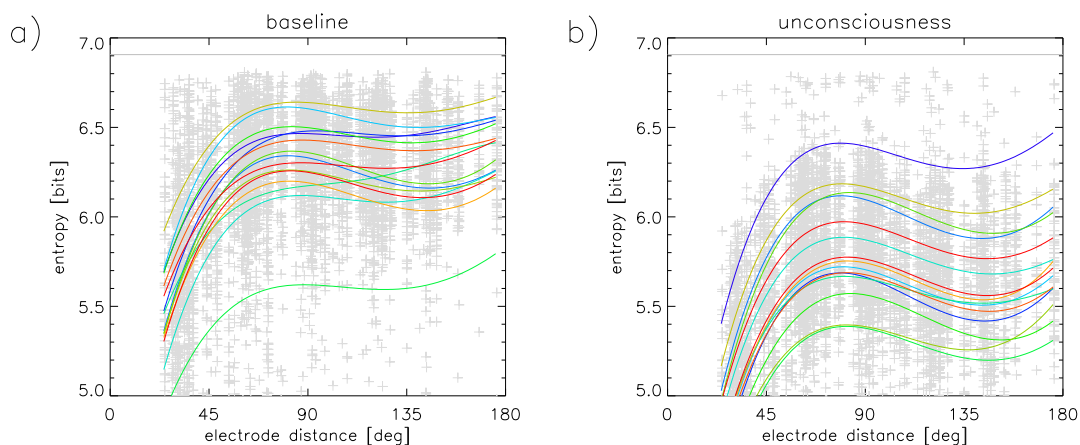


Fig. 5.3: Transfer symbol entropy ($n = 5$, $\tau = 6$ ms) versus electrode distance. a) Baseline b) Unconsciousness. The lines show a polynomial fit of order 4 over all electrode pairs, performed for each of the 15 probands separately (the colors correspond to the different probands).

Next, I asked if the observed long-range correlation is related to the symmetry between the left and right hemisphere of the brain. In fig. 5.4, I separated the data into symmetric (the two electrodes are situated at corresponding positions of different hemispheres) and non-symmetric electrode pairs. Note that the fitted curves are based on different sampling points, which are relatively sparse in the symmetric case.

The green curves (non-symmetric pairs) are similar to the curves in fig. 5.3, because they are based on almost the same data. For the unconscious regime, the red curve (symmetric pairs) is monotonic, suggesting that the observed long-range synchronization effects are not directly related to symmetric pairs of electrodes. For the conscious state, the disparity between symmetric and non-symmetric pairs is not as distinct. As before, the states of consciousness mainly differ by an offset in entropy.

In order to study interrelations on a more local level, fig. 5.5 considers the same measure (transfer symbol entropy versus electrode distance), restricted to pairs of electrodes within selected regions of the scalp (as defined in fig. 5.5a). Since only electrodes within the same region are considered, the range of distances is smaller than in the previous figures.

Fig. 5.3b and c compare regions with identical electrode geometry, namely the front and back region, and the left and right region. For these pairs of regions, the polynomial fits are based on the same set of sampling points, hence it seems reasonable to compare them pointwise.

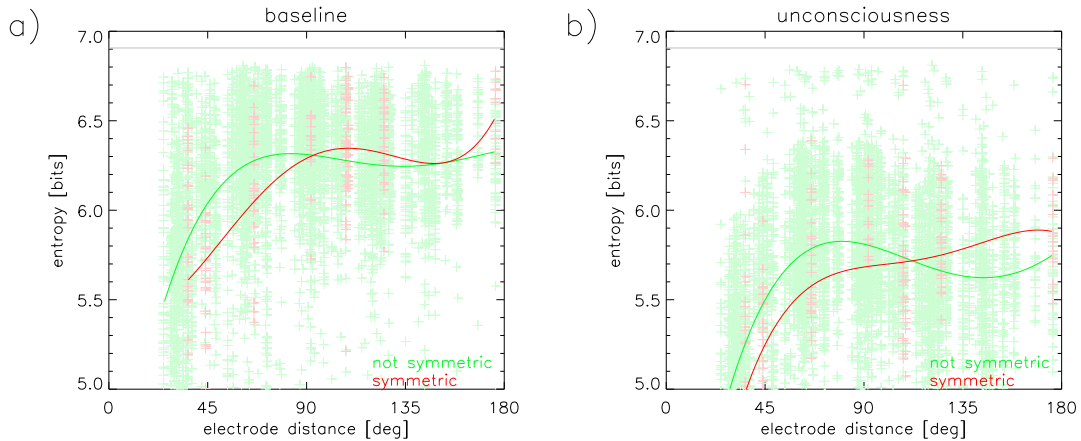


Fig. 5.4: Transfer symbol entropy ($n = 5, \tau = 6$ ms) versus electrode distance. a) Baseline b) Unconsciousness. Polynomial fit of order 4 to the data of the symmetric electrode pairs (red) and of all other pairs (green).

I estimated the variation among the probands using a *bootstrap approximation*: several curves were fitted to samples of 15 probands that were randomly drawn with replacement. I used the curves to estimate the standard deviation of the fit curve, which is shown in the form of error channels. The qualitative behavior of the examined regions was reproduced well between the baseline and unconsciousness regimes. Generally, the entropy was lower for unconsciousness. This may be due to the aforementioned differences in the power spectra of both populations. Between the front and back region, the fit curves indicate a considerable difference in the structure. The front region had a monotonic dependence on the distance. The back region followed a more complex relation, suggesting long-range dependencies. The left and right regions were similar, yet there might be a systematic difference for short electrode distance, suggesting more structure in the symbolic description of the left hemisphere.

5.3.3 Paths between Hypnotic States

This section defines a simplified state space for the 'ultrahigh-dimensional dynamical system' of the human brain. The aim is to describe essential properties to map the dynamical regimes that are of interest for this study, namely the states of consciousness that correspond to different depths of anesthesia.

I derived the methodology used here from an approach that proved to be useful for the coupled map system in chapter 4. A symbolic representation was mapped into a low-dimensional description space using the distribution of the algebraic order. This results in a trajectory that represents the changes in the state of consciousness over the course of the experiment.

In an analogy to the coupled map lattice in chapter 4, I defined a neighborhood-relation between the EEG electrodes (see fig. 5.6), specifying between 2 and 6 neighbors for each electrode. Later, I will draw topograms, assigning the data corresponding to a pair of electrodes to the center of their connecting line. In order not to have different pairs assigned to the same position, I avoided crossing edges, i. e. the neighborhood relation corresponds to a triangulation. For each pair of neighboring electrodes, the transfer symbol distribution ($n = 5, \tau = 6$ ms) was calculated.

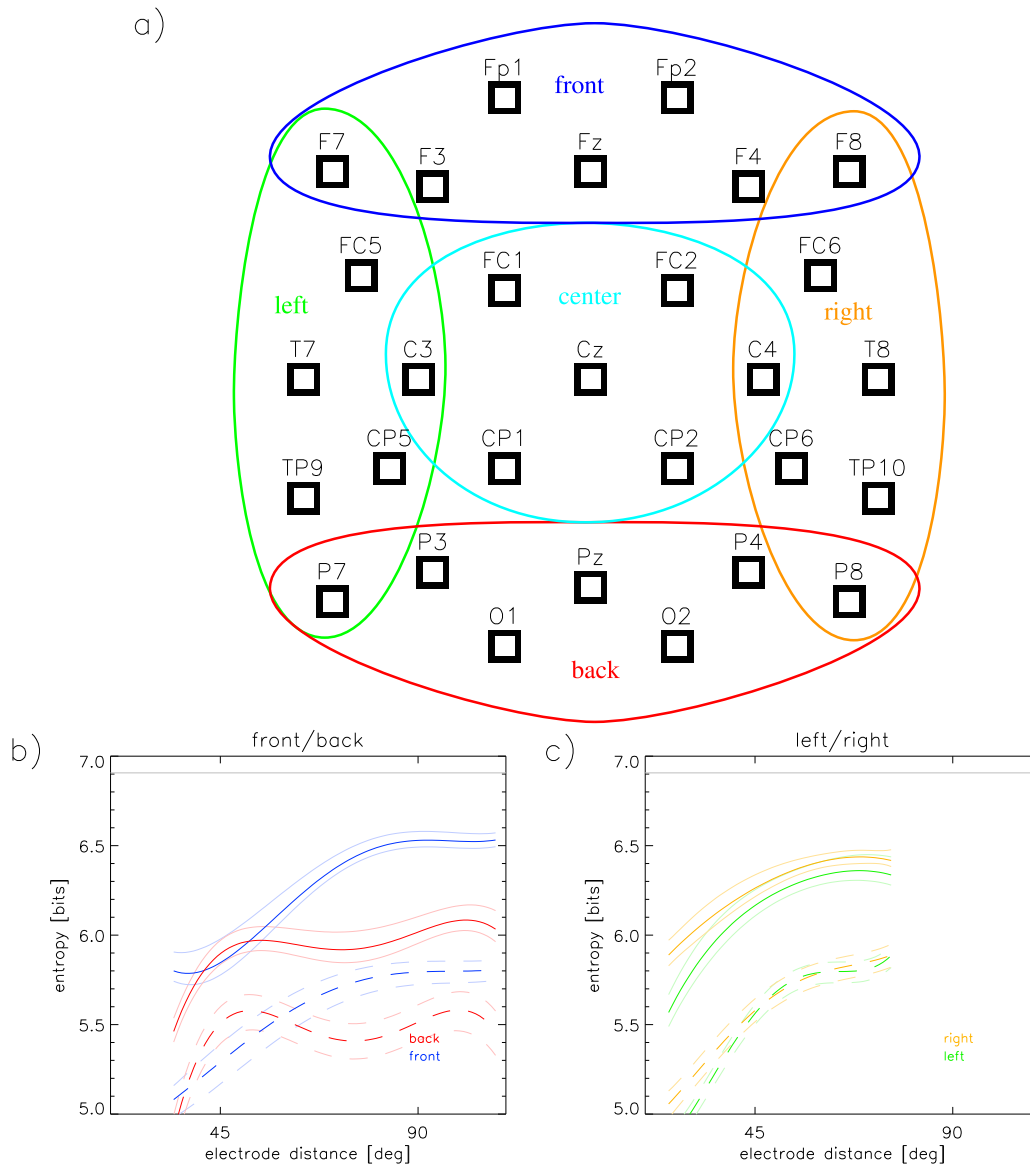


Fig. 5.5: Transfer symbol entropy ($n = 5, \tau = 6$ ms) versus electrode distance for pairs of electrodes within different regions of the skull. a) Definition of the regions b) Comparison of front and back region c) Comparison of left and right region. The lighter curves mark the standard deviation (across probands) of the fitted curves, based on a bootstrap estimation. Continuous lines mark the baseline and dashed lines the unconsciousness regime, respectively.

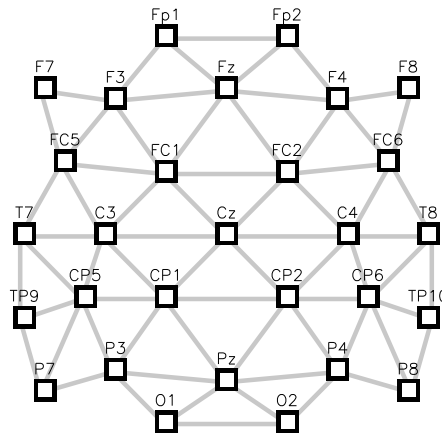


Fig. 5.6: A neighbor relation was defined on the electrode grid, avoiding crossing edges.

In order to allow a visualization as a trajectory in a low-dimensional space, the algebraic order distribution of the transfer symbols was averaged over all neighboring pairs of electrodes. The symbols of sequence length $n = 5$ can have an algebraic order from 1 to 6. Since the relative frequencies add up to 1, the order distribution has 5 degrees of freedom. The description space is the 5-dimensional *affine space* spanned by the orders $1, \dots, 6$ (however, the set of normalized order distributions is the convex hull of the orders). See section 4.4.1, especially fig. 4.18, for the corresponding description of the CML.

Since the following investigations used data from all regimes (see fig. 5.1), only the data from 10 probands could be used (inclusion criterion: 5 min of continuously recorded data in the baseline, unconscious and awake regime, respectively). Since the recovery process can be individual, the recording was stopped soon after the return of consciousness for certain probands. The investigations done so far only used data from the baseline and unconsciousness regimes, which is available for all 15 probands.

Fig. 5.7 shows 2-dimensional projections of the trajectory in the description space, based on overlapping sliding windows of 30 sec length. The regimes are color coded.

The baseline, unconsciousness and awake regimes are expected to be approximately stationary (near steady state conditions). In the description space, they can be identified as compact clusters. The descent and recovery regimes were defined as transition between the supposedly stationary states. Those transitions would resemble smooth (or at least monotonic) paths with added noise, which is in a reasonable agreement with fig. 5.7. The trajectory follows a corridor between the awake regime and the unconsciousness regime. The individuals differ mainly in the positions of the cluster centers.

The baseline regime was not always consistent with the expectations. Even though it was generally related to the more awake states, the connection from the baseline sample to the rest of the trajectory was not as smooth as expected. In contrast to the assumption of an approximately stationary state, the transition from the baseline to the descent regime was clearly discontinuous in some cases. The variation in the location of the baseline cluster between individuals was larger than for the other regimes, including a single case (#6) whose baseline regime had the same order distribution as it is typical for the unconsciousness regime.

The observed discrepancy between the baseline and the rest of the data needs some explanation. It should be mentioned that the data was not continuously recorded at this point (the baseline data was separate). There was possibly a short time gap between the data of the baseline regime and the rest of the data (in the order of several minutes). However, when

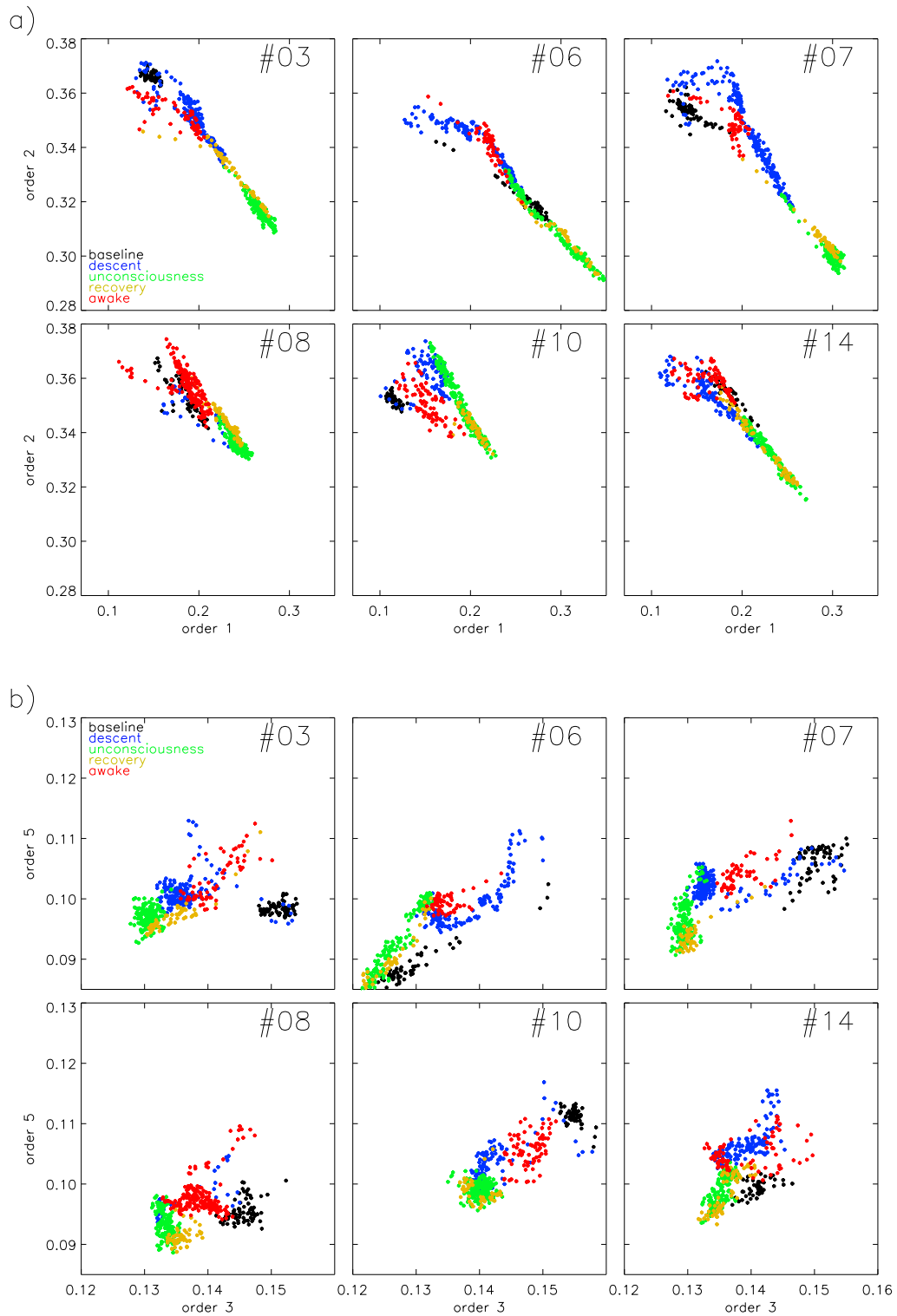


Fig. 5.7: EEG trajectory in terms of the algebraic order distribution (for single probands, over all pairs of neighboring electrodes). The regimes are color coded, the values are based on overlapping sliding windows of 30s length. a) Order 2 versus 1 b) Order 5 versus 3.

considering the variation over time, a gap in the data is not likely to fully explain the observed discrepancy. This observation suggests that the probands behaved more individually before the medication and more commonly under the influence of Propofol.

Some individuals differ fundamentally from the bulk of the group. For proband #10 for instance, the separation line between unconsciousness (green) and awake (red) in fig. 5.7a had a completely different direction, because the unconsciousness regime had more order 2 and less order 1 symbols than usual. Another example is the aforementioned proband #6, where baseline and unconsciousness were not distinguished at all.

In summary, I conclude that the proposed description space provides a useful mapping of the main features that distinguish the regimes addressed by this study.

5.3.4 A Symbol-Based Measure of Anesthetic Depth

Based on the description space from the previous section, I propose a classifier for anesthetic depth, more precisely a scalar quantity describing the features that distinguish the conscious from the unconscious state. Exploiting the multi-channel EEG data, a spatially resolved description of the transition process might be possible.

In order to establish a 1-dimensional scale, two *reference regimes* for consciousness and unconsciousness, respectively, were chosen and represented by their order distribution. This was done separately for each neighbor pair of electrodes, so that the *template* of a reference regime consisted of the average order distribution for each pair of electrodes.

When evaluating a *test sample* consisting of a short sequence from one pair of electrodes, I compared its order distribution o_s to the pair-specific templates o_{co} and o_{un} of the conscious and unconscious reference regime, respectively. The comparison was done in terms of the Kullback-Leibler distance d_{KL} (as described in section 3.2.3). As a classifier for the test sample, I used the normalized difference

$$m := \frac{d_{KL}(o_s, o_{un}) - d_{KL}(o_s, o_{co})}{d_{KL}(o_s, o_{un}) + d_{KL}(o_s, o_{co})}. \quad (5.2)$$

Values close to $m = 1$ indicate the conscious and values close to $m = -1$ the unconscious regime.

In order to have a precise representation of the states of consciousness, it is advantageous to use templates based on an EEG sample from the individual. Having a real surgery situation in mind, I suppose that a template o_{co} for the conscious regime can be obtained from each individual as a preparatory step prior to the administration of the anesthetic. This method is referred to as a *personalized template*. In this case, whenever evaluating a sample from the conscious reference regime, i. e. baseline or awake, this sample was left out when generating the template. The alternative is to base the template on the data of the other probands, which is referred to as a *common template*. This was always done for the template o_{un} of the unconsciousness regime. Note that both methods are cross-validation approaches, excluding either the test sample or all data from the test proband from the training sample.

Fig. 5.8 shows the classifier m for a typical proband. The average over all pairs of neighboring electrodes (fig. 5.8a) exhibits a smooth transition between the states and an apparent plateau of distinct level in the unconsciousness regime, in agreement with the expected stationarity. At the end of the measurement, the distinction from the plateau is apparent.

In fig. 5.8b, *topograms* show spatially resolved snapshots of m at fixed times, indicating that for this individual, the distinction is best in the frontal and occipital scalp regions.

Due to the personalized baseline template, the classifier tends to have smaller variance over the probands when evaluating samples of the baseline regime (compared to the unconsciousness regime). Therefore, the threshold that minimizes the total number of mis-classifications is slightly shifted from zero to positive values.

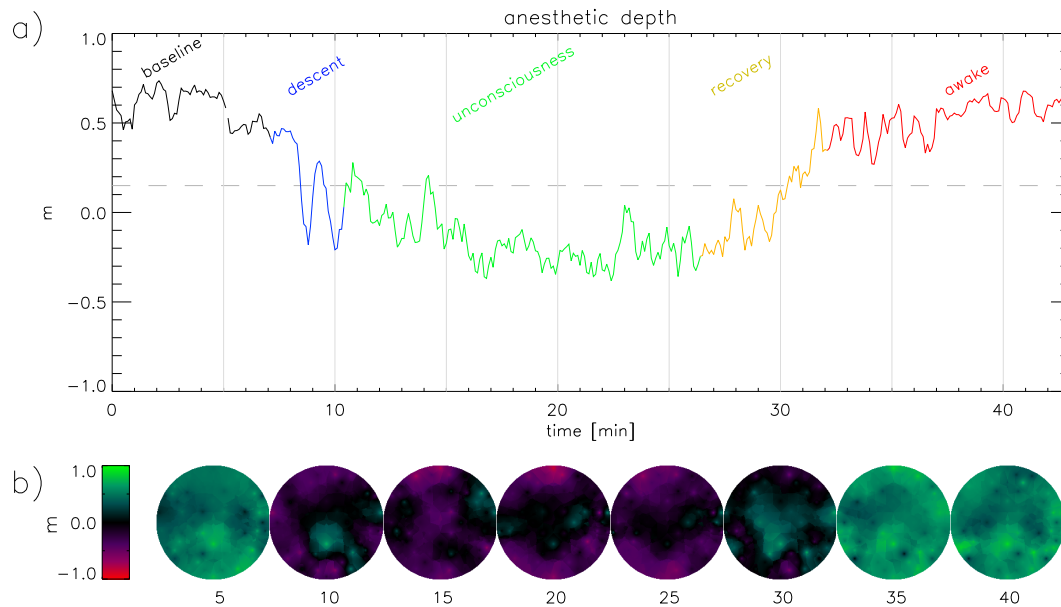


Fig. 5.8: Anesthetic depth in terms of the classifier m , for a typical proband (#8), with baseline (personalized template) and unconsciousness as reference regimes (30s sliding window, both for curve and topograms). a) Average of m over all neighbor pairs of electrodes, the color codes the regime as in fig. 5.1. The dashed line at $m = 0.15$ marks a decision threshold optimized for minimal total number of misclassified baseline or unconsciousness samples over all probands. b) Topograms of the classifier: green indicates a classification as conscious and red as unconscious. As mentioned, there was a possible time gap in the recording, marked by the discontinuity in the baseline regime.

Fig. 5.9 gives topograms of m at selected stages of the experiment. The measure does not always exhibit a clear change at the time of observed loss and return of consciousness. Even though it distinguishes the regimes, the measure often suggests different transition times than the observed ones (which were defined by the reaction to command). The average over all probands suggests that the LOC starts in the parietal regions, while the onset of the return of consciousness is not clearly localized. The classifier m often exhibits a gradual transition between the regimes, instead of a distinct change at the recorded transition times. Therefore, the topograms before and after the recorded transition are often more similar than expected. The classifier does not perform well in the occipital region. For individual probands, the observed trends are masked by fluctuations and individual peculiarities. Fig. 5.9 does not show a universal spatial sequence in the transitions. The regions where the transition to unconsciousness is observed first differ individually.

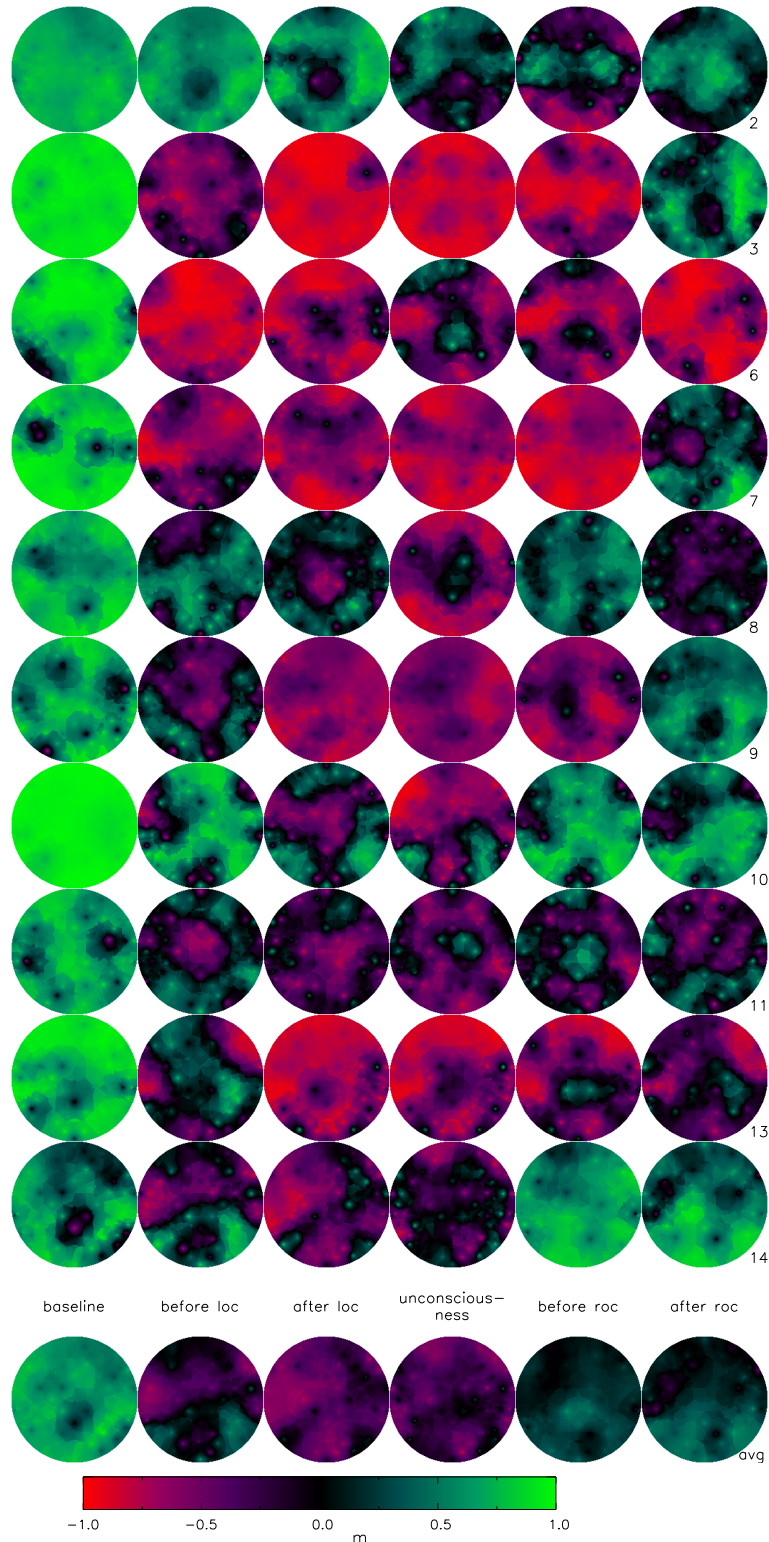


Fig. 5.9: Topograms of the classifier m at selected stages of the experiment for all 10 probands. The lowermost row shows the average over all probands. The samples are based on windows of 30 s length, taken (from left to right) during the baseline regime, 2 min before and after the recorded loss of consciousness, during the unconsciousness regime, and 2 min before and after the return of consciousness. The proband numbers at the right refer to the initial set of 15 probands.

5.3.5 Distinguishing Different States of Consciousness

In the previous section, I defined a classifier m for anesthetic depth, and showed qualitative results. Here, its discrimination power is quantified, from the perspective of a possible application as a real-time monitor for anesthetic depth. Since the classifier was defined locally (i. e. for single electrode pairs), its discrimination power can be studied in a spatially resolved way, relating the differences between the conscious and unconscious state to regions of the scalp.

The quantification was done in terms of the *receiver operating characteristic* (ROC), which I introduce briefly. It deals with the question to distinguish two populations of samples, referred to as *positive* and *negative* here. Suppose that a scalar classifier m is given, which defines a ranking among the samples. A higher ranking means that a sample is more likely to come from the positive population. The aim of ROC analysis is to quantify how useful the classifier is for separating the two populations.

The probably most straightforward quantitative measure is the error probabilities of a statistical test. Such a test is defined by the choice of a threshold T , assigning the samples with $m(x) \geq T$ to the positive population, and the others to the negative one. Since there is no canonic threshold, a measure for the discrimination potential of the classifier should take into account every possible threshold. Peterson et al. [75] propose a graph of the *true positive rate* (or *sensitivity*)

$$p(m(x) \geq T \mid x \in X_1) \quad (5.3)$$

versus the *false positive rate* (or *1-specificity*)

$$p(m(x) \geq T \mid x \in X_0), \quad (5.4)$$

which they call the ROC curve. Since both quantities grow monotonically as a function of T , the ROC curve is monotonically increasing.

As a scalar quantity for the discrimination power of a classifier, Peterson et al. propose the *area under the curve* (AUC). The AUC equals the probability that a randomly chosen positive sample is ranked higher than a randomly chosen negative sample. Note that the ROC curve is invariant with respect to monotonic transformations of the scalar classifier, i. e. it only depends on the ranking of the samples. It is straightforward to see that a perfect classifier has an AUC of 1, a random one has 0.5 and the inverse of a ranking with AUC = x has an AUC of $1 - x$.

I used the AUC for a large set of observations (all probands), as well as for subsets (a single proband). Let us take a look at the relations of these quantities. When combining data sets, the union can have an AUC far from the average of its subsets. Fig. 5.10 illustrates two examples with opposite effects. If a classifier is perfect on one subset and random on another, the discrimination can be better than the average AUC (fig. 5.10a). On the other hand, a bias of the classifier on one subset can lower the performance of the union considerably (fig. 5.10b).

I analyzed the classifier m from the preceding section in terms of the ROC. Using the average of m over all pairs of neighboring electrodes, a *global AUC* (over all probands and all electrodes) of 0.99 (baseline-unconsciousness), 0.97 (awake-unconsciousness), and 0.93 (awake-unconsciousness with common template for awake) was attained.

A spatially resolved ROC analysis (fig. 5.11) showed a good separation, especially in the frontal and temporal regions. There are regions where the separation fails, which depend on the individual and mainly appear in the occipital region of the scalp.

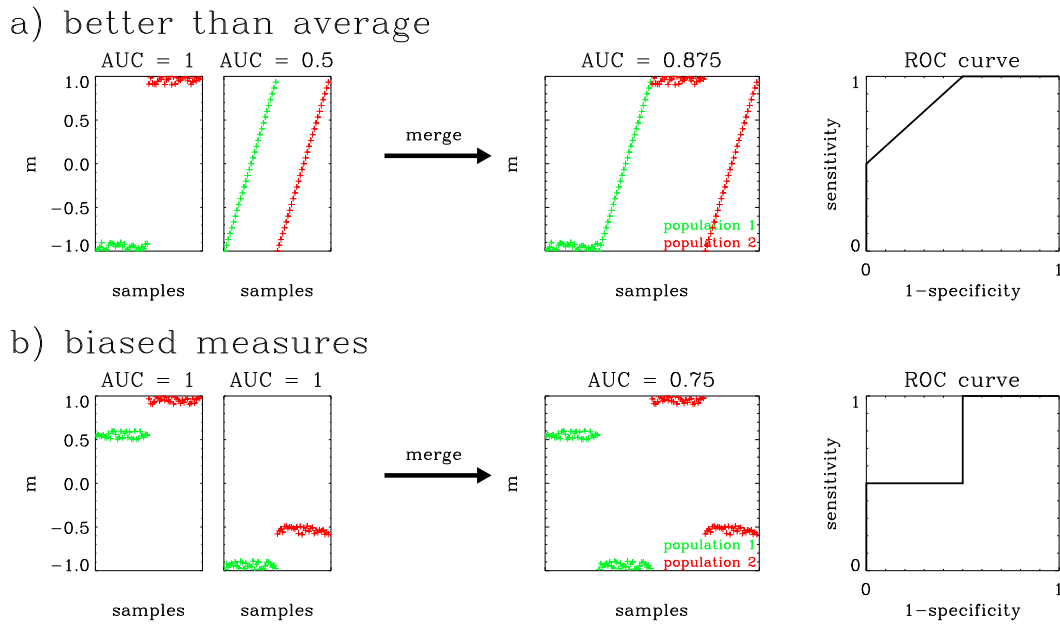


Fig. 5.10: The ROC for merged data sets. a) The global AUC can be larger than the average over the merged sets. b) An individual bias can reduce the discrimination power considerably.

The comparison of fig. 5.11 b and c shows that the personalized template is an effective means to increase the discrimination power. While technically not possible with the awake regime, it is in principle applicable to the beginning of the descent regime.

Some of the individuals presented in fig. 5.11 show isolated zones of low discrimination, which are often related to mis-classifications in fig. 5.9. These areas are generally well defined and not changing over time. Thus, these were probably not random fluctuations but peculiarities of the individual. The affected areas are situated mainly in the occipital region. The locations of the individual areas of low discrimination are generally similar for the baseline and the awake reference regime.

The baseline regime is the primary choice for the conscious reference and can in principle be measured directly before a surgery, allowing to generate a personalized template. In the context of monitoring anesthetic depth however, the aim is to detect intra-operative awareness. It is therefore not clear which regime is an appropriate representation for those intermittent moments of consciousness. I expect those moments to be more similar to the awake regime, hence for the measuring of anesthetic depth the awake regime would be the preferred reference regime.

From the ROC results, the classifier based on the the baseline regime shows the highest discrimination power (with proband #11 being the exception from the rule). Under identical conditions (i.e. when used with a personalized template), the awake regime gives a slightly lower performance. Since a sample of the awake regime can generally not be recorded in advance, fig. 5.11c probably gives the most realistic approach for the detection of intra-operative awareness in a surgery situation (awake with common template versus unconsciousness), with an AUC of 0.93.

For ease of application, it is preferable to restrict the measurement to a small set of electrodes, ideally located in the frontal area. In this study, the four front electrodes Fp1, Fp2,

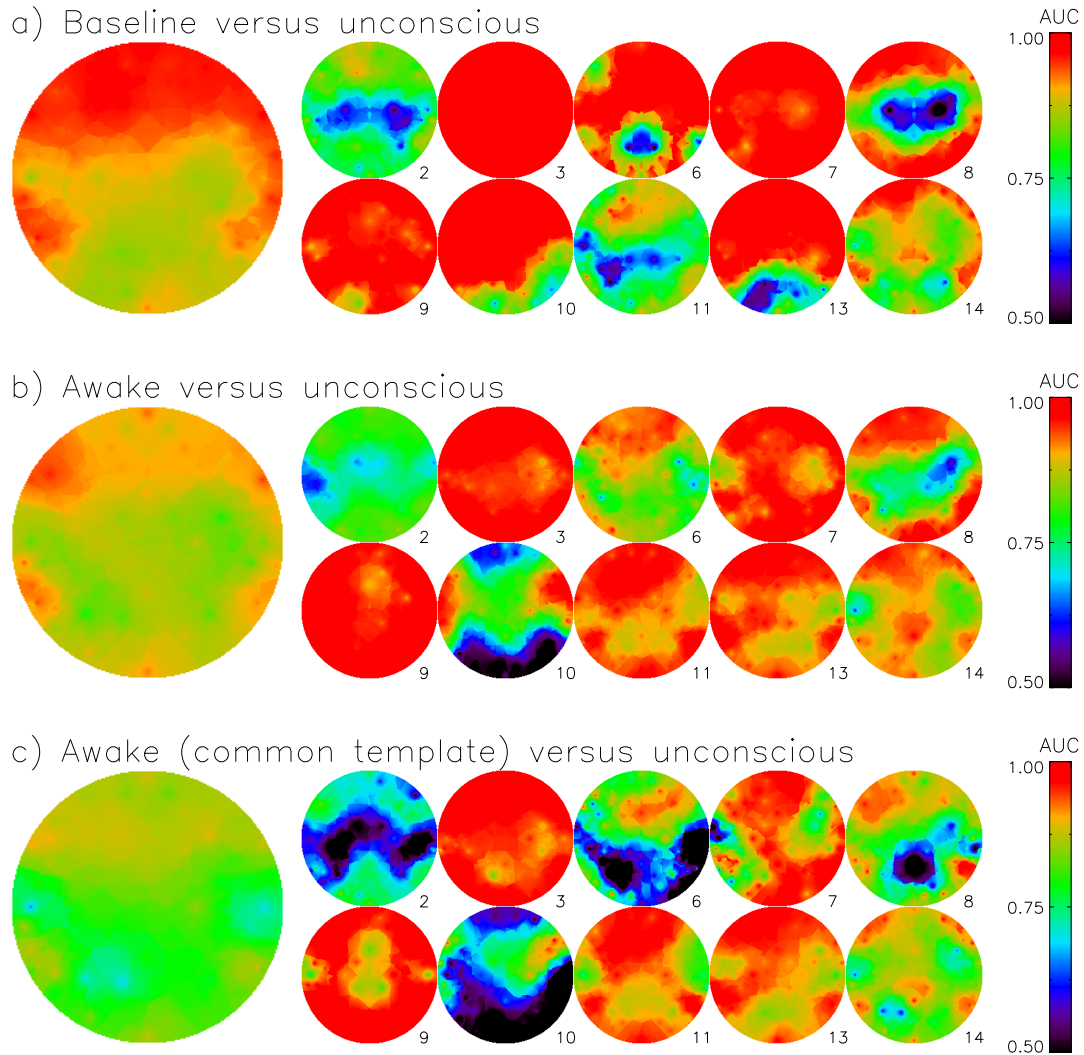


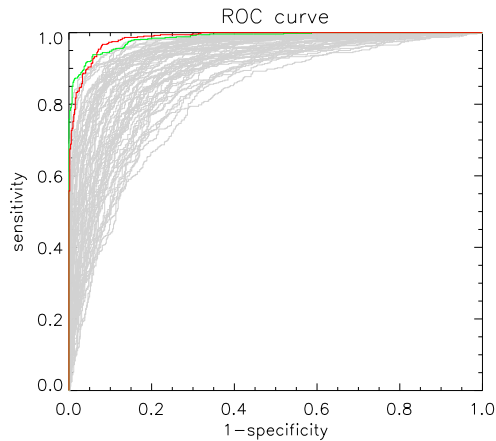
Fig. 5.11: Left: Topogram of the discrimination power (AUC) over all individuals. Right: Discrimination power for each individual. a) Baseline versus unconsciousness (global AUC 0.99) b) Awake versus unconsciousness (global AUC 0.97) c) Awake versus unconsciousness (common template for awake, global AUC 0.93). The EEG data was digitally filtered (0.5 – 50 Hz), equidistant sampling pattern with sequence length $n = 5$ and delay $\tau = 6$ ms. The classification was based on samples with a length of 6 s. For every pair of neighboring electrodes, the population comprised 52 samples per individual, for the conscious and unconscious reference regimes, respectively. The numbers beneath the topograms refer to the probands.

evaluation regimes		reference regimes					
		common template			pers. template		
		bl/un	aw/un	bl/aw	bl/un	aw/un	bl/aw
bl/un	0.926	0.922		0.986	0.928		
aw/un	0.926	0.932		0.875	0.974		
bl/aw			0.760			0.975	

Table 5.1: Discrimination power of different measures, evaluated on different pairs of regimes in terms of the global AUC. The baseline, unconsciousness and awake regimes are abbreviated as *bl*, *un* and *aw*. As mentioned, 'personalized template' only refers to the conscious states.

F3 and F4 performed as well as the complete set of electrodes (AUC 0.985 versus 0.986, see fig. 5.12). There is a range of high specificity (> 0.95) where the measure based on the front electrodes performed better. However, the difference was small and could be an artifact of the small sample size. The AUC values given here refer to sliding windows of length 6s, which determines the reaction time in which a case of intra-operative awareness would be detected with the given sensitivity and specificity.

Fig. 5.12: ROC curve for single electrode pairs (gray, average AUC 0.92), the whole data set (red, AUC 0.99), and combinations of the frontal electrodes FP1, FP2, F3 and F4 (green, AUC 0.98). The reference regimes are baseline (personalized template) and unconsciousness.



It should be noted that the global AUC values are larger than the average of the AUC topogram in fig. 5.11. To understand this, note that when averaging over a spatially resolved classifier m , the electrode pairs with $|m| \ll 1$ have a small weight. For instance, the average of a perfect classifier (AUC= 1, with $|m| \approx 1$) and one that fluctuates around zero (AUC= 0.5) is still perfect for sufficiently small fluctuations.

Table 5.1 gives a summary of the global AUC for the proposed measures, evaluated on pairs from the baseline, unconsciousness and awake regimes. A personalized template for the awake states (which is not possible in practice) increased the AUC considerably. Note that some of the combinations are not reasonable, like distinguishing between bl/aw using a measure with reference regimes bl/un.

In conclusion, the transfer symbols of neighboring channels, which have proven themselves as a powerful description in the application to the coupled map lattice of chapter 4, are a promising description for the EEG of different states of consciousness and the transitions between them. There are practical calibration difficulties and individual exceptions, but the results support the general conclusion that the symbolic description depends on the state of consciousness in a systematic and consistent way.

5.4 Auditory Evoked Potentials

The processing of an auditory stimulus in the midbrain (in the center of the brain, below the neocortex) causes electrical potential activity measurable on the scalp (see Nunez [68]). As mentioned, the magnitude of these potentials on the scalp is about 5% of the background activity. In order to increase the *signal to noise ratio* (SNR), it is common practice to consider an average over multiple *epochs* of the EEG taken after similar stimuli, so that any activity that is not related to the stimulus decays statistically.

In the first 1000 ms after a stimulus, there are about 15 reproducible features (maxima and minima, see fig. 5.13). Following Thornton and Sharpe [103], the first of those features – named *I-V* –, originate in the brain stem. The EEG data used in the present work comes from a study of *middle latency waves* (MLAEP) [41]. MLAEP include the features N_0, P_0, N_a, P_a, N_b and originate in the *medial geniculate* and the *primary auditory cortex*. Finally, there are responses with high latency (*late cortical waves*), including the features P_1, N_1, P_2, N_2, P_3 , which are related to higher cognitive functions and located in the frontal cortex and association areas. Similar features are observed for visual stimuli (see Allefeld [1]).

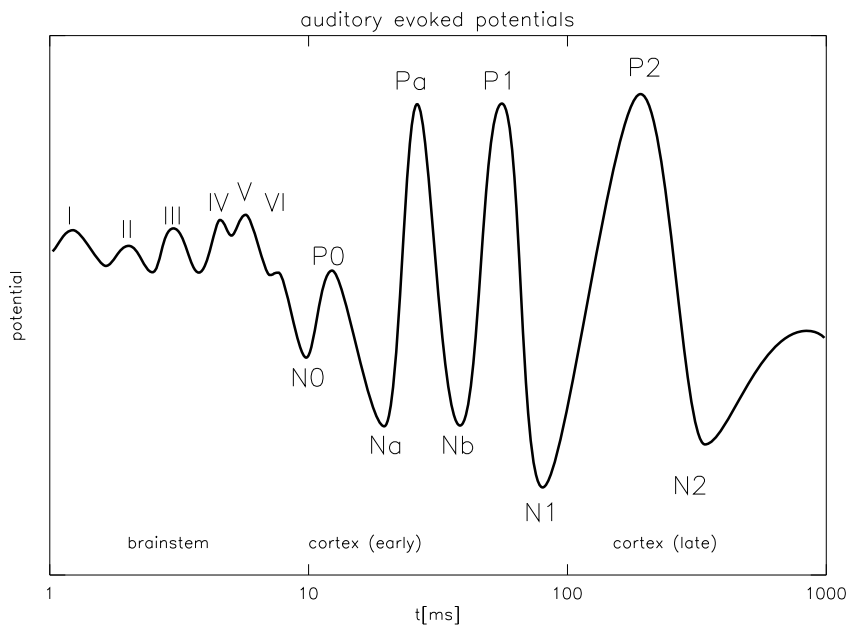


Fig. 5.13: The denotation of auditory evoked potentials according to Thornton and Sharpe [103].

The processing of a stimulus can vary considerably for different states of consciousness. Knowledge about this dependence can be used to determine the state of consciousness. For instance, the latency of P_a and N_b is highly related to the transition to unconsciousness [103]. For studying the effects of hypnotic anesthetics, latencies between 35 and 65 ms are considered as relevant [43]. EEG data from the electrode TP10 was used (which is common practice [41]).

The *postauricularis reflex* [43] is a muscle reflex, which for some individuals is triggered by auditory stimuli in the conscious state. Even though happening at fixed latencies after a stimulus, it is not considered as a part of the AEP, because it reflects activity from a muscle and not from the brain. The activity from the reflex is larger than the AEP activity, dominating the latencies about 10-30 ms for the affected individuals.

As mentioned previously, the stimuli were given every 120 ms, which resulted in a total of about 2625 epochs from the baseline and unconscious regime of each proband, respectively. I

considered epochs containing the first 100 ms after a stimulus. A digital filter from 26 – 400 Hz was used. The inclusion of high frequencies is justified by the fact that muscular activity is supposed not to be related to the trigger times (except for the mentioned postauricularis reflex). Since one is only interested in features related to a stimulus, *surrogate data* can be generated by collecting samples of 100 ms at random times. This data can serve as a reference population that includes all properties of the original data (e. g. the power spectrum) except the features which are related to the stimuli.

5.4.1 Modelling of the Average Profile

This section compares different models for the formation of the averaged signals commonly used in the study of evoked potentials. The measured triggered EEG activity is a superposition of a *response* caused by the processing of the stimulus and the *background* consisting of all stimulus-independent brain activity. Current evaluation methods define the amplitude or latency of pre-defined features [103] using an average over multiple epochs. There is not yet a commonly accepted model for the exact form of single AEP responses [43]. The common assumption is that variations in the response can be neglected, in other words that the average potential is a reasonable representative for the response to a single stimulus, and that the latency variations are low. The aim of this section is to test if a symbol-based approach can distinguish different models leading to the same average potential.

Let us first consider a model for the formation of the average signal. A simple average signal can be modeled as a single peak in the form of a Gaussian bell curve. Suppose that this curve is generated by multiple similar events. Then, the width of the average curve can reflect the width of the single events (fig. 5.14a) or it can be caused by sharp responses occurring with different latencies (fig. 5.14b). If the width (in terms of the standard deviation) of a single event is σ_s and the standard deviation of the latency t is σ_t , then the width of the average curve is given by

$$\sigma_a^2 = \sigma_s^2 + \sigma_t^2. \quad (5.5)$$

Since the integral is preserved in the average process, the corresponding amplitudes (maxima) a_a and a_s are related by

$$a_a * \sigma_a = a_s * \sigma_s. \quad (5.6)$$

Instead of using averages to increase the *signal to noise ratio* (SNR), I considered a symbolic description of single epochs and studied the symbol distribution over a sequence of stimuli. The aim here was to use an abstract description, which avoids premises like tailoring measures to certain details or latencies. This section compares different models for the formation of features that lead to the same average curve and tries to differentiate them using a symbolic description.

As an application to measured AEP data, a single feature in the average potential was modeled as described above, with fit parameter σ_s . For the model data, I took EEG background signals (epochs from the original data taken at random times, so that the original AEP-signal, as well as the background activity, cancels out statistically), and added the model signal.

Fig. 5.15 shows the data and its symbolic description ($n = 5$, $\tau = 1.8$ ms), for the original triggered data (part a) and for models of different peak width σ_s (parts b and c), based on one feature of one proband in the unconscious regime. The second row of graphs shows the responses (only applicable to the models) and the *grand average* (the average potential over all 2625 epochs). Even though the sharp peaks in fig. 5.15c are high enough to occasionally correspond

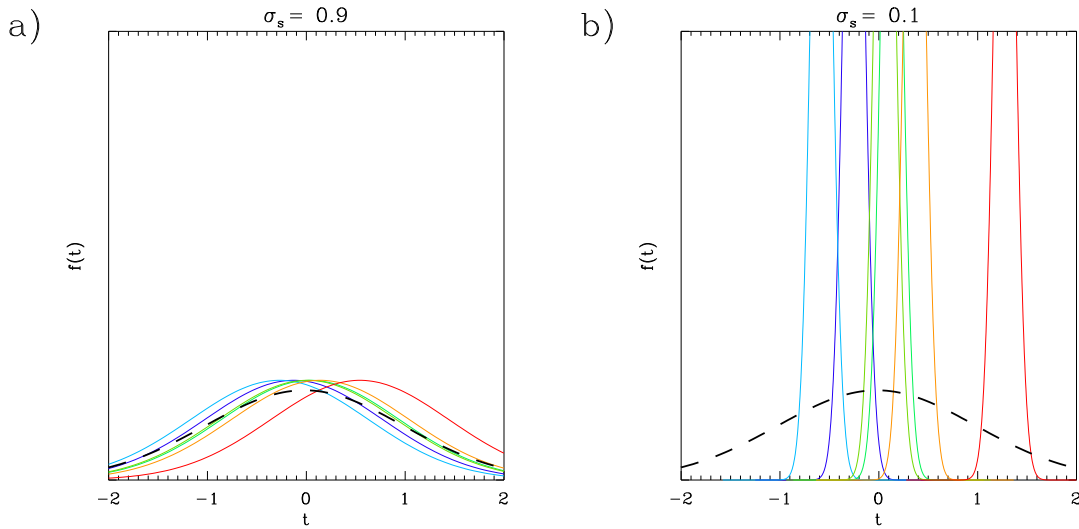


Fig. 5.14: Model responses made of Gaussian peaks with different widths, both leading to the same average signal (dashed line) with $\sigma_a = 1$: a) $\sigma_s = 0.9$ b) $\sigma_s = 0.1$.

to local maxima in the time series (first row), averaging over multiple curves is necessary to unambiguously identify the AEP response. Regarding the state symbol distribution (lowermost row), the average signal is clearly reflected, but there is no obvious preference for one of the models. Note that the symbol at latency t is based on data from the interval $[t, t + 7.2 \text{ ms}]$. Due to this, for instance the change from red to green at latency $t \approx 19 \text{ ms}$ for symbol #0 (monotonic incline) and #119 (monotonic decline) corresponds to symbols centered at the maximum of the average potential.

As a quantitative examination, I considered the Kullback-Leibler distance between the model and the measured data. Fig. 5.16a shows the distance as a function of the peak width σ_s and the latency t , fig. 5.16b shows the average over all latencies. Apparent deviations are observed for small values (roughly $\sigma_s \leq 1$). Larger values are not distinguished.

In conclusion, the AEP-features in single epochs of EEG data are reflected in the proposed symbolic description. The quantitative examination suggests that the extreme case of sharp spikes can be ruled out, supporting the common assumption that the average potential is a suitable approximation for the response to an auditory stimulus.

5.4.2 Distinguishing Different States of Consciousness

Since the preceding section showed that the AEP is visible to the symbols of single EEG epochs, this section uses the symbolic description of AEP to distinguish states of consciousness. I quantified the discrimination power in terms of the ROC, in the same manner as in section 5.3.5 for the background activity. For a monitor of anesthetic depth, the AEP is a promising candidate because it is directly related to the reaction of the brain to external stimuli, which is what the hypnotic component of general anesthesia aims to influence. I compared the baseline and the unconsciousness regime of all 15 probands.

Each epoch covers an interval of 100 ms of EEG data subsequent to an auditory stimulus. It is described by a sequence s_t of state symbols, where t is the latency. Like in section 5.3.4, I defined templates for the conscious and the unconscious regime, containing the latency-resolved

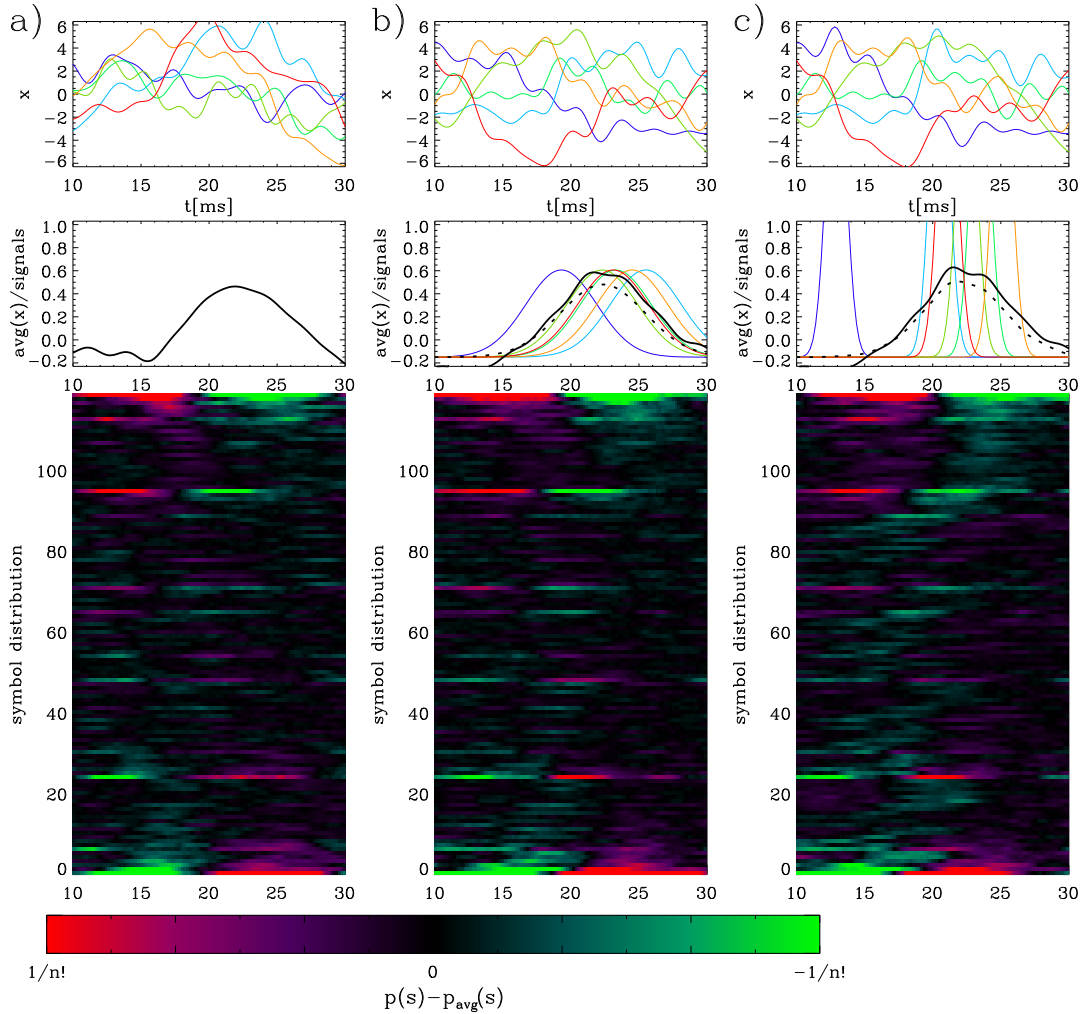


Fig. 5.15: AEP feature modeled by different types of responses. a) Triggered EEG data. b) Broad feature with $\sigma_a = 3$ ms, $\sigma_s = 2.6$ ms over EEG background. c) Sharp feature with varied latency ($\sigma_a = 3$ ms, $\sigma_s = 0.7$ ms) over EEG background. First row: Single epochs of the potential. Second row: Grand average over all epochs (black), single model signals (colored) and average model signal (dashed). Third row: State symbol distribution ($n = 5$, $\tau = 1.8$ ms). The color codes the deviation from the average distribution, in order to emphasize latency-dependent effects.

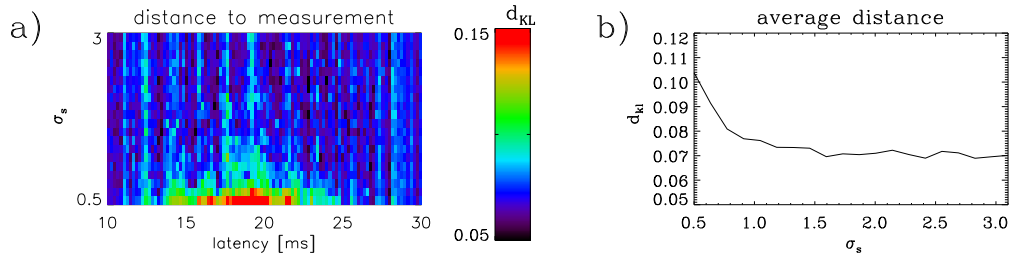


Fig. 5.16: Kullback-Leibler distance between the state symbol distribution of the model data and the measured data. a) For each latency b) Average over the latency.

symbol distribution p_t^{bl} and p_t^{pr} , respectively. For robustness against latency variations between individuals, the distributions for latency t were based on a sliding window of size 4 ms, centered at t .

In order to assign each epoch either to the conscious or the unconscious population, a *maximum likelihood* estimation was carried out. The maximum likelihood principle is a commonly used statistical estimation principle. Let $\{p_i\}_{i \in I}$ be a set of possible probability distributions modeling some phenomenon. The aim is to estimate the most plausible parameter i . Given a measured event a , a maximum likelihood estimator chooses the i that maximizes $p_i(a)$. The term likelihood refers to $p_i(a)$ as a function of i . In this case, one avoids to speak of probability, because this function can not be interpreted as a probability distribution.

This was done on the basis of single latencies, i. e. a symbol $s(t)$ was judged by its likelihood values $p_t^{bl}(s_t)$ and $p_t^{pr}(s_t)$. Since the symbols s_t for different latencies are not independent, there is no direct way to assign a likelihood to a symbol sequence. Therefore, a latency-resolved classifier d_t was defined as a normalized difference

$$d_t = \frac{p_t^{pr} - p_t^{bl}}{p_t^{pr} + p_t^{bl}}. \quad (5.7)$$

This classifier can be averaged over multiple latencies to obtain a classifier for a symbol sequence.

Fig. 5.17 shows the discrimination power, in terms of the AUC as defined in section 5.3.5, of the maximum likelihood test based on the state symbol distribution ($n = 5$, $\tau = 2$ ms). The raw EEG potential (i. e. no symbolic description) and its time derivative acted as reference data. In order to ensure that the reference data reflects the same information, I (nonlinearly) binned both the potential and its derivative to 120 equiprobable bins. This was done separately for baseline and unconsciousness. Based on the latencies from 35-65 ms, the symbol-based measure gave a significant distinction. In contrast, the reference measures based on binned EEG data were mostly close to the random classifier (AUC= 0.5). Proband #4 had an exceptionally strong postauricularis reflex (see the start of section 5.4), which might influence the latencies after 35 ms, and probably was responsible for the good performance of the reference measures for this proband.

The observed discrimination power depends on the individual (fig. 5.17a and c), but not on the latency (fig. 5.17b and d). A comparison with randomized triggers showed no noteworthy differences. Fig. 5.18 shows the discrimination power as a function of the individual as well as of the latency. Most of the curves are flat, on a level that depends on the individual. Sporadic areas of raised discrimination relate to occurrences of the postauricularis reflex, which is considerably stronger than the AEP.

The results suggest that symbols or the maximum likelihood approach used here are not sensitive to auditory evoked potentials. The observed discrimination effect is independent of the latency and therefore must reflect properties of the EEG background activity that are not related to the stimuli.

This is still an interesting result because for most probands the method allowed a good distinction of the baseline and unconsciousness regimes, based on only 100 ms of data from a single EEG electrode. The drawback is that it used a high frequency range of the EEG background, which is prone to perturbations like myogenic activity and usually left out in EEG background analysis (see section 5.1.3).

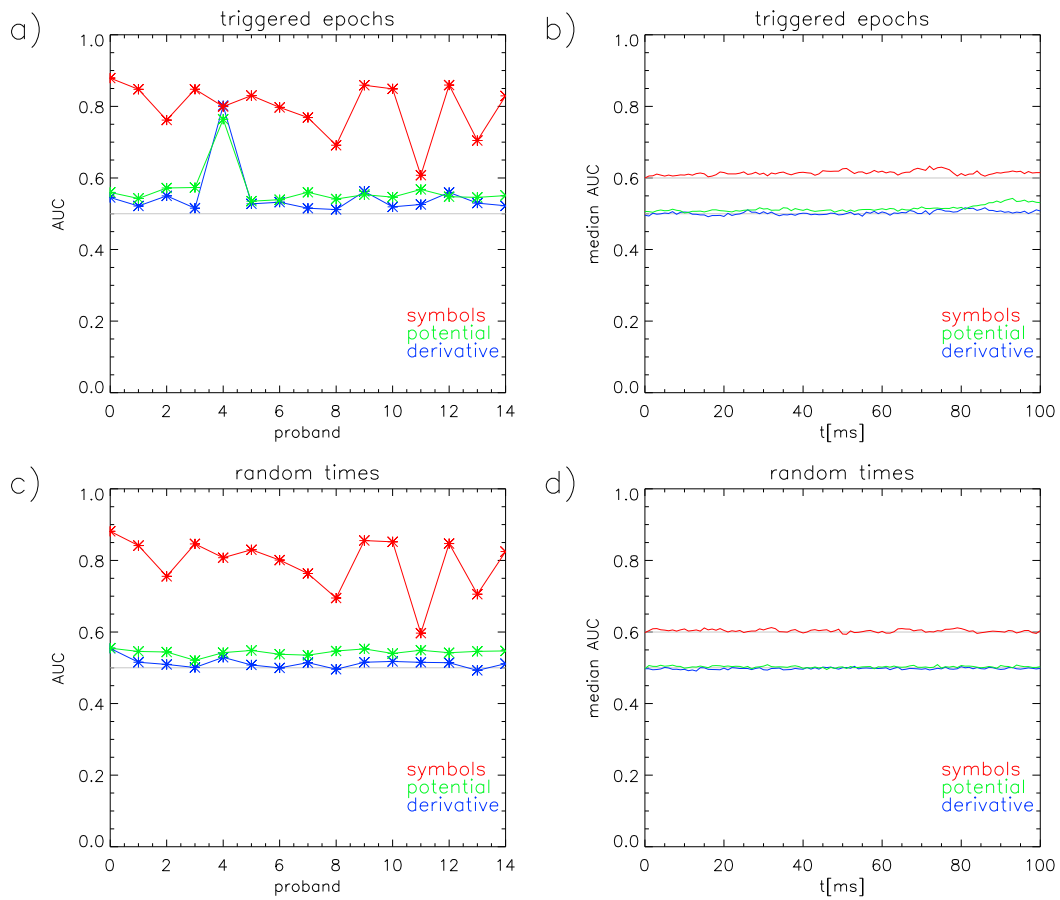


Fig. 5.17: Discrimination power of the maximum likelihood test. a) AUC of the measure (sum over the latencies from 35-65 ms) b) AUC for specific latencies (median over all probands). c) and d) Corresponding graphs for randomized triggers. The potential (green) and its derivative (blue) are binned to 120 equiprobable bins, in order to act as a reference for the symbolic description (red).

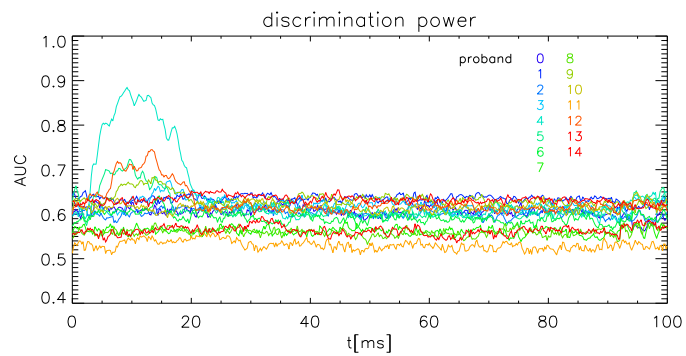


Fig. 5.18: Discrimination power (AUC) for each individual (colors) as a function of the latency.

Chapter 6

Discussion and Conclusions

The main objective of the present work is to study the theoretical background and properties of symbolic representations of time series, and their applications. There is a multitude of concepts, notations and viewpoints related to symbolic descriptions, which can roughly be separated into two domains, referred to as *rank orders* and *permutations*. The domain of rank orders is about a total order on a set of elements, leading to a set of static patterns, where one can study the symbol distributions, e. g. in terms of information entropy [11], or explain the occurrence of forbidden patterns. This domain is established in the literature and has been widely used. On the other side, permutations are bijective transformations that come along with a natural algebraic structure, leading to notions like transcriptions between rank orders or conjugacy classes and allowing the formulation of equations in terms of symbols.

Even though symbols have been named permutations, they have mostly been considered as the set of order patterns without further structure. In other words, in the consideration of symbolic representations, the algebraic structure of the symmetric group has hardly been exploited. Therefore, the focus of this work is to draw connections between the domains of rank orders and permutations, in order to understand in which aspects the corresponding concepts are similar or different, and to use algebraic considerations in the study of symbolic representations.

Section 3.1.3 discussed how the different notations and composition concepts fit into a common formalism. This included a canonical identification of order patterns with permutations. It became obvious that the two aforementioned domains correspond to viewpoints that appear to be surprisingly different. Hence, the properties or transformations that are natural in one domain may be highly complex in terms of the other.

I described the symbolic representation of a time series as a delay embedding into an n -dimensional space, followed by a certain form of discretization. Since the embedding step is well-known (see section 2.2 on Takens' theorem), section 3.1.4 studied the discretization process as a projection onto a partition of the delay embedding space. Compared to common binning methods using hyperplanes given by the coordinate system, the partition corresponding to the rank ordering process has quite a different geometry. Using translation and scaling invariance, the essence of the (n -dimensional) partition was described as a tessellation of an $n-2$ -dimensional sphere. The resulting polytope gives insights into the structure of the set of symbols from the 'rank order'-perspective, as well as into the different degrees of ambiguities that arise at the boundaries between different tiles. Along with this, I discussed how occurring ambiguities can be resolved in practice, proposing different methods that focus either on

information theoretic or on algebraic properties.

Section 3.1.6 discussed the parameters of a symbolic representation, namely the *sequence length* n and the *sampling pattern* τ . I argued that for high-dimensional systems it is generally not feasible to reconstruct the attractor. Instead, the choice of parameters for a symbolic description should be guided by the research question under consideration. State symbols have a hierarchical structure with respect to the sequence length, in the sense that a short symbol of sequence length $n - 1$ can be reconstructed from a longer symbol of sequence length n . Later in section 3.3, it was shown that transfer symbols do not follow such a hierarchy. I examined the limit of infinite sequence length, where an infinite symbol corresponds to a time series that is transformed to a uniform value distribution.

From an information theoretic point of view, any sampling pattern can potentially lead to the same amount of information. For instance, any sampling pattern leads to a uniform symbol distribution for an iid random time series, and to the identity symbol for a strictly monotonic time series. Different sampling patterns correspond to descriptions with different foci. The most suitable choice of sampling pattern may depend on the question under consideration. For instance, one can consider characteristic time scales to generate a symbolic description sensitive to the associated frequencies. In this context, any distance $(\tau_j - \tau_i)_{i < j}$ of a pair of delays is called a *time scale* of the sampling pattern τ . In this sense, an equidistant sampling pattern has the narrowest possible focus because it has the smallest possible number of different time scales. As a complement, I proposed a family of sampling patterns that has a wide focus in the above sense.

An appropriate descriptor often reflects important symmetries of the considered system. Section 3.1.7 discussed the behavior of symbolic representations under the transformations that are natural to real-valued time series. It came out that transfer symbols have useful invariance properties. Even though state symbols are well-behaved from the viewpoint of order patterns, their algebraic properties change in a complex way under those transformations. Hence, if asking for algebraic properties, it is more natural to use transfer symbols.

Section 3.2 applied different order concepts to symbolic representations with the aim to provide a collection of measures suitable to answer different kinds of questions. To describe similarities without time delays, a one-to-one comparison of concurrent symbols can be useful. For this reason, commonly used distance measures on the symmetric group were studied. A concept of dual measures was discussed, where corresponding distances are related but surprisingly different in terms of mutual information, self-dual measures being highly symmetric. To be sensitive to similarities arising at different times, measures based on symbol distributions can be useful. I discussed an approach to turn the Kullback-Leibler distance into a metric, as well as a measure for the distance of a pair of time series from being independent. It is closely related to (and bounded from above by) the mutual information, and differs by an additional projection that allows a valid statistic with smaller sample sizes.

Section 3.3 discussed the relation between symbols of different sequence length, which is a natural concept for rank orders, however less straightforward from the perspective of permutations. The truncation and expansion process, as well as the passing from one symbol to the next in the sequence, was formalized in algebraic terms. When considering rank orders, these transformations are natural and straightforward. In contrast, an algebraic description of the process is much more difficult, and the algebraic structure of an initial symbol does not univocally determine the algebraic properties of the result. Hence, even though the conceptual differences of the two perspectives on symbols may seem subtle, the structures that are natural from these viewpoints can differ largely. I also presented information theoretic

considerations, discussing the entropy rate of state symbols with uniform and non-equidistant sampling patterns, and transfer symbols.

In chapter 4, I applied symbolic representations to coupled map lattices (CML), which are typical examples where the synchronization concept from section 2.3.1 is not enough to describe all occurring phenomena of emerging ordered structures. Section 4.1 started the chapter with an introduction to CML, the logistic map as the base component, and the coupling mechanism used in the considered model.

In order to have an independent reference description, I first described the system using a set of well-known established measures (section 4.2). The complete 2-dimensional parameter space was investigated, using several complementary quantities to classify the occurring dynamics into well-defined regimes under consideration of both spatial and temporal order criteria. The dynamical regimes were described in detail, noting structures in spatial and temporal behavior like chaoticity, periodicity, formation of temporary or permanent clusters or different degrees of synchronization between cells.

Section 4.3 introduced the algebraic order of the transfer symbols of neighbor cells, which is the main symbol-based measure used in this chapter. By combining (temporal) rank orders with the comparison of different time series, the construction of transfer symbols is destined to describe spatio-temporal behavior. Even for a short sequence length of $n = 4$, this generic description is powerful enough to discriminate a broad variety of dynamical regimes, associating them to specific symbolic fingerprints. Otherwise, one needs several specialized measures to do so.

The symbol-based measure is compact enough to allow for simple visualization: for $n = 4$, the order distribution can be injectively mapped to the 3-dimensional color space, allowing an overview over the whole two-dimensional parameter space. This is useful, for instance for locating interesting regions, like the splitting into subsystems at $\epsilon = 1$ considered in section 4.2.3. One can easily choose paths to study certain transitions, as is done in section 4.3.4, for instance from spatially ordered to unordered dynamics. Furthermore, the study of transitions showed that the symbolic description is mostly smooth as a function of the dynamics, making it well-behaved.

A possible pitfall are the discontinuities that occur when there are ambiguities in the form of equal values within the time series (see also section 3.1.5). These discontinuities are in accordance with the idea of symbolic descriptions to focus on fundamental dynamical properties, while neglecting subtle changes.

In section 4.2.5, I discussed an observation that the specific mechanism for the initialization of random initial conditions can considerably influence the tendency of the system to synchronize.

The application of complexity measures in section 4.3.5 demonstrated spatial and temporal properties that are not only visible in the description but can be extracted separately.

The symbolic description can lead to strategies for studying, perturbing or controlling systems using the information what kinds of dynamical behavior are close to each other in terms of either the control parameters or the symbolic description. For instance, one could utilize a memory-based reasoning approach using the parameter space representation, searching nearest points in the parameter space, in order to promote or prevent a certain kind of dynamics.

In section 4.4, the transients of the system were studied in terms of a symbolic description.

From a metric perspective, one would expect that a system finally converges exponentially to the attractor whose basin of attraction contains the initial condition. However, a symbolic description neglects this asymptotic convergence. Instead, it indicates if the system is close enough to share the main dynamical properties of the attractor, corresponding to a 'macroscopic' view on the convergence. For this kind of considerations, symbolic descriptions were shown to be useful.

While the subject of the transient analysis could be described as large perturbations, which are only considered until they become sufficiently small, the stability analysis of section 4.5 studies the effect of small perturbations. Since it is a central property of a symbolic description to ignore such subtle changes in the dynamics, it is preferable to use a metric distance for such an analysis. The stability with respect to generic perturbations proved to be a good complement to the symbolic description. From the idea that both transient times and stability are related with convergence to an attractor, one could expect a correlation between both. This is not the case because the mentioned methods as defined here describe fundamentally different concepts of convergence. For instance, a state of independent chaotic cells immediately reaches its stationary state, even though it is classified as maximally unstable by the stability measure.

Section 4.6 studied a prediction of the stationary state given an early transient state, using a method of nonlinear prediction [101]. It came out that the prediction in terms of a symbolic description is a useful complement to the transient analysis, in the sense that the regimes with the longest transient times have small nonlinear prediction errors. In other words, if a state has a long transient, a symbolic description of the early development can generally predict in a good approximation where it will finally end up. A prediction of the dynamical regime given only the first iterations of the system also performs well.

In chapter 5, the human brain was considered as a real-world example of a spatio-temporal coupled system. At first glance, the network of neurons resembles a CML, even though the connection geometry of the real structure is far from geometric regularity. As a macroscopic observable of this system, I studied electroencephalographic data for local synchronization effects, in order to gain insights in the physiological processes, and to distinguish different states of consciousness.

In section 5.3, a description that was proven to be useful for detecting spatio-temporal order was adapted to the EEG: drawing an analogy from the EEG electrode geometry to the coupled map lattice of chapter 4, dynamical properties of the EEG were described with transfer symbols between neighbor electrodes. As a preparatory step, the presence of spatial synchronization phenomena was demonstrated by studying interrelations between pairs of electrodes as a function of the electrode distance.

I described the EEG data of a measurement as a trajectory in a low-dimensional space, acting as a simplified state space for the 'ultrahigh-dimensional' system. Systematic relations were shown between the symbolic description and the observed state of consciousness of the probands, with varying degrees of individual differences. Especially the baseline regime, which was measured before the administration of anesthetic, is highly individual, which is plausible but unfavorable for use as a reference. I proposed a scalar measure of anesthetic depth, using two reference regimes for the conscious and unconscious state, respectively. I evaluated the performance of this measure in terms of the *receiver operating characteristic* (ROC), with promising results. Possible optimizations were discussed, for instance an *individual template* for the conscious reference state improves the result considerably. Furthermore, I observed that a reduction of the set of measuring electrodes to the frontal area preserves most of the

discrimination power.

In a further approach, auditory evoked potentials (AEP), caused by the processing of acoustic stimuli, were studied (section 5.4). A symbolic description of single epochs was considered, using symbol statistics over a set of stimuli instead of the commonly used averaging of the data. Since the focus was on features occurring at fixed latencies after a stimulus, only symbols corresponding to the same latency were compared.

The study included an examination of the distributions, evaluating their discriminatory power with respect to different states of consciousness as a function of the latency, in comparison with the commonly used averaging method. The main observation was that, in general, the discrimination power of the measure has no noteworthy latency dependence, even though there are exceptions related to extraordinary features that are not considered part of the AEP. I conclude that the symbolic description studied here is not able to distinguish the ordinary AEP features of the examined states of consciousness.

Even though this work has revealed useful algebraic aspects in the context of symbolic representations, many open questions remain. A further examination of the field that connects the two domains referred to as rank orders and permutations can lead to new methodology. The ideas given here should be applied to other problems from different fields, tailoring measures in order to answer specific questions.

A further example from the field of EEG analysis could be *graphoelements*, which are local patterns within the EEG activity used in the diagnosis of pathologies. The characterization of classes of graphoelements given by a collection of samples could be a promising field for the application of symbolic descriptions.

The convergence argument from section 3.1.6 in mind, one could study a reversal of the projection done by a symbolic description. In this way, a symbolic representation would generate an approximate time series.

As a matter of principle, longer symbols contain more information. However, the increasing number of different symbols usually does not allow to estimate the symbol distribution with a reasonable sample size. Since most methods are based on symbol distributions, longer symbols aren't currently in use. A deeper understanding of the algebraic structure of the set of symbols can lead to refined methods describing the properties of single symbols. This would make the use of larger sequence lengths more attractive.

Symbolic representations could be useful for many other real world systems, for instance in computer-assisted process and system control, namely in the monitoring of rotating machinery like engines, bearings or turbines. Nonlinear analysis of time series is already used in the monitoring of machine tools using vibration sensors (cf. Simon [93]). A mapping of the symbolic signature, like in sections 4.4.2 and 5.3.3, could measure the wearing of tools or detect malfunction before the occurrence of functional disorder by observing deviations of the symbolic signature from the regime of normal operation. Even if a machine works at variable rotation speed, the normal mode of operation supposably still corresponds to a more or less distinct path (or a more complicated structure) in the description space, still allowing the detection of deviations.

In cases like these, any measurement of the system corresponds to a projection to a highly reduced description space. Symbolic descriptions give a complementary projection to that of many commonly used measures. Therefore, they promise to extract supplementary information that other methods can not access.

Bibliography

- [1] C. Allefeld. *Phase synchronization analysis of event-related brain potentials in language processing*. PhD thesis, Universität Potsdam, 2004.
- [2] J. M. Amigó, L. Kocarev, and J. Szczepanski. Order patterns and chaos. *Phys. Lett. A*, 335:27–31, 2006.
- [3] J. M. Amigó, R. Monetti, T. Aschenbrenner, and W. Bunk. Transcripts: an algebraic approach to coupled time series. *Chaos*, 22:013105, 2012.
- [4] J. M. Amigó, S. Zambrano, and M. A. F. Sanjuán. True and false forbidden patterns in deterministic and random dynamics. *EPL*, 79:50001, 2007.
- [5] J. M. Amigó, S. Zambrano, and M. A. F. Sanjuán. Permutation complexity of spatiotemporal dynamics. *EPL*, 90:10007, 2010.
- [6] R. E. Amritkar and S. Jalan. Self-organized and driven phase synchronization in coupled map networks. *Physica A*, 321:220–225, 2003.
- [7] H. Atmanspacher, T. Filk, and H. Scheingraber. Stability analysis of coupled map lattices at locally unstable fixed points. *European Physical Journal B*, 44(2):229–239, 2005.
- [8] H. Atmanspacher and H. Scheingraber. Stabilization of causally and non-causally coupled map lattices. *Physica A*, 345:435–447, 2005.
- [9] A. Bahraminasab, F. Ghasemi, A. Stefanovska, P. V. E. McClintock, and H. Kantz. Direction of coupling from phases of interacting oscillators: a permutation information approach. *Phys. Rev. Lett.*, 100:084101, 2008.
- [10] J. Balatoni and A. Rényi. Selected papers of A. Rényi, vol.1. *Academiai Budapest*, 1976.
- [11] C. Bandt and B. Pompe. Permutation entropy: a natural complexity measure for time series. *Phys. Rev. Lett.*, 88(17):174102, 2002.
- [12] G. Benettin, L. Galgani, and J.-M. Strelcyn. Kolmogorov entropy and numerical experiments. *Phys. Rev. A*, 14(6):2338–2345, 1976.
- [13] C. H. Bennett. On the nature and origin of complexity in discrete, homogeneous, locally-interacting systems. *Foundations of Physics*, 16(6):585–592, 1986.
- [14] S. Boccaletti, J. Kurths, G. Osipov, D. L. Valladares, and C. S. Zhou. The synchronization of chaotic systems. *Physics Reports*, 366:1–101, 2002.

- [15] B. Bohn. *Einbettung von Zeitreihen nach Takens' Theorem*. Diplomarbeit, Rheinische Friedrich-Wilhelms-Universität Bonn, 2010.
- [16] V. Bonhomme and P. Hans. Muscle relaxation and depth of anesthesia: where is the missing link? *British Journal of Anaesthesia*, 99:456–460, 2007.
- [17] R. Brown and L. Kocarev. A unifying definition of synchronization for dynamical systems. *Chaos*, 10(2):344–349, 2000.
- [18] J. Bruhn, P. S. Myles, R. Sneyd, and M. M. R. F. Struys. Depth of anaesthesia monitoring: what's available, what's validated and what's next? *British Journal of Anaesthesia*, 97(1):85–94, 2006.
- [19] J. B. Buck. Synchronous rhythmic flashing of fireflies. *The Quarterly Review of Biology*, 13(3):301–314, 1938.
- [20] J. B. Buck. Synchronous rhythmic flashing of fireflies II. *The Quarterly Review of Biology*, 63(3):265–289, 1988.
- [21] T. Buzug and G. Pfister. Comparison of algorithms calculating optimal embedding parameters for delay time coordinates. *Physica D*, 58:127–137, 1992.
- [22] G. J. Chaitin. On the length of programs for computing finite binary sequences. *Journal of the ACM*, 13:547–569, 1966.
- [23] J.-R. Chazottes and B. Fernandez. *Dynamics of coupled map lattices and of related spatially extended systems*. Springer, 2005.
- [24] T. Cover and J. Thomas. *Elements of information theory*. Wiley, 1991.
- [25] J. P. Crutchfield. Space-time dynamics in video feedback. *Physica D*, 10:229–245, 1984.
- [26] M. P. do Carmo. *Riemannian geometry*. Birkhäuser, 1992.
- [27] Y. Dobyns and H. Atmanspacher. Characterizing spontaneous irregular behavior in coupled map lattices. *Chaos, Solitons and Fractals*, 24:313–327, 2005.
- [28] R. Durrett and S. Levin. Spatial aspects of interspecific competition. *Theoretical Population Biology*, 53:30–43, 1998.
- [29] J.-P. Eckmann, S. Oliffson Kamphorst, and D. Ruelle. Recurrence plots of dynamical systems. *Europhys. Lett.*, 4(9):973–977, 1987.
- [30] S. Elizalde. Asymptotic enumeration of permutations avoiding generalized patterns. *Adv. in Appl. Math.*, 36:138–155, 2006.
- [31] J. D. Farmer, E. Ott, and J. A. Yorke. The dimension of chaotic attractors. *Physica D*, 7:153–180, 1983.
- [32] M. J. Feigenbaum. The universal metric properties of nonlinear transformations. *Journal of Statistical Physics*, 21(6):669–706, 1979.
- [33] B. Fiedler. *Handbook of Dynamical Systems*, volume 2. North-Holland, 2002.

- [34] A. M. Fraser and H. L. Swinney. Independent coordinates for strange attractors from mutual information. *Phys. Rev. A*, 33(2):1134–1139, 1986.
- [35] F. Galton. Co-relations and their measurement, chiefly from anthropometric data. *Proc. Roy. Soc. London*, 45:135–145, 1888.
- [36] L. Glass. Synchronization and rhythmic processes in physiology. *Nature*, 410:277–284, 2001.
- [37] L. Glass and M. C. Mackey. *From clocks to chaos*. Princeton University Press, 1988.
- [38] P. Grassberger and I. Procaccia. Characterization of strange attractors. *Phys. Rev. Lett.*, 50(5):346–349, 1983.
- [39] A. Groth. Visualization of coupling in time series by order recurrence plots. *Phys. Rev. E*, 72:046220, 2005.
- [40] F. Hausdorff. Dimension und äußeres Maß. *Math. Annalen*, 79:157–179, 1918.
- [41] A. Hock and S. Paprotny. personal communication.
- [42] H. H. Jasper. Report of the committee on methods of clinical examination in electroencephalography: 1957. *Electroencephalography and Clinical Neurophysiology*, 10(2):370–375, 1958.
- [43] D. Jordan. personal communication.
- [44] D. Jordan, G. Stockmanns, E. F. Kochs, S. Pilge, and G. Schneider. Electroencephalographic order pattern analysis for the separation of consciousness and unconsciousness. *Anesthesiology*, 109:1014–1022, 2008.
- [45] K. Kaneko. Spatiotemporal chaos in one- and two-dimensional coupled map lattices. *Physica D*, 37:60–82, 1989.
- [46] A. Katok and B. Hasselblatt. *Introduction to the modern theory of dynamical systems*. Cambridge University Press, 1996.
- [47] M. G. Kendall. A new measure of rank correlation. *Biometrika*, 30:81–89, 1938.
- [48] M. B. Kennel, R. Brown, and H. D. Abarbanel. Determining embedding dimension for phase-space reconstruction using a geometrical construction. *Phys. Rev. A*, 45(6):3403–3411, 1992.
- [49] E. Kochs. personal communication.
- [50] A. N. Kolmogorov. Three approaches to the definition of the concept of 'amount of information'. *Problemy Predachi Informatsii (Problems of Information Transmission)*, 1:3–11, 1965.
- [51] S. Kullback and R. A. Leibler. On information and sufficiency. *Ann. Math. Stat.*, 22(1).
- [52] P. Laurent. The supposed synchronal flashing of fireflies. *Science, New Series*, 45(1150):44, 1917.

- [53] P. Lavie. Ultrashort sleep-waking schedule. III. ‘gates’ and ‘forbidden zones’ for sleep. *Electroencephalography and Clinical Neurophysiology*, 63:414–425, 1986.
- [54] T.-Y. Li and J. A. Yorke. Period three implies chaos. *Amer. Math. Monthly*, 82(10):985–992, 1975.
- [55] W. Liebert, K. Pawelzik, and H. G. Schuster. Optimal embeddings of chaotic attractors from topological considerations. *Europhys. Lett.*, 14(6):521–526, 1991.
- [56] Z. Liu. Measuring the degree of synchronization from time series data. *Europhys. Lett.*, 68(1):19–25, 2004.
- [57] R. López-Ruiz, H. L. Mancini, and X. Calbet. A statistical measure of complexity. *Phys. Lett. A*, 209:321–326, 1995.
- [58] E. N. Lorenz. Deterministic nonperiodic flow. *Journal of the Atmospheric Sciences*, 20:130–141, 1963.
- [59] A. M. Lyapunov. Problème général de la stabilité du mouvement (transl. from russian). *Ann. fac. Sci. Univ. Toulouse*, 9:203–475, 1907. reproduced in *Ann. Math. Study* vol. 17, Princeton 1947.
- [60] B. Mandelbrot. *Die fraktale Geometrie der Natur*. Birkhäuser, 1987.
- [61] N. Marwan, M. C. Romano, M. Thiel, and J. Kurths. Recurrence plots for the analysis of complex systems. *Physics Reports*, 438:237–329, 2007.
- [62] C. Masoller and A. C. Marti. Random delays and the synchronization of chaotic maps. *Phys. Rev. Lett.*, 94:134102, 2005.
- [63] R. M. May. Simple mathematical models with very complicated dynamics. *Nature*, 261:459–467, 1976.
- [64] J. Milnor. On the concept of attractor. *Commun. Math. Phys.*, 99:177–195, 1985.
- [65] R. Monetti, W. Bunk, T. Aschenbrenner, and F. Jamitzky. Characterizing synchronization in time series using information measures extracted from symbolic representations. *Phys. Rev. E*, 79:046207, 2009.
- [66] M. Murphy et al. Propofol anesthesia and sleep: a high-density EEG study. *Sleep*, 34(3):283–291, 2011.
- [67] P. Nunez, R. B. Silberstein, Z. Shi, M. R. Carpenter, R. Srinivasan, D. M. Tucker, S. M. Doran, P. J. Cadusch, and R. S. Wijesinghe. EEG coherency II: experimental comparisons of multiple measures. *Clinical Neurophysiology*, 110:469–486, 1999.
- [68] P. Nunez and R. Srinivasan. *Electric fields of the brain*. Oxford University Press, 2006.
- [69] P. Nunez, R. Srinivasan, A. F. Westdorp, R. S. Wijesinghe, D. M. Tucker, R. B. Silberstein, and P. J. Cadusch. EEG coherency I: statistics, reference electrode, volume conduction, Laplacians, cortical imaging, and interpretation at multiple scales. *Electroencephalography and clinical Neurophysiology*, 103:499–515, 1997.

- [70] G.-L. Oppo and R. Kapral. Discrete models for the formation and evolution of spatial structure in dissipative systems. *Phys. Rev. A*, 33(6):4219–4231, 1986.
- [71] E. Ott. *Chaos in dynamical systems*. Cambridge Univ. Press, 2002.
- [72] N. H. Packard, J. P. Crutchfield, J. D. Farmer, and R. S. Shaw. Geometry from a time series. *Phys. Rev. Lett.*, 45(9):712–716, 1980.
- [73] K. Pearson. Mathematical contributions to the theory of evolution. III. regression, heredity and panmixia. *Philosophical Transactions of the Royal Society of London*, 187:253–318, 1896.
- [74] L. M. Pecora, L. Moniz, J. Nichols, and T. L. Carroll. A unified approach to attractor reconstruction. *Chaos*, 17:013110, 2007.
- [75] W. W. Peterson, T. G. Birdsall, and W. C. Fox. The theory of signal detectability. *Transactions of the IRE Professional Group on Information Theory*, 4:171–212, 1954.
- [76] A. Pikovsky, M. Rosenblum, and J. Kurths. *Synchronization*. Cambridge University Press, 2001.
- [77] H. Poincaré. Sur le problème des trois corps et les équations de la dynamique. *Acta Mathematica*, 13:1–270, 1890.
- [78] W. H. Press, B. P. Flannery, S. A. Teukolsky, and W. T. Vetterling. *Numerical recipes in C: the art of scientific computing*. Cambridge University Press, 1986.
- [79] T. Reichenbach, M. Mobilia, and E. Frey. Mobility promotes and jeopardizes biodiversity in rockpaperscissors games. *Nature*, 448:1046–1049, 2007.
- [80] E. Rodriguez, N. George, J.-P. Lachaux, J. Martinerie, B. Renault, and F. J. Varela. Perception’s shadow: long-distance synchronization of human brain activity. *Nature*, 397:430–433, 1999.
- [81] M. G. Rosenblum and A. S. Pikovsky. Synchronization: from pendulum clocks to chaotic lasers and chemical oscillators. *Contemporary Physics*, 44(5):401–416, 2003.
- [82] M. G. Rosenblum, A. S. Pikovsky, and J. Kurths. From phase to lag synchronization in coupled chaotic oscillators. *Phys. Rev. Lett.*, 78(22):4193–4196, 1997.
- [83] O. E. Rössler. An equation for continuous chaos. *Phys. Lett.*, 57A(5):397–398, 1976.
- [84] D. Ruelle and F. Takens. On the nature of turbulence. *Commun. math. Phys.*, 20:167–192, 1971.
- [85] M. Sande Lemos and B. J. Fish. The weighted average reference montage. *Electroencephalography and clinical Neurophysiology*, 79:361–370, 1991.
- [86] T. Sauer, J. A. Yorke, and M. Casdagli. Embedology. *J. Stat. Phys.*, 65:579–616, 1991.
- [87] S. Schinkel, N. Marwan, and J. Kurths. Order patterns recurrence plots in the analysis of ERP data. *Cogn. Neurodyn.*, 1:317–325, 2007.

- [88] G. Schneider. Intraoperative Wachheit. *Anesthesiol. Intensivmed. Notfallmed. Schmerzther.*, 38:75–84, 2003.
- [89] G. Schneider, R. Hollweck, M. Ningler, G. Stockmanns, and E. F. Kochs. Detection of consciousness by electroencephalogram and auditory evoked potentials. *Anesthesiology*, 103:934–943, 2005.
- [90] C. E. Shannon. A mathematical theory of communication. *The Bell System Technical Journal*, 27:379–423, 623–656, 1948.
- [91] R. Shaw. *The dripping faucet as a model chaotic system*. Aerial Press, 1984.
- [92] J. S. Shiner and M. Davidson. Simple measure for complexity. *Phys. Rev. E*, 59(2):1459–1464, 1999.
- [93] T. Simon. *Beiträge zur Steuerung und Analyse von technischen Bearbeitungssystemen mit Methoden der Nichtlinearen Zeitreihenanalyse*. PhD thesis, Johannes Gutenberg-Universität Mainz, 1999.
- [94] S. Smale. Differentiable dynamical systems. *Bull. Amer. Math. Soc.*, 73:747–817, 1967.
- [95] R. Solomonoff. A formal theory of inductive inference, part 1 and part 2. *Information and control*, 7:1–22, 224–254, 1964.
- [96] C. Spearman. The proof and measurement of association between two things. *The American Journal of Psychology*, 15:72–101, 1904.
- [97] S. H. Strogatz. *Nonlinear dynamics and chaos: with applications in physics, biology, chemistry, and engineering*. Addison Wesley, 1994.
- [98] S. H. Strogatz. *Sync*. Hyperion, 2003.
- [99] S. H. Strogatz, D. M. Abrams, A. McRobie, B. Eckhardt, and E. Ott. Crowd synchrony on the Millennium Bridge. *Nature*, 438:43–44, 2005.
- [100] S. H. Strogatz, R. E. Kronauer, and C. A. Czeisler. Circadian pacemaker interferes with sleep onset at specific times each day: role in insomnia. *American Journal of Physiology*, 253:R172–R178, 1987.
- [101] G. Sugihara and R. May. Nonlinear forecasting as a way of distinguishing chaos from measurement error in time series. *Nature*, 344:734–741, 1990.
- [102] F. Takens. Detecting strange attractors in turbulence. *Springer Lecture Notes in Mathematics*, 898:366–381, 1981.
- [103] C. Thornton and R. M. Sharpe. Evoked responses in anesthesia. *British Journal of Anesthesia*, 81:771–781, 1998.
- [104] F. Topsøe. Some inequalities for information divergence and related measures of discrimination. *IEEE Trans. Info. Th.*, 46:1602–1609, 2000.
- [105] J. F. Traub, G. W. Wasilkowski, and H. Woyzniakowski. *Information, uncertainty, complexity*. Addison-Wesley, 1983.

-
- [106] W. Tucker. The Lorenz attractor exists. *C. R. Acad. Sci. Paris*, 328:1197–1202, 1999.
- [107] H.-M. Weinmann. *Ableitung und Beschreibung des kindlichen EEG*. Zuckschwerdt, 1986.
- [108] E. M. Whitham et al. Scalp electrical recording during paralysis: quantitative evidence that EEG frequencies above 20 Hz are contaminated by EMG. *Clinical Neurophysiology*, 118:1877–1888, 2007.
- [109] H. Whitney. Differentiable manifolds. *Ann. Math.*, 37(3):645–680, 1936.
- [110] A. T. Winfree. Spiral waves of chemical activity. *Science*, 175(4022):634–636, 1972.
- [111] A. T. Winfree. The prehistory of the Belousov-Zhabotinsky oscillator. *Journal of Chemical Education*, 61(8):661–663, 1984.
- [112] A. Wolf, J. B. Swift, H. L. Swinney, and J. A. Vastano. Determining Lyapunov exponents from a time series. *Physica D*, 16(3):285–317, 1985.
- [113] A. N. Zaikin and A. M. Zhabotinsky. Concentration wave propagation in two-dimensional liquid-phase self-oscillating systems. *Nature*, 225:535–537, 1970.

Acknowledgments

The work presented here would not have been possible without the help and guidance of many people. Firstly, I am very grateful to Prof. Dr. Gregor Morfill for the invitation into his outstanding research group, the supervision of this work, and much freedom to choose the direction of research. Thanks also to the Max-Planck-Society for financial support of this work, and for the possibilities to take part in workshops and to present this work at international conferences.

I am also much obliged to my supervisor Dr. Wolfram Bunk, who has taken considerable time for extensive discussions, which through many suggestions and konstruktive criticism brought this work to its current shape. At this point I would also like to mention Dr. Roberto Monetti und Dr. Thomas Aschenbrenner, many thanks to you for numerous helpful discussions and corrections.

In the context of the EEG analysis, I thank Prof. Dr. Eberhard Kochs and his research group from the Klinikum rechts der Isar for the collaboration with MPE, which enabled me to apply my methods to real-world data. A special thanks also to Dr. Denis Jordan for corrections regarding practical aspects of elektroencephalography.

I would like to thank Dr. Peter Huber, Dr. Leila Taghizadeh und Antje Eckhoff for numerous corrections of formal and linguistic nature.

Last but not least, sincere thanks to the theory group as a whole for the cordial atmosphere that makes this department a great place to work.